Mondragon Unibertsitatea

DOCTORAL THESIS

RELIABLE INDUSTRIAL COMMUNICATIONS OVER MMWAVE BANDS

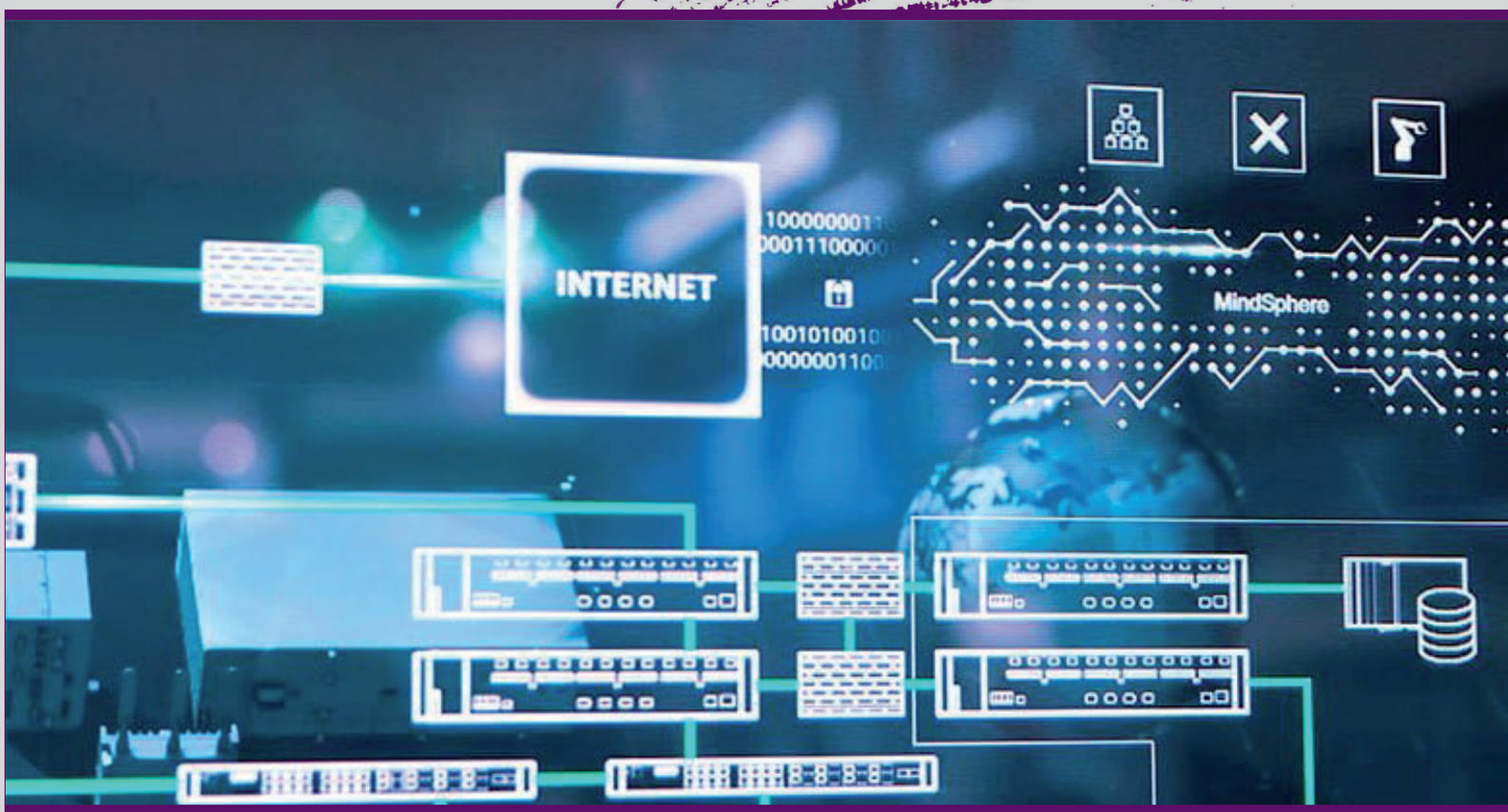

JOSEBA OSA AROZENA | Arrasate-Mondragón, 2023

JOSEBA OSA AROZENA | Reliable Industrial Communications over mmWave Bands

MONDRAGON UNIBERTSITATEA

GOI ESKOLA POLITEKNIKOA

FACULTY OF ENGINEERING

PHD THESIS

Reliable Industrial Communications over mmWave Bands

Author:

JOSEBA OSA AROZENA

Supervisors:

Dr. MIKEL MENDICUTE ERRASTI

Dr. IÑAKI VAL BEITIA

Computer and Electronics Department

Faculty of Engineering

Mondragon Unibertsitatea

Arrasate

October 2023

"You never fail until you stop trying"
Albert Einstein

Dedicada a todas las personas que han confiado en mi,
Joseba

Acknowledgments

I would like to begin by thanking my supervisors Mikel Mendicute and Iñaki Val for their guidance during this journey. Thank you for letting me research the topics that I found most interesting while assisting me with all your knowledge and experience in the field. Special thanks to Mikel for proposing me to participate in the PhD program of the university of Mondragon and helping me out in all the process.

I would like to thank professor Iban Barrutia in particular for helping me with all the RF related doubts that came to my mind. Thank you for sharing your useful advice and guiding me when the next step was unclear.

I am thankful to the signal theory and communications group as well, specially to all the PhD students that have pursued their goals along me. Many thanks to Joseba Gorospe, Jokin Cifuentes, Jon Ayerdi, Jenifer Brenes and the rest of the laboratory members who were beside me during this journey, and good luck with the path that you have ahead. I am sure that you will get there.

Many thanks to the electrical engineering group from the Högskolan i Gävle for welcoming me to research with them in Sweden. Special thanks to professors Niclas Björsell, Per Ängskog, Daniel Rönnow and Håkan Hugosson, as well as the PhD students Oscar Bautista, Ali Bemani, Amir Hosseinzadeh and Muhammad Hassan for making my stay an unforgettable experience.

At last, I would like to express my gratitude to my family and friends for their constant support in this adventure. Many thanks to my parents and sister for their unconditional support and helping me out in every possible way.

Declaration

I hereby declare that this work is my original authorial work, which I have worked out on my own. All sources, references, and literature used or excerpted during the elaboration of this work are cited and listed in complete reference to the due source.

Joseba Osa Arozena
Arrasate, October 2023

Abstract

Communication systems are a key enabling technology for the industry 4.0 revolution, since they provide the ability to exchange information between different devices. This makes tasks as remote monitoring and control of processes possible, adding a new degree of flexibility to the existing industrial facilities. The communications of this kind of use cases differ significantly with the ones that belong to more generic scenarios as home or office, since aspects as reliability and latency are critical to ensure the proper operation of industrial processes. In order to comply with the requirements, wired solutions were introduced first because they can meet the demands using relatively simple implementations thanks to the use of a dedicated medium. However, wireless solutions offer several advantages compared to the wired counterpart such as a lower cost in deployment and maintenance, flexibility to re-organize factory plants or the ability to operate in moving or rotating elements. This is why the implementation of wireless industrial communications is an actively discussed topic in both academic and industrial fields. However, as wireless communications use a shared medium that is prone to interference and noise, none of the existing proposals meet the most stringent requirements defined in industrial use cases.

In this thesis, the use of the 2.4 GHz ISM frequency band was identified as a possible cause of this lack of reliability, since most of nowadays solutions operate over this license-free frequency band that is already saturated with other applications and interference is unavoidable. In order to overcome this issue, the use of the 60 GHz mmWave spectrum is proposed as a possible alternative for the radio access, as it offers several advantages as a higher bandwidth or a far less saturated medium. Since the propagation of electromagnetic signals in the mmWave spectrum has not been widely characterized in industrial settings, this thesis is focused on expanding the existing knowledge in this particular field. The objective is to provide the required evidence to determine if the proposed solution is a valid candidate to achieve reliable industrial communications over a wireless medium.

As for the contributions, a cost-effective double directional channel sounder that measures propagation in the mmWave spectrum was created first with the aim of

characterizing industrial facilities. Two different measurement campaigns were carried out after with this equipment, where the key propagation metrics were obtained within two workshops and a pit oven from a steel company. A stochastic channel model that represents the observed propagation was developed then to be able to represent it in network simulation tools. At last, the performance that a commercial mmWave standard can offer in a typical industrial network was analysed to assess the viability of the technology and identify possible improvements that can be done to the standard. Regarding the results, the analysed standard showed potential to cope with the most demanding industrial use cases, even if modifications are required to reach the desired performance.

Laburpena

Komunikazio sistemak industria 4.0 eraldaketa lortzeko gakoa den teknologia dira, gailu desberdinen artean informazioa parekatzea ahalbidetzen dutelako. Honen bitartez, makina desberdinen monitorizazioa eta kontrola lekuan bertan egon gabe burutu ahal da, fabrikazio prozesuen kontrol eta jarraipen eraginkorragoa lortuz. Kasu hauetan erabiltzen diren komunikazioak ez dute inongo zerikusirik beste kontestu batzuetan aurki daitezkeen sareekin, esaterako etxe edo bulego batean. Arrazoi nagusia industriako aplikazioetan dago, hauek determinismo eta latentziarekiko kritikoak diren baldintza batzuk bete behar dituztelako. Hau dela eta, sortu ziren lehenengo protokoloak kable bidez komunikatzen ziren, teknologia honek komunikatzeko kanal esklusibo bat eskaintzen duelako eta inplementazio sinpleek eskatzen diren baldintza guztiak betetzen dituztelako. Dena den, haririk gabeko protokoloek hainbat abantaila eskaintzen dituzten, haien artean instalazio eta mantentze-lanetarako kostu baxuago bat, makinak lekuz aldatzeko ahalmena edo mugimenduren bat duten piezetan instalatzeko gaitasuna egonik. Honegatik, haririk gabeko protokolo industrialen garapena asko eztabaidatzen den gai bat da, bai industria sailean eta baita mundu akademikoan ere. Teknologia honek duen arazorik handiena mezuak aire bidez transmititzen direla da, hau parekatzen den baliabide bat delako eta ondorioz interferentziekin erlazionatutako arazoak agertzen direlako. Honen ondorioz, garatu diren protokoloak ez dira gai aplikazio industrial kritikoenei dagokien baldintzak asebetetzeko.

Tesi honen hasieran, arazo honen arrazoietako bat 2.4 GHz ko ISM frekuentzien erabilera dela identifikatu zen, izan ere frekuentzia hauetan lizentziarik gabe transmititu ahal da eta dagoeneko aplikazio askok erabiltzen dute, interferentzia maila areagotuz. Arazo hau ekiditeko, tesi honetan 60 GHz inguruko frekuentziak erabiltzea proposatzen da konponbide bezala. Proposamen honek abantaila ugari ditu, hauen artean banda zabalera handiago bat edo interferentzia gutxiago duen komunikazio kanal bat egonik. Mota honetako seinaleen propagazioa ez dago guztiz aztertuta eremu industrialetan, eta tesi honen helburua gai honetan sakontzea da. Helburu hau propagazioari buruzko informazioa beharrezkoa delako jarri da, honek zehaz-

tuko duelako ea benetan frekuentzia banda berri hau erabili ahalko den aplikazio industrialetan.

Lortu diren ekarpenei dagokienez, lehenengo eta behin 60 GHz inguruko seinale elektromagnetikoen propagazioa neurtzeko gailu bat garatu zen. Honen ondoren, bi neurketa-kanpaina burutu ziren, non seinaleen propagazioa bi tailer desberdinetan eta altzairugintzarako labe batean aztertu zen eta honekin erlazionatutako metrikak eskuratu ziren. Hurrengo urratsa aztertu zen propagazioa errepresentatzeko modelo estokastiko bat sortzea izan zen, honen bitartez jasotako informazioa simulazio tresnetan erabili ahal delako. Bukatzeko, 60 GHz tan dabilen protokolo komertzial batek sare industrial bat kudeatzeko duen ahalmena aztertu zen, non teknologia honen bideragarritasuna eta protokoloari egin litzaizkiokeen hobekuntzak aztertu ziren. Ikerketa honen emaitzei dagokionez, testeatu den estandarrak eskakizun zorrotzak dituzten aplikazio industrialekin lan egiteko potentziala azaldu du, nahiz eta honi aldaketa batzuk egitea ezinbestekoa den erabilera kasu zorrotzenekin ibili ahal izateko.

Resumen

Los sistemas de comunicación son una tecnología clave para la revolución industria 4.0, ya que dotan a los dispositivos de la capacidad de intercambiar información. Esto permite realizar tareas como la monitorización y control de procesos industriales de forma remota, aumentando así la flexibilidad que estos puedan tener. Este tipo de comunicación difiere significativamente del que se puede esperar en otros entornos como el hogar y oficina, dado que aspectos como la fiabilidad y latencia son críticos para asegurar un correcto funcionamiento de los procesos. Considerando esto, las primeras propuestas de redes industriales fueron sobre cable, ya que el uso de un medio dedicado permite que implementaciones simples puedan proveer todas las garantías necesarias. No obstante, siempre ha habido interés en soluciones inalámbricas, ya que éstas proporcionan una serie de ventajas como un costo reducido de instalación y mantenimiento, mayor flexibilidad a la hora de reorganizar plantas o la habilidad de operar en elementos con movilidad. Es por esto por lo que la adopción de soluciones inalámbricas para redes industriales es un tema ampliamente discutido en los ámbitos industriales y académicos. El mayor reto que presenta esta tecnología está relacionado con el uso de un medio compartido, ya que esto dificulta garantizar la fiabilidad y, consecuentemente, ninguno de los estándares existentes cumple con las demandas de las aplicaciones más exigentes.

Esta tesis identificó el uso de la banda de frecuencia ISM de 2.4 GHz como una posible causa de la falta de fiabilidad, dado que muchas aplicaciones hacen uso de estas frecuencias que no requieren licencia y las interferencias entre ellas son inevitables. Se planteó utilizar la banda de 60 GHz como posible alternativa, ya que esta ofrece numerosas ventajas como un ancho de banda superior o un medio que cuenta con significativamente menos interferencia. No obstante, la propagación de este tipo de señal no está extensamente caracterizada en entornos industriales, y esta tesis se ha focalizado en expandir el conocimiento existente en este ámbito. Todo esto se ha llevado a cabo con la finalidad de determinar si la solución propuesta podría ser un candidato válido para obtener comunicaciones industriales fiables sobre un medio inalámbrico.

En cuanto a las contribuciones, se comenzó por elaborar un dispositivo capaz de medir la propagación de señales electromagnéticas en la banda de 60 GHz con la finalidad de caracterizar entornos industriales. Después, se llevaron a cabo dos campañas de mediciones en total, en las que se pudo medir la propagación en dos talleres y un horno de pozo de una acería. Dichas mediciones sirvieron para extraer las métricas clave de la propagación observada, las cuales se utilizaron posteriormente para elaborar un modelo estocástico. Finalmente, se utilizó el modelo para evaluar la capacidad de un estándar comercial que opera sobre 60 GHz en una casuística industrial. Este estudio sirvió para determinar la viabilidad que tendrían las redes de frecuencias milimétricas en la industria, así como identificar las posibles mejoras que podrían realizarse para incrementar la fiabilidad del estándar. En cuanto a los resultados obtenidos, se pudo comprobar que el estándar analizado posee potencial para las aplicaciones industriales de alta demanda, aunque realizar una serie de modificaciones sería necesario para poder cumplimentar con las demandas más exigentes.

Contents

List of Figures

List of Tables

Acronyms

3GPP Third Generation Partnership Project.

A-BFT Association Beamforming Training.

ABG Alpha-Beta-Gamma.

ACK Acknowledge.

ADC Analog to Digital Converter.

AGC Automatic Gain Control.

AID Association ID.

AoA Angle of Arrival.

AoD Angle of Departure.

AP Access Point.

AS Azimuth Spread.

ASA Azimuth Spread of Arrival.

ASD Azimuth Spread of Departure.

ATI Announcement Transmission Interval.

AWGN Additive White Gaussian Noise.

AWV Antenna Weight Vector.

BA Building Automation.

BER Bit Error Rate.

BHI Beacon Header Interval.

BI Beacon Interval.

BRP Beam Refinement Protocol.

BTI Beacon Transfer Interval.

CBAP Contention Based Access Period.

CDF Cumulative Distribution Function.

CE Channel Estimation.

CI Close-In.

CIR Channel Impulse Response.

COTS Commercial-Off-The-Shelf.

CPS Cyber-Physical Systems.

CSCN IEEE Conference on Standards for Communications and Networking.

CSMA/CA Carrier Sensing Multiple Access with Collision Avoidance.

CTS Clear To Send.

CW Continuous Wave.

DAC Digital to Analog Converter.

DCF Distributed Coordination Function.

DMG Directional multi-Gigabit.

DS Delay Spread.

DTI Data Transfer Interval.

ES Elevation Spread.

FA Factory Automation.

FCS Frame Check Sequence.

FI Floating Intercept.

FPGA Field Programmable Gate Array.

FSPL Free Space Path Loss.

Gbps Gigabit Per Second.

GEV Generalized Extreme Value.

HiG Högskolan i Gävle.

HPBW Half Power Beam Width.

HPress Hydraulic Press Area.

HW Hardware.

I In-phase.

IDE Integrated Development Environment.

IDFT Inverse Discrete Fourier Transform.

IEEE Institute of Electrical and Electronics Engineers.

IF Intermediate Frequency.

IFFT Inverse Fast Fourier Transform.

IIoT Industrial Internet of Things.

IP Internet Protocol.

ISM Industrial, Scientific and Medical.

ITU International Telecommunication Union.

K-S Kolmogorov-Smirnov.

LDPC Low-Density Parity Check.

LFSR Linear Feedback Shift Register.

LHA Lens Horn Antenna.

LoS Line of Sight.

MAC Medium Access Control.

MC Monte Carlo.

MCS Modulation and Coding Scheme.

Mill Milling Station.

MIMO Multiple-Input Multiple-Output.

MLS Maximum Length Sequence.

mmICM millimeter Industrial Channel Model.

mmWave Millimeter Wave.

MPDU MAC Protocol Data Unit.

MSE Mean Squared Error.

MU Mondragon Unibertsitatea.

NED Network Description.

NIST National Institute of Standards and Technology.

NLoS Non Line of Sight.

NR New Radio.

NS Network Simulator.

OFDM Orthogonal Frequency-Division Multiplexing.

OMNeT++ Objective Modular Network Testbed for C++.

PA Process Automation.

PAPR Peak-to-Average Power Ratio.

PC Personal Computer.

PCAP Packet Capture.

PDF Probability Density Function.

PDP Power Delay Profile.

PER Packet Error Rate.

PHY Physical.

PL Path Loss.

PN Pseudo-random Noise.

PPDU Physical Protocol Data Unit.

PRBS Pseudo-Random Binary Sequence.

PSDU Physical Service Data Unit.

Q Quadrature.

Q-D Quasi-Deterministic.

RMS Root Mean Square.

RMSE Root Mean Square Error.

RS Reed-Solomon.

RSSI Received Signal Strength Indicator.

RTS Request To Send.

RTT Round-Trip Time.

Rx Receiver.

S-V Saleh-Valenzuela.

SAGE Space-Alternating Generalized Expectation-Maximization.

SBR Shooting and Bouncing Ray.

SC Single Carrier.

SHARP Synchronous and Hybrid Architecture for Real-time Performance.

SNR Signal-to-Noise Ratio.

SP Service Period.

STA Station.

STD Standard Deviation.

STF Short Training Field.

TCP Transmission Control Protocol.

TDL Tapped Delay Line.

TRN-R Receive Training.

TRN-T Transmit Training.

TSN Time-Sensitive Networking.

TU Time Unit.

Tx Transmitter.

UDP User Datagram Protocol.

USB Universal Serial Bus.

VMC Vertical Machining Center.

VNA Vector Network Analyser.

WFCS IEEE International Workshop on Factory Communication Systems.

WIA-FA Wireless Networks for Industrial Automation - Factory Automation.

WIA-PA Wireless Networks for Industrial Automation - Process Automation.

WISA Wireless Interface for Sensors and Actuators.

WSAN Wireless Sensors and Actuators Network.

ZC Zadoff-Chu.

Chapter 1

Introduction

A general introduction of this PhD thesis is provided in this chapter, where the main motivation behind this work, generated contributions, publications and related activities are described. The structure that the rest of the document follows is detailed in the end of the chapter as well.

1.1 Motivation

Four major industrial revolutions have occurred until now [1]. The first revolution, which began in 1800s, introduced the mechanization of processes. This was implemented mostly in steel and textile industries as well as railway transportation, where steam powered machinery was added to replace manual labour. The second revolution introduced electrification to the factories, which enabled the implementation of the concept of mass production. The production lines were fixed at the time, and it was not possible to modify or customize the end products. The third revolution arrived with the invention of microelectronics and the automation of processes, which brought programmable machines that added some degree of flexibility to the production lines. At last, the industry 4.0 revolution began approximately a decade ago as a result of the development of information and communication technologies [2, 3].

The term industry 4.0 appeared first at the 2011 Hannover fair in Germany as a strategic initiative for the industrial development, where the concept of smart factories was introduced [4]. A hierarchical representation proposed in [4] for a smart factory can be seen in Figure 1.1. Here, the different aspects of the industry 4.0 are divided in ranges of abstraction, beginning with the elements that interact with the production itself and moving towards a more digital environment. The lowest category, which is referred as *Physical Resource Layer*, represents the devices that are responsible of the production and their surroundings. The concept of Cyber-Physical Systems (CPS) is introduced in this category [5, 6], where machines have advanced control and sensing capabilities and are able to operate in an autonomous manner. Additionally, they are

also connected to a network, which is the next layer of the hierarchy. This concept is known as Industrial Internet of Things (IIoT) in the literature [7], where all the production elements are connected to add new capabilities to the factories as remote control (edge/cloud computing), predictive maintenance, virtualization of processes and more.

As it can be seen, communication systems are a fundamental part of the industry 4.0 revolution. The ability to exchange information between devices is essential to carry out all the smart functionalities described above, and for this reason it is an extensively discussed topic in both industrial and academic fields. In this regard, the National Institute of Standards and Technology (NIST) has recently carried out a meta-analysis that compiles the requirements that have been defined in several works for communications within factories [8]. All these works separate the different use cases given to communications within factories in several categories, depending on their demands in terms of latency, reliability, update rate, security, range and other performance indicators. The work presented in [8] has compiled all the requirements that have been defined in the other studies and elaborates a proposal that combines the main aspects of each, which can be seen in Table 1.1.

The mission-critical aspect of the communications is the baseline of the categorization, where the lowest communication classes equal to the most demanding use cases. There are six classes in total (0 to 5), but the fifth class is not included in

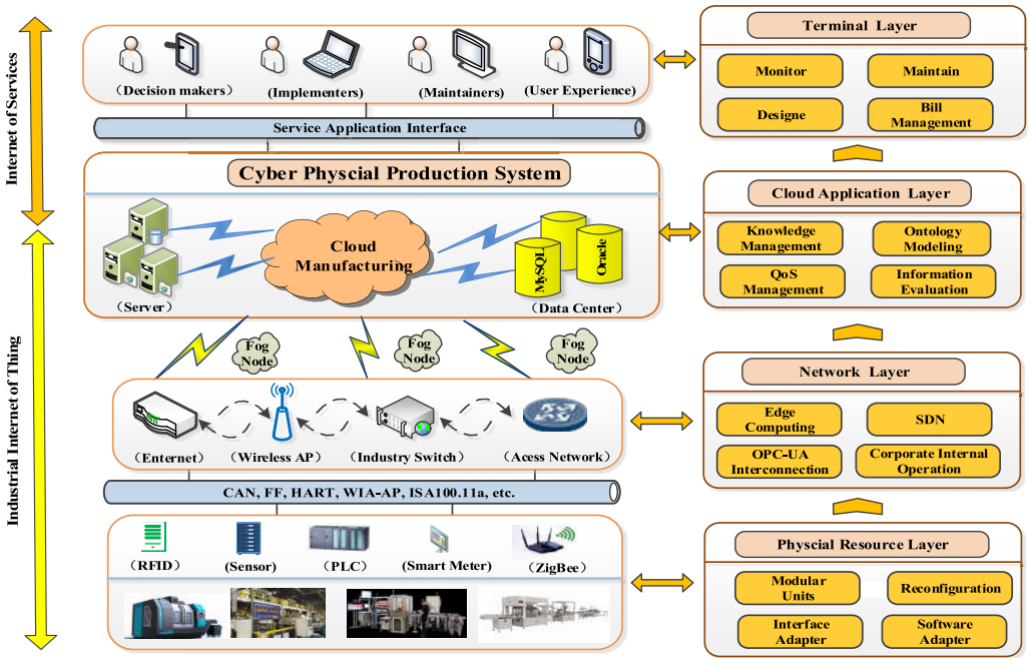

Figure 1.1: Smart factory hierarchy [4]

User Requirement		**Class 0: Safety**	**Class 1: Closed Loop Regulatory Control**	**Class 2: Closed Loop Supervisory Control**	**Class 3: Open Loop Regulatory Control**	**Class 4: Condition Monitoring**
End-to-end Latency (ms)	Typical	4	4	20	4	50
	Strict	0.5	0.25	4	0.5	4
Reliability (Pr. of Loss)	Typical	10^{-7}	10^{-7}	10^{-7}	10^{-7}	10^{-6}
	Strict	10^{-8}	10^{-7}	10^{-7}	10^{-7}	10^{-7}
Scale (# of links)	Typical	8	10	10	1	100
	Maximum	24	30	30	4	300
Range (m)	Typical	10	10	10	10	10
	Maximum	30	30	30	30	30
Payload Size (B)	Minimum	6	8	8	8	12
	Maximum	24	64	64	64	33KB
Update Rate (Hz)	Typical	125	125	25	125	10
	Maximum	1000	2000	125	1000	125

Table 1.1: Communication classes and requirements in industrial environments [8]

Table 1.1 due to its low demands, as most of nowadays implementations are capable to cope with it. These communications would fall in the Building Automation (BA) category defined in [9], where the typical applications are surveillance, illumination, temperature control and similar. The communications that belong to the fourth class or *condition monitoring* are also known as Process Automation (PA) in the literature, where the target is the monitoring of different industrial processes as mining, chemical or metallurgical. In this kind of networks, devices are usually battery powered and scattered around the industrial facilities, and the main priority is to increase their autonomy and coverage as much as possible. The classes one to three define controlled processes where sensors and actuators are employed to achieve different degrees of automation. This is aligned to the Factory Automation (FA) concept used in [9], and the most relevant aspects of this kind of communication are the reliability, latency and determinism, which are significantly more demanding compared to an average network. At last, the communications of class zero define the most stringent requirements, as they are oriented to safety integrated systems and alarm signaling.

As it is known, communications can be carried out through both wired or wireless mediums, and each alternative has its own implications. Wired communications transfer information through a dedicated medium that does not vary significantly over time, which allows to control the reach of each device, design the topology of networks with ease or detect traffic collisions. However, an infrastructure is

necessary to sustain this alternative, which presents some drawbacks as a higher cost in installation/maintenance or the low flexibility for network re-structuring. On the other hand, wireless communications exchange the information over the air, which can be accessed by installing antennas to the devices. In this case, all the devices share the same medium, which varies with time and suffers interference. Despite its drawbacks, wireless solutions are particularly interesting as they allow to implement solutions that imply a lower deployment cost, have the flexibility to adapt to different layouts or can be used in elements where movement is present.

Communication systems came first to the industrial sector in the form of fieldbus systems almost 40 years ago [10, 11, 12], which use a serial, digital data bus to connect industrial control with instrumentation. The development of this technology is a controversial topic, as each entity developed its own custom implementation and no common structure was defined for interoperability [13]. As a result, several protocols exist nowadays, some examples would be Foundation Fieldbus [14], PROFIBUS [15] or CAN [16]. The lack of interoperability and limitations of serialized communications presented several difficulties and, in order to overcome them, Ethernet based solutions were proposed later. This new approach offered several advantages as being based on a standardized and well tested protocol stack, offering a vertical hierarchy that eases the configuration or enabling the interoperability with other non-industrial networks. As fieldbuses were already implemented for the time, most of these solutions developed an adaptation mechanism that made the conversion between Ethernet and their corresponding fieldbus standard, some examples would be PROFINET IO [17], EtherCAT [18] or SERCOS III [19].

These two generations of industrial communication protocols were cable based, but as wireless protocols were gaining momentum in other sectors as home and office, the next move was to include them in industry in order to use all the previously described advantages [11]. However, as the wireless medium presents a lot of challenges, the first protocols that were proposed were not oriented to the most demanding use cases. These were mostly intended for PA applications, being the most extended solutions Bluetooth [20], ZigBee [21], Wireless Interface for Sensors and Actuators (WISA) [22], ISA 100.11a [23], WirelessHART [24] and Wireless Networks for Industrial Automation - Process Automation (WIA-PA) [25]. Nowadays, wireless communications have gained certain maturity and there are already some proposals to cover the more demanding FA use cases. These would be Wireless Networks for Industrial Automation - Factory Automation (WIA-FA) [26], WirelessHP [27], Synchronous and Hybrid Architecture for Real-time Performance (SHARP) [28] and IO-Link Wireless [29], among others. These standards operate over the 2.4 GHz

Industrial, Scientific and Medical (ISM) license-free frequency band defined by the International Telecommunication Union (ITU), which is saturated with other types of communications and interference is unavoidable. Consequently, the implementation of mechanisms to cope with this kind of environment are necessary, and this, added up to the fact that factories are considered harsh environments for electromagnetic signal propagation, makes the proposed standards not capable to cope with the most stringent use cases.

A possible solution to overcome the limitations that are present in the 2.4 GHz ISM frequency band would be to perform the communications over a different frequency band. In this regard, the ITU defines additional ISM frequency bands centered in 5.8, 24.125, 61.25, 122.5 and 245 GHz, which are license-free as well. Among these, the frequencies in the Millimeter Wave (mmWave) spectrum (30 - 300 GHz) have gained notoriety in the last decades for communication systems [30, 31], as they appear to be a promising candidate to cope with the exponential growth that communication systems are facing nowadays [32]. The main advantage of mmWave bands is their huge available bandwidth, which can be used to transmit data rates of several Gigabit Per Second (Gbps). However, these frequencies suffer a much greater propagation loss due to their shorter wavelength, and some mechanisms that counter it are necessary, the most common ones being directive antennas or beamforming techniques. Nowadays the use of this technology is being proposed for applications as telephony, multimedia, healthcare, security, autonomous driving and smart manufacturing among others [33], and two well known standard groups have included them in their newest amendments: the Institute of Electrical and Electronics Engineers (IEEE) 802.11 (versions 802.11ad and 802.11ay) and the 5G New Radio (NR) from the Third Generation Partnership Project (3GPP).

Despite the growing interest in the mmWave spectrum, very few works address the possibility of using it for industrial use cases. This idea is particularly interesting, as the extremely high available bandwidth could provide all the necessary resources to cope with the most demanding FA applications which, as described above, can not be covered with the existing solutions. The lack of a thorough analysis is attributed to the relative novelty of the communication systems that operate over the mmWave spectrum, a proof of such is that the existing related works were published less than a decade ago. The lack of a wireless standard that fully covers all the FA demands along the potential offered by mmWave frequency bands are the main motivations behind this thesis work.

1.2 Research contributions

The main contributions of this thesis are presented in this section. These can be divided in three categories, which are the characterization of electromagnetic signal propagation at 60 GHz in industrial plants, channel modelling and communication protocol testing in factory scenarios.

Regarding the first category, a double directional channel sounder that operates in the 60 GHz ISM frequency band has been developed in order to characterize the propagation of mmWave electromagnetic signals in industrial scenarios [34]. This contribution includes the design, implementation and validation of the equipment, where three independent tests are carried out to verify that the measurements made with the sounder represent the real environment. The channel sounder is later used to perform a measurement campaign that includes a workshop and a pit oven from a steel company [35], which is the second contribution of this thesis. Several positions are measured during this campaign, and the typical propagation metrics are extracted from them. All the measurements were submitted to the NIST's NextG Channel Model Alliance public repository as well [36], making them available for researchers in the academic and industrial fields.

The next category is related to the elaboration of a stochastic channel model that represents the observed propagation in industrial sites. In this contribution [37], additional measurements are carried out first with an improved resolution, this time in a mechanical workshop that belongs to Mondragon Unibertsitatea (MU). These measurements are employed to infer the parameters that represent the propagation of mmWave signals in this environment, which are used as the base for the elaboration of a stochastic channel model. This model has the aim of representing the observed scenarios in simulations, which can be useful for protocol testing. The model is validated and tested in this contribution as well, where its behaviour is proved to be in accordance with the measured data.

At last, the performance of an IEEE 802.11ad industrial network is evaluated in order to determine the suitability of a mmWave frequency based standard for the use case of interest. In this contribution [38], a simulation based approach is employed to determine the performance that the standard can offer in terms of reliability and delay, which are the critical aspects in this kind of network. To achieve this, the simulation is split in two, where the reliability of individual links is evaluated first under several conditions and two different topologies are tested later using the previously generated metrics.

1.3 Publications

Two international conferences were published at the time of writing this document. Apart from these, an additional international conference paper has been accepted, and a peer-reviewed journal has been submitted, which is currently under review. These can be found in the following sections.

1.3.1 Journals

- **Joseba Osa**, Niclas Björsell, Iñaki Val, Mikel Mendicute. "Measurement based stochastic channel model for 60 GHz mmWave industrial communications". [Manuscript submitted to the IEEE Open Journal of the Industrial Electronics Society].

1.3.2 International conferences

- **Joseba Osa**, Iban Barrutia, Jokin Cifuentes, Iñaki Val, Mikel Mendicute. “A Cost-Effective Directional Millimeter-Wave Channel Sounder for 60 GHz Industrial Wireless Communications”. In 2022 IEEE 18th International Conference on Factory Communication Systems (WFCS).

- **Joseba Osa**, Niclas Björsell, Per Ängskog, Iñaki Val, Mikel Mendicute. “60 GHz mmWave Signal Propagation Characterization in Workshop and Steel Industry”. In 2023 IEEE 19th International Conference on Factory Communication Systems (WFCS).

- **Joseba Osa**, Iñaki Val, Mikel Mendicute. "Simulation based IEEE 802.11ad performance assessment in factory workshop". [Manuscript accepted in the CSCN’23 conference].

1.4 Related activities

Additional activities that were carried out during the elaboration of this thesis are discussed in this section.

1.4.1 Assistance to international conferences

- **PIMRC2021**: The PhD student attended the IEEE 32nd Annual International Symposium on Personal, Indoor and Mobile Radio Communications (PIMRC) virtual conference as a listener, which took place on September 13-16, 2021 in

Helsinki, Finland. Topics related to the thesis as the implementation of a sub-THz channel sounder or the use of 5G NR for smart manufacturing were discussed here.

- **WFCS2022**: The PhD student attended the 2022 IEEE 18th International Conference on Factory Communication Systems (WFCS) as a listener and speaker, which took place on April 27-29, 2022 in Pavia, Italy. This conference was celebrated virtually, and the given presentation was related to the channel sounder elaborated in this thesis. Apart from this, topics as improvements for the wireless Time-Sensitive Networking (TSN) or Path Loss (PL) characterization in industrial sites were discussed, which are perfectly aligned with the scope of this thesis.
- **WFCS2023**: The PhD student attended the 2023 IEEE 19th International Conference on Factory Communication Systems (WFCS) as a listener and speaker, which took place on April 26-28, 2023 in Pavia, Italy. A presentation related to the measurement campaign carried out in industrial sites was given in this conference, and topics related to 5G, wireless TSN and reliability in industrial networks were discussed as well.
- **CSCN'23**: The PhD student will attend the IEEE Conference on Standards for Communications and Networking (CSCN'23) as a listener and a speaker on November 6-8, 2023 in Munich, Germany. A presentation will be given about the simulations of mmWave protocols in industrial settings, and discussions of topics related to communication protocols are expected from the event.

1.4.2 Collaboration with other universities

A collaboration took place between MU and Högskolan i Gävle (HiG) from the 5th of September to the 9th of December, 2022. Here, the PhD student made a stay at HiG as a guest researcher in the department of Electrical Engineering, Mathematics and Science under the supervision of Prof. Per Ängskog. The objective of the stay was to perform measurements of the propagation of mmWave electromagnetic signals in various industrial sites, using the equipment developed in MU and the contacts that the HiG group had with the local industry. A conference paper was written with all the results obtained in this work [35], and all the measured data was submitted to a public repository as well.

1.5 Structure of the thesis

This document has began with Chapter 1, where the main motivation behind this thesis is exposed and the main contributions, activities and publications are shown. From

now on, this document is structured as follows.

In Chapter 2, the main objectives and hypotheses defined at the beginning of the thesis are reviewed. The research methodology followed during the development is discussed as well, where the techniques employed during the research process are detailed.

An extensive background and literature review is presented in Chapter 3. This is divided in four sections, which are the pillars that this thesis is built on. First of all, a general introduction of the wireless medium and its properties is provided. Measurement and characterization techniques of it are discussed next, where the existing tools that perform this task are reviewed along the measurement campaigns carried out in the mmWave spectrum. Network simulation tools are shown after, and a summary of their structure and capabilities is provided as well. At last, the IEEE 802.11ad standard is analysed, since several tests are carried out over it in this thesis. The structure of the standard, as well as the works that evaluate its performance are shown in this section.

Chapter 4 describes the first development stage of the thesis, which can be divided in two main sections: the process behind the elaboration of the channel sounder and a measurement campaign performed with it. The first half of the chapter describes the components, operation and validation of the elaborated channel sounder. The other half details a measurement campaign carried out in real industrial sites, where the properties of the acquired signal are evaluated and its propagation metrics are extracted.

The stochastic channel model developed in this thesis is discussed in Chapter 5. This chapter begins by detailing an additional measurement campaign that has the aim of obtaining propagation data with a higher resolution and is employed to get the necessary information to elaborate the model. The design, parameterization and implementation of the model are detailed next, and the validation of the model is shown after. At last, some preliminary tests of the model are provided, where its performance is compared to the one of two generic indoor models.

In Chapter 6, a simulation based evaluation is done to a IEEE 802.11ad protocol managed factory network, focusing on two different use cases. Reliability and update rate metrics are measured in this test, and two different simulations are carried out to assess the performance. The first simulation focuses on individual links, where the reliability is estimated under various conditions. The other simulation works with the network as a whole, and aspects as the failure and recovery of the connections are analysed here.

At last, the main conclusions drawn from this work are exposed in Chapter 7.

Here, the main contributions are summarized first, hypotheses are validated after and future lines are proposed in the end.

Chapter 2

Objectives and Metodology

This chapter begins by summarising the objectives defined for the research. Following up, the hypotheses that this theses aims to prove are listed. The last section provides a brief introduction of the followed methodology.

2.1 Research objectives

The main objective of this thesis is to explore the behaviour of mmWave band communications in industrial settings in order to assess their viability for reliability driven use cases. In order to achieve this, the main goal is divided in several sub-objectives:

- **Objective 1:** Develop an equipment capable of measuring propagation in the mmWave spectrum.
- **Objective 2:** Acquire mmWave signal propagation measurements in real industrial sites.
- **Objective 3:** Develop a channel model to represent the propagation of electromagnetic signals in the mmWave spectrum using the previously measured sites.
- **Objective 4:** Test the capabilities of existing standards as the IEEE 802.11ad in industrial settings to assess their current capabilities.

2.2 Research hypotheses

The research carried out in this thesis will try to prove the following hypotheses:

- **Hypothesis 1:** It is possible to make accurate mmWave signal propagation measurements using low cost Commercial-Off-The-Shelf (COTS) equipment.

- **Hypothesis 2:** Industrial sites present difficulties for mmWave signal propagation due to the abundance of reflective surfaces.
- **Hypothesis 3:** The propagation of mmWave band signals in industrial sites can be approximated with mathematical formulas and stochastic processes.
- **Hypothesis 4:** Existing standard that operate over mmWave frequencies cannot meet the most stringent reliability demands of industrial communications, but modifications can be done to improve their performance.

2.3 Research methodology

This thesis has carried out all the research based on the methodology presented in [39], where an eight step process is described. This book provides three perspectives to classify the typology of research, which are the application, objectives and enquiry process. The research carried out in this thesis would fall within the following categories:

- **Application** (pure or applied): This thesis performs pure research. The main goal is to gain knowledge about the behaviour of mmWave band communications in industry, and its viability is uncertain.
- **Objectives** (descriptive, correlative, explanatory or exploratory): The research has an exploratory goal. Very few works address the idea of mmWave band industrial communications in the literature, and this thesis aims to expand the existing knowledge in this particular topic by providing related data.
- **Enquiry process** (quantitative or qualitative): This research is quantitative. The main goal is to quantify the magnitude of variance of terms as the power a signal arrives with or the achievable throughput of a network. These are measured with units that follow the international system and are unambiguous.

As for the eight step process, this can be divided in three stages depending on the development state of the research. Table 2.1 shows the complete structure of the methodology, and individual steps are discussed after.

STEP 1: FORMULATING A RESEARCH PROBLEM

The first step of a research is to decide what to investigate. This is the most important part, since all the next tasks, designs, evaluations and so on are carried out based on this decision. In practical terms, a literature review is done first in order to obtain information related to the research topic, and this process is extended along all the

THE RESEARCH PROCESS			
Phase	PHASE I	PHASE II	PHASE III
Main task	*DECIDING* ↓ WHAT (*research questions to answer?*)	*PLANNING* ↓ HOW (*to gather evidence to answer the research questions*)	*UNDERTAKING* ↓ COLLECTING (*the required information*)
Operational steps/research journey	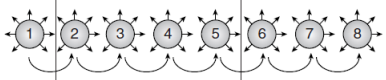		

Table 2.1: Structure of the research methodology [39]

development stages. Additionally, hypotheses can be formulated to narrow the scope of the work and generate statements that are verifiable with research.

In this thesis, the first year was dedicated almost exclusively to research the topic of reliable industrial communications and its current status, from where the problem of the lack of a standard capable of providing the performance required by the most demanding applications was identified.

STEP 2: CONCEPTUALIZING A RESEARCH DESIGN

The second step has the aim of defining all the procedures that will be followed to obtain answers to the formulated questions. In other words, how are the questions going to be answered is detailed in this step, and this is achieved by defining the study design, logistical arrangements, measurement procedures, sampling strategy, frame of analysis and the time-frame.

Each development stage of the thesis (measurement campaigns, modeling and so on) began by performing a planning about the process and expected outcome of it. Here, the tests to carry out were defined first, considering parameters as the resolution, sample size or number of iterations. Time-frame analyses were carried out as well, where the estimated duration of the measurements, development, generation of results and documentation was established.

STEP 3: CONSTRUCTING AN INSTRUMENT FOR DATA COLLECTION

The third step is oriented to the data acquisition process. Here, two kind of sources are distinguished: primary and secondary. Primary sources correspond to the ones that are made by the researcher or any related entity, whereas the secondary ones are published by an external agent as a company or the government. Quantitative tests require equipment to perform the measurements, which is developed by the researcher

in some cases. It is important to make an appropriate design, since the acquired data will be the source of the research. With a faulty device, all the obtained samples and drawn conclusions will be invalid, which is why it is important to carefully design and validate the device before making the measurements.

Part of the development of this thesis has been dedicated to the construction of a 60 GHz mmWave channel sounder for the reason detailed in this step. The selection of equipment, construction and validation were done carefully since the rest of the research is built upon the measurements obtained with this instrument.

STEP 4: SELECTING A SAMPLE

In this step, the size of the sample measured from a population is selected. Here, a trade-off is done between the sample size and the accuracy of the measurements, since the characteristics of the population are inferred from the sample and a more accurate estimation can be done with more data. However, acquiring additional data is resource-intensive, which is why this trade-off exists.

The sample size selection step was an important element of the measurement campaigns and simulations during the development of the thesis. Here, two different criteria were followed depending on the task: selecting a sample size based on similar scenario reports that can be found in the literature or using a metric as a minimum confidence interval to extrapolate the amount of required samples.

STEP 5: WRITING A RESEARCH PROPOSAL

All the preparatory work is summarized in a document in this step. Here, the research objective, hypotheses, the selected methods to find the answers and a justification for the selection are included. Its main goal is to detect any possible fault or improvement in the research plan and to validate it before carrying out the development.

In this thesis, this task was achieved by beginning to write a draft of the desired publication related to the topic under research. This draft included a literature review of similar works and a description of the work to carry out, including details regarding the testing environment, topology or layout, sample size and so on.

STEP 6: COLLECTING DATA

The measurements are carried out in this step. The size of the sample, technique, objectives and rest of the parameters were previously defined, and this step consists of implementing the accepted plan and generating all the required raw data.

As for the implementation of this step, carrying out the measurement campaigns or running the simulations would be the tasks that are correlated to it.

STEP 7: PROCESSING AND DISPLAYING DATA

In this step, the raw data is processed and the obtained results are displayed. The processing step has the goal of extracting all the relevant metrics from the data, and to

achieve this it is recommended to define the type of analysis (for example frequency distribution or correlation) and the statistical procedure to obtain this. On the other hand, the data displaying process has the aim of showing the obtained results to the readers. The predominant way to share the results is plain text, but in quantitative works this can be accompanied by tables or graphs, which makes the communication easier, clearer and more simple to understand.

In this thesis, statistical analysis has been used for data processing in several development stages like extracting propagation metrics from the measurements, elaborating the model or computing the reliability of networks. On the other hand, most results have been displayed in the form of graphs or tables, as indicated in this step of the methodology.

STEP 8: WRITING A RESEARCH REPORT

At last, a research report is written. This document contains details about all the process, beginning from the motivation of the work and going through the objective, development, obtained results and discoveries or drawn conclusions. This report must be written in an academic style, where the different topics are differentiated in chapters.

As mentioned earlier, a draft was written in step 5 where some chapters of the report were covered. In this step, the retrieved information and drawn conclusions were included in the report following the criteria established by the journal or conference the document was sent to.

Chapter 3

Background and State of the Art

The technical background of the technologies related to this thesis is presented in this chapter, and four sections are defined to achieve this. The first one, addressed as the wireless medium, provides an introduction to electromagnetic signal propagation through wireless environments. Topics as propagation delay and fading are discussed, and existing modeling solutions are described as well. The second section, which is wireless channel characterization, describes the existing techniques and implementations of equipment that is employed to measure the propagation characteristics of signals in various environments. A literature review that covers the available mmWave equipment and measurement campaigns in industrial scenarios and similar environments can be found here as well. Next, the network simulation section provides a brief introduction to the two most popular discrete-event network simulation tools that fill testing and prototyping purposes. The last section details the structure of the IEEE 802.11ad standard, as this protocol has been employed in several development stages of this thesis.

3.1 The wireless medium

As it is known, wireless communication systems use electromagnetic signals to exchange information. These signals are generated in one end known as the Transmitter (Tx) and travel to the other end, which is the Receiver (Rx), through the air, water, vacuum or any other element that separates both ends. This is what it is known as the propagation medium, which is referred as the channel in the communication system discipline as well.

The ideal channel would make the transmitted signal arrive to the destination as it is. However, this is not possible in reality as there are delay and fading effects which are inherent to the propagation of electromagnetic signals. These effects, as well ass the existing models to represent them are discussed in detail in the following sub-sections.

3.1.1 Propagation delay

The propagation delay represents the elapsed time between the transmission and and reception of a signal, which depends on the distance between both ends and the permittivity (ϵ) and permeability (μ) of the material the signals travels through. The formula to compute the propagation speed is given as

$$c = \frac{1}{\sqrt{\epsilon\mu}}, \tag{3.1}$$

where c represents the propagation speed in m/s and ϵ/μ are the permittivity/permeability coefficients relative to the vacuum ($\epsilon_0 = 8.854 * 10^{-12} F/m, \mu_0 = 1.25 * 10^{-6} N/A^2$). These coefficients are obtained for different materials through extensive measurements [40], an example of the characterization of glass (Sodium Borosilicate Glass) can be found in Table 3.1.

3.1.2 Propagation fading

The fading represents the power that is lost due to propagation of an electromagnetic signal. This phenomenon is not as straightforward as the delay, as there are several effects that take place depending on the scenario [41]. A categorization of these effects has been carried out in order to better understand all the existing mechanisms. This can be found in Figure 3.1, and a more detailed explanation is provided next.

Large scale fading

The large scale fading represents all the fading effects that are inherent to the propagation of signals. This kind of fading is noticeable at distances (d) much higher than the wavelength of the signal ($d >> \lambda$), and the attribute of interest is the power lost due to the propagation, which is known as the PL. The most simple scenario is the

Frequency (GHz)	ε*		μ*	
	ε'	ε''	μ'	μ''
8.6	4.38	0.07	1.00	0.00
9.0	4.37	0.08	1.01	0.00
9.5	4.36	0.09	1.02	0.00
10.0	4.36	0.10	1.02	0.00
10.5	4.36	0.11	1.02	–0.01
11.0	4.36	0.13	1.02	–0.01
11.5	4.38	0.14	1.01	–0.02
12.0	4.41	0.15	1.00	–0.02
12.5	4.46	0.15	0.99	–0.02
13.0	4.55	0.14	0.97	–0.03
13.4	4.63	0.11	0.96	–0.03

Table 3.1: Measured relative permittivity and permeability of glass [40]

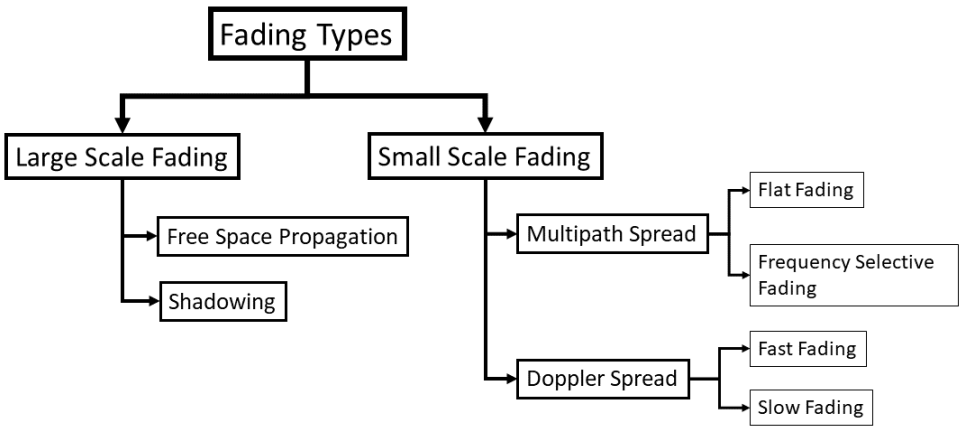

Figure 3.1: Fading categories

Free Space Path Loss (FSPL), where the signal propagates through one medium from one end to the other without any obstacle. However, all the practical scenarios are composed of additional elements as the ground, buildings, trees and more, which can provoke different effects in the propagation of the signals. These scenarios where different materials generate a partial or total obstruction in the LoS path between both ends fall within the shadow fading or shadowing category.

FREE SPACE PATH LOSS:

As stated before, the FSPL represents the fading that occurs when a signal propagates through a homogeneous, obstacle-less medium. The FSPL that a communication system suffers can be computed with the Friis Transmission Formula [42]:

$$\frac{P_r}{P_t} = G_r G_t \left(\frac{\lambda}{4\pi d}\right)^2. \tag{3.2}$$

Here, the relation between the received and transmitted power (P_r and P_t, expressed in the same unit) is computed using the gains that the antennas provide (G_r and G_t, relative to the isotropic antenna in the linear domain), the wavelength (λ in meters) and and the distance (d in meters). Assuming that both antennas are isotropic (i.e., they can be taken out from the equation), the FSPL can be characterized using only the distance and wavelength. If the wavelength is replaced with its definition (c/f), some interesting conclusions can be drawn, which are that there is a quadratic increase in the loss if the distance or frequency are incremented or the propagation speed (which is computed with the formula provided in (3.1)) is decreased.

As a final note, this formula is valid only for far field scenario. As it is known, two different regions are defined when antennas send or receive electromagnetic waves: the near field when the point of interest is close to the antennas and the far field when there is a certain separation between both. Near field scenarios are particularly

challenging to estimate, as the antenna body and objects located in proximity can change the radiated signal drastically, as well as containing reactive effects along radiative ones. In order to discern both fields the Fraunhofer distance formula can be found in the literature [43], which allows to compute an approximated distance that delimits them. This is expressed as

$$r = \frac{2D^2}{\lambda}, \tag{3.3}$$

where *r* represents the delimiter distance in meters, D is the largest antenna dimension represented in meters and λ expresses the wavelength of the radiated signal in meters.

SHADOW FADING:

The shadow fading represents the loss of a signal due to the presence of an obstacle. In this case, electromagnetic signals need to change the propagation medium in order to keep moving forward, and several effects can take place depending on the dimensions and material of the new medium. The observable effects are detailed in the following list:

- **Reflection:** The signal does not propagate to the new medium. Instead, it bounces in the area that separates both media and continues to propagate in the original medium with a different direction, amplitude and phase.
- **Refraction:** The signal traverses through the new medium changing its direction, amplitude and phase.
- **Diffraction/Scattering:** This effect happens when the surface that delimits both media is irregular. In this case, the signal propagates through several directions with no predominant component.
- **Absorption:** The signal looses strength while propagating through the new medium to the point where it is no longer detectable.

A graphical representation of all the aforementioned effects can be seen in Figure 3.2. As it can be observed, the direction of the reflected/refracted wave can vary depending on the scenario, which is an effect that depends on the refractive indices of the materials and the phase gradient that presents the surface that separates both media. Both reflection and refraction angles can be computed with the generalized Snell's law [44]:

$$sin(\theta_2)n_2 - sin(\theta_1)n_1 = \frac{\lambda_0}{2\pi}\frac{d\phi}{dx}, \tag{3.4}$$

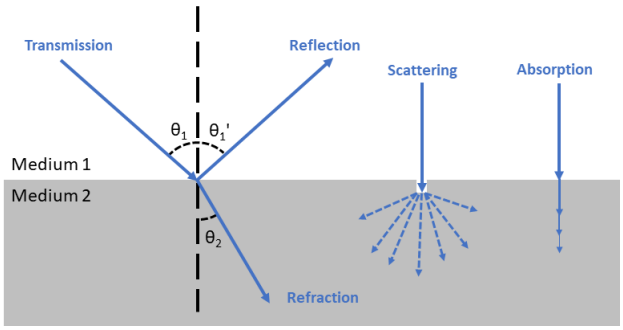

Figure 3.2: Electromagnetic signal propagation effects due to change of medium

$$sin(\theta_1') - sin(\theta_1) = \frac{\lambda_0}{2\pi n_1}\frac{d\phi}{dx}. \tag{3.5}$$

The refraction and reflection angles can be computed with these equations, where n_1 and n_2 represent the refractive indices, λ_0 is the wavelength of the electromagnetic signal in vacuum and $d\phi/dx$ contains the phase gradient that the surface presents.

As for the strength of both transmitted and reflected waves, these are computed with the Fresnel's equations [45]. Two different sets of equations are provided depending on the polarization of the signal, which can be *p* polarization when the electric field is parallel to the plane of incidence or *s* polarization when the magnetic field is the parallel one. The transmitted and reflected power are computed as

$$\begin{aligned} T_p &= \frac{2n_1\cos\theta_1}{n_2\cos\theta_1 + n_1\cos\theta_2}A_p \\ T_s &= \frac{2n_1\cos\theta_1}{n_1\cos\theta_1 + n_2\cos\theta_2}A_s \end{aligned}, \tag{3.6}$$

$$\begin{aligned} R_p &= \frac{n_2\cos\theta_1 - n_1\cos\theta_2}{n_2\cos\theta_1 + n_1\cos\theta_2}A_p \\ R_s &= \frac{n_1\cos\theta_1 - n_2\cos\theta_2}{n_1\cos\theta_1 + n_2\cos\theta_2}A_s \end{aligned}, \tag{3.7}$$

respectively. Here, *A* represents the amplitude of the electromagnetic signal, which later splits in to the reflected (*R*) and transmitted (*T*) amplitudes. Following the energy conservation principle, *A* should be the sum of *T* and *R*. The other parameters, which have been previously introduced, represent the refractive indices of the media (n_1, n_2) and the incidence/refraction angles (θ_1, θ_2).

Small scale fading

Small scale fading effects occur due to a rapid fluctuation in the amplitude of an electromagnetic wave. This kind of fading can appear sporadically and its effects

are perceived in a very small spatio-temporal window ($d >= \lambda$). There are two well documented effects that fall within the small scale fading, which are multipath fading and doppler spread. Details regarding each one can be found in the following paragraphs.

MULTIPATH FADING:

Multipath fading takes place when a transmitted signal reaches the receiver through various routes as the LoS component and paths that reflect on surfaces as buildings, the ground, cars or trees that belong to the environment. An example can be found in Figure 3.3.

In this case, multiple copies of the transmitted signal arrive to the destination with different amplitudes, delays and phases. These copies are combined in the receiver, where depending on the scenario can suppose constructive or destructive interference. Communication systems must be designed with the capability to cope with this effect, which can vary significantly depending on the scenario. A common practice to determine the impact of the multipath elements is to analyse its dispersion in both spatial and temporal domains.

The dispersion that multipath presents in time is computed with the Root Mean Square (RMS) Delay Spread (DS) parameter [46], which represents the square root of the second central moment. The formula to compute this value is

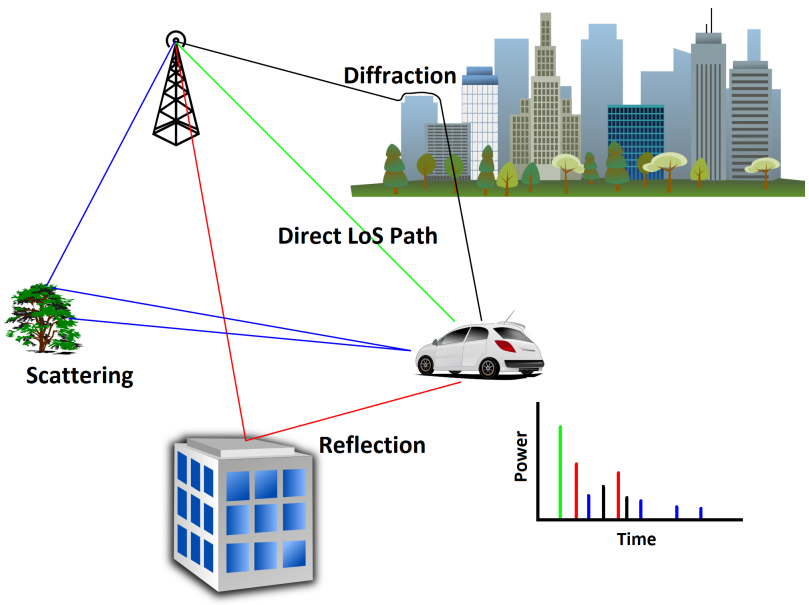

Figure 3.3: Multipath propagation example

$$\begin{aligned} \tau_{RMS} &= \sqrt{\frac{\sum_{n=1}^{N}(\tau_n - T_D)^2 P_n}{\sum_{n=1}^{N} P_n}} \\ T_D &= \frac{\sum_{n=1}^{N} \tau_n P_n}{\sum_{n=1}^{N} P_n} \end{aligned}, \tag{3.8}$$

where *N* represents the amount of multipath components, (τ_n,P_n) are the delay and power of the n^{th} component and T_D is the mean delay.

The spatial dispersion is computed in a similar fashion. Depending on the available information, the angular dispersion that is presented in transmission or reception is computed for the azimuth or elevation planes separately. The corresponding formulas to compute this value are

$$\begin{aligned} \phi_{RMS} &= \sqrt{\frac{\sum_{n=1}^{N}\left(\phi_n - \bar{\phi}\right)^2 P_n}{\sum_{n=1}^{N} P_n}} \\ \bar{\phi} &= \frac{\sum_{n=1}^{N} \phi_n P_n}{\sum_{n=1}^{N} P_n} \end{aligned}, \tag{3.9}$$

where ϕ_n is the angle of the n^{th} multipath component in the plane of interest and $\bar{\phi}$ represents the mean angle.

Another parameter that must be considered during the communication system design is the coherent bandwidth. This is related to the DS of the multipath, and it represents the amount of frequencies that have a flat fading (i.e. the same gain and linear phase for all the components). If the bandwidth of the transmitted signal exceeds this threshold, this condition is no longer maintained and fading is said to be frequency selective. Even if the coherent bandwidth is related to the DS, there is not a straightforward formula to compute the relationship between them and an approximation is required [41]. The approximations of the threshold for 90% and 50% correlation between frequencies is detailed next:

$$\begin{aligned} B_c &= \frac{1}{50\tau_{RMS}}(90\%) \\ B_c &= \frac{1}{5\tau_{RMS}}(50\%) \end{aligned}. \tag{3.10}$$

DOPPLER SPREAD:

The doppler spread accounts for scenarios where a moving element is present. This element can be the transmitter, receiver, any object that generates a multipath component

or a combination of all of them. The relative movement between the transmitter and receiver is perceived as a shift in the carrier frequency, as the phase shift of the received signal increases when both ends approach each other and decreases when they move in opposite directions. This makes the perceived wavelength have a different dimension, which means that the frequency is different as well. A graphical representation of this phenomenon can be found in Figure 3.4, and the expected frequency can be computed as

$$f = \frac{c \pm v_{Rx}}{c \pm v_{Tx}} f_0. \tag{3.11}$$

Here, the original frequency is expressed as f_0 in Hz, c represents the propagation speed of light in *m/s* and (v_{Tx}, v_{Rx}) are the relative speeds between both ends in *m/s*. As for the sign, $(-v_{Tx}, +v_{Rx})$ is used when the objects are approaching and $(+v_{Tx}, -v_{Rx})$ for receding.

The relative movement between both ends makes the communication channel vary with time, which can distort the received signal. Depending on the expected Doppler spread, the channel will remain invariant for certain duration, which is known as the coherent time in the literature. If the duration of a transmission is lower than this threshold, the signal does not suffer any significant variation. This is defined as a slow fading scenario. On the other hand, using a bandwidth superior to the threshold provokes the signal to change during the transmission, which is known as a fast fading scenario. As in the case of the coherent bandwidth, there is not a straightforward formula to compute the maximum time and several approximation can be made to obtain this value. Modern digital communication systems use the one defined in [41]:

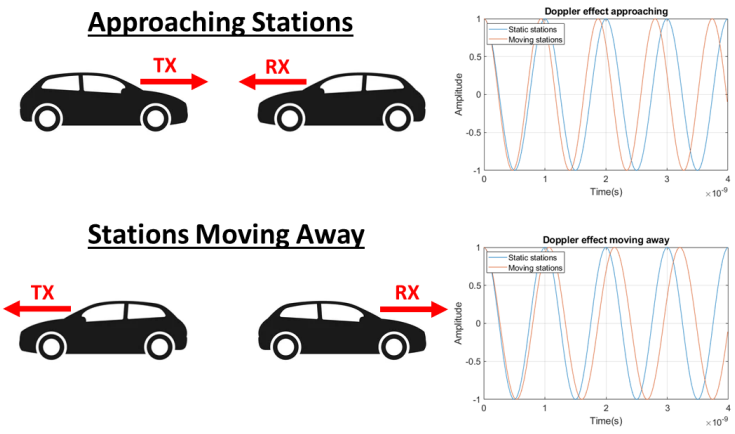

Figure 3.4: Doppler effect example

$$T_c = \sqrt{\frac{9}{16\pi f_m^2}}, \tag{3.12}$$

where the coherence time (T_c) is expressed in seconds and f_m represents the maximum Doppler frequency ($f_m = v/\lambda$).

3.1.3 Modeling of fading

As it can be deduced from the previous section, the fading that a transmitted signal suffers can be affected by several elements, which can be challenging to represent in simulated environments. Instead of including all the aforementioned effects, simulation tools tend to use techniques to approach the expected fading effect, and these can be divided into two categories: stochastic and deterministic.

Stochastic models use a probabilistic distribution to represent fading. Different distributions are proposed in the literature for scenarios that have LoS/Non Line of Sight (NLoS), a variation in time or rapid fluctuations in the CIR.

On the other hand, deterministic models use in-site measurements of an environment to obtain the fading. These models only represent large scale fading (i.e. PL and shadowing), and they are elaborated based on statistical inference over the measured data.

The following sections provide details regarding both modeling approaches.

Stochastic fading distributions

There are four well extended probabilistic distributions in the literature to represent fading of electromagnetic signals, which are the Rayleigh, Ricean, Weibull and Nakagami distributions. Details regarding each can be found next.

RAYLEIGH DISTRIBUTION:

The Rayleigh distribution is used to represent the time varying aspect of the fading that a multipath component suffers [41]. This is achieved by computing the real and imaginary components of the signal as two independent and identically distributed Gaussian variables with zero mean and equal variance, and its Probability Density Function (PDF) can be computed with the following formula:

$$p(r) = \begin{cases} \frac{r}{\sigma^2} exp\left(-\frac{r^2}{2\sigma^2}\right) & ,(0 \leq r \leq \infty) \\ 0 & ,(r < 0) \end{cases} . \tag{3.13}$$

Here, the variance (σ^2) represents the time-averaged power of the received signal, and the PDFs of some examples can be seen in Figure 3.5.

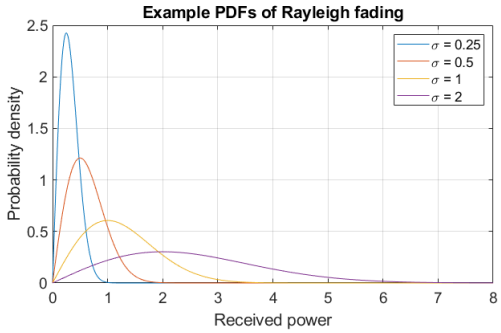

Figure 3.5: Example PDFs of Rayleigh fading

RICEAN DISTRIBUTION:

Ricean distribution represents the fading of a signal when a dominant component as the LoS path is present [41]. Here, the LoS element adds a constant gain that can be significantly larger than the variation of the signal, which is computed with a formula similar to the Rayleigh fading. The PDF of this distribution is shown next

$$p(r) = \begin{cases} \frac{r}{\sigma^2} exp(-\frac{r^2+A^2}{2\sigma^2}) I_0\left(\frac{Ar}{\sigma^2}\right) & ,(A \geq 0, r \geq 0) \\ 0 & ,(r < 0) \end{cases} , \tag{3.14}$$

where I_0 is the modified Bessel function of the first kind with zero order and A represents the maximum amplitude of the dominant component.

This model is typically configured with the Rician-K parameter, which determines the power ratio between the dominant component and multipath elements. The K factor is computed as

$$K(dB) = 10log\left(\frac{A^2}{2\sigma^2}\right) dB, \tag{3.15}$$

and some PDF examples for several values are provided in Figure 3.6.

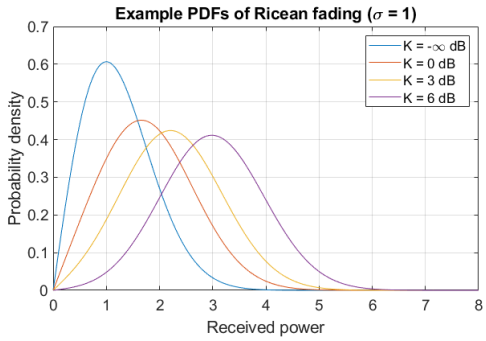

Figure 3.6: Example PDFs of Ricean fading

WEIBULL DISTRIBUTION:

The Weibull distribution is used to represent fading as well, even if its applications are not limited to communication systems [47]. This probabilistic distribution uses a parameter *k* to determine the shape of the PDF, where the highest probability density is clustered in the left or right ends depending on its sign. The formula to compute its PDF is

$$p(r) = \begin{cases} \frac{k}{\lambda}\left(\frac{r}{\lambda}\right)^{k-1} exp(-(r/\lambda)^k) & ,(A \geq 0, r \geq 0) \\ 0 & ,(r < 0) \end{cases}, \tag{3.16}$$

where two configuration parameters can be seen: the shape (k) and the scale (λ). Some PDF examples are provided in Figure 3.7. As a final note, there is a special case where a Rayleigh distribution can be generated using this method, which is when the (k, λ) parameters adopt the $(2, \sqrt{2}\sigma)$ values.

NAKAGAMI DISTRIBUTION:

The Nakagami distribution is another popular stochastic model that represents fading [48]. Two different parameters are used here to control the structure of the PDF, which are the shape ($m \geq 0.5$) and scale ($\Omega > 0$). The formula to compute the PDF of this distribution is

$$p(r) = \frac{2m^m r^{2m-1}}{\Gamma(m)\Omega^m} exp(-(m/\Omega)/r^2), \tag{3.17}$$

and some examples can be found in Figure 3.8.

Deterministic Path Loss models

Three main deterministic PL models can be found in the literature: Close-In (CI), Floating Intercept (FI) and Alpha-Beta-Gamma (ABG). Even if nowadays extended versions of them do exist (including dual slopes, antenna polarization, etc.), this

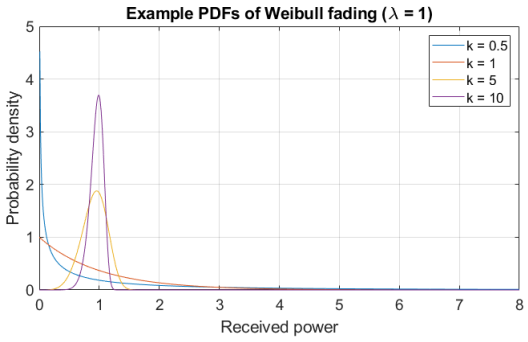

Figure 3.7: Example PDFs of Weibull fading

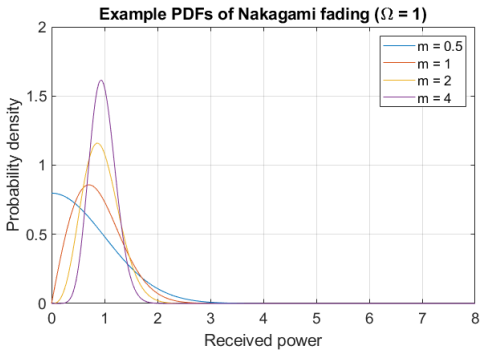

Figure 3.8: Example PDFs of Nakagami fading

document will only cover their basic forms as it is intended to provide only an introduction to the topic. Details regarding the three models are provided next.

CLOSE-IN MODEL:

The CI model uses the FSPL at a fixed distance (usually 1 meter) as a reference and computes the distance dependant loss by offsetting this value. The offset is computed with a statistically inferred parameter known as the path loss exponent (n), which has a value of 2 for the propagation in vacuum. The shadow fading is computed with the difference between the measured powers and inferred values, and the model represents it with an random Gaussian variable with the $N(0, MeanSquaredError(MSE))$ distribution. The formula to represent this model is

$$PL^{CI}(f,d)[dB] = FSPL(f,d_0) + 10nlog_{10}\left(\frac{d}{d_0}\right) + X_\sigma^{CI}, \tag{3.18}$$

where $FSPL(f,d_0)$ represent the PL for the frequency f at a reference distance d_0 (typically 1 meter) computed with the Friis transmission equation (3.2), d represents the distance between the transmitter and receiver and X_σ^{CI} is the random Gaussian variable that includes shadowing.

FLOATING INTERCEPT MODEL:

The FI model performs a linear regression of the measured powers vs their corresponding distances. This operation yields two results: the intercept (α) and distance dependant slope (β). As with the CI model, shadowing is represented with a random Gaussian variable that follows a $N(0, MSE)$ distribution as well. The equation that represents this model is

$$PL^{FI}(d)[dB] = \alpha + 10\beta log_{10}\left(\frac{d}{d_0}\right) + X_\sigma^{FI}, \tag{3.19}$$

where the distance is d and X_σ^{FI} represents the Gaussian distribution that includes shadowing.

ALPHA-BETA-GAMMA MODEL:

The ABG model is employed when measurements from multiple frequency bands are available. This model can be seen as an extension of the FI where the frequency is included as an additional independent variable. The name comes from the three parameters that characterize this model, which are a distance dependent value (α), the intercept point (β) and frequency dependent component (γ), and a multivariate regression is performed to the samples in order to obtain them. As in the previous cases, a random Gaussian with $N(0, MSE)$ distribution represents the shadowing effect. The structure of this model is the following one:

$$PL^{ABG}(f,d)[dB] = 10\alpha log_{10}\left(\frac{d}{d_0}\right) + \beta + 10\gamma log_{10}\left(\frac{f}{f_0}\right) + X_{\sigma}^{ABG}. \quad (3.20)$$

3.1.4 Stochastic propagation models

The previous section has introduced the most common stochastic fading distributions, which are a simple alternative to model the fading of electromagnetic signals in simulated environments. However, this is not sufficient to fully represent the propagation of signals, as other elements as delay, multipath or Doppler need to be considered as well. In this regard, there are additional stochastic models in the literature that use more parameters in order to generate channel models that resemble more to real environments. This document will only introduce three basic models as it is intended to provide just an introduction to the topic. These models are the following: Two-ray ground-reflection, Tapped Delay Line (TDL) and Saleh-Valenzuela (S-V), and details regarding each can be found in the following sections.

Two-ray ground-reflection model

The two-ray ground-reflection model uses two multipath components to represent the propagated signal between two stations: the LoS element and a reflection that occurs on the ground between both ends. A graphical representation of this model can be found in Figure 3.9.

This model computes the delay and fading of the signal in both paths, which can be calculated following several criteria. In [41], an approximation that uses the Rayleigh fading is proposed, where the CIR is computed as follows

$$h(t) = \alpha_1 exp(j\phi_1)\delta(t) + \alpha_2 exp(j\phi_2)\delta(t-\tau). \quad (3.21)$$

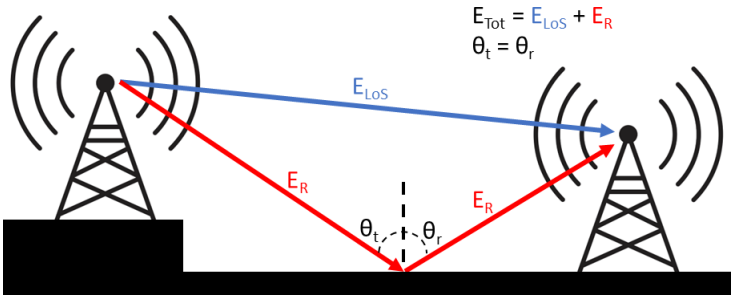

Figure 3.9: Two-ray ground-reflection model

Here, (α_1, α_2) represent two independent Rayleigh distributions, (ϕ_1, ϕ_2) are two random variables that follow a uniform distribution in the $[0..2\pi)$ range and τ contains the elapsed time between both multipath components.

On the other hand, [46] proposes an equation that computes the received power with the FSPL propagation formula (3.2), as well as (3.7) for the ground reflected power. This formula is

$$P_R = P_T \left(\frac{\lambda}{4\pi}\right)^2 \left| \frac{1}{d_{LoS}} exp(-jkd_{LoS}) + \rho \frac{1}{d_R} exp(-jkd_R) \right|, \tag{3.22}$$

where the received power (P_R) is represented as an addition of two FSPL components that are multiplied by the transmitted power (P_T). In this addition, (d_{LoS}, d_R) represent the length of both LoS and reflected paths in meters, ρ is the reflection coefficient of the ground and k is the wave number ($k = 2\pi/\lambda$). As it can be seen, both gains are added constructive or destructively depending on their relative phases before performing the multiplication with the transmitted power.

Tapped Delay Line model

The TDL model is a widely adopted solution that provides a simple representation of the multipath fading where the received signal is composed of an addition of various copies of the transmitted one, each having its own gain, delay and phase. Figure 3.10 shows the structure described above, where delayed copies of the transmitted signal are multiplied with their corresponding phases and gains and all the products are added to generate the received signal.

This can be represented with the formula

$$h(\tau) = \sum_{i=0}^{N} A_i exp(-j\phi_i)\delta(\tau - \tau_i), \tag{3.23}$$

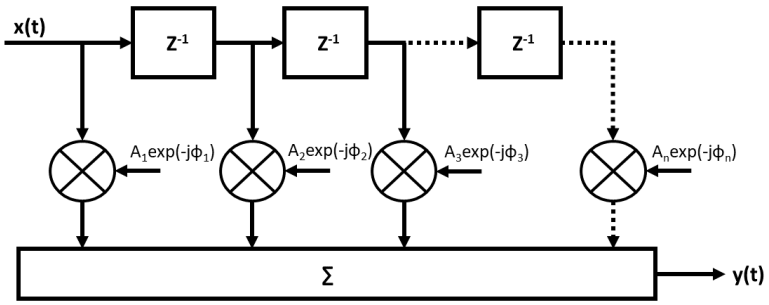

Figure 3.10: TDL propagation model structure

where N is the total amount of multipath components and (A_i, ϕ_i, τ_i) contain the gain, phase shift and delay of the *i*-th component.

The model can be expanded to include the time variation of the channel. Here, the time (t) domain is included in addition to the delay (τ), being their relation $(\Delta t >> \Delta\tau)$. The time domain represents the elapsed time from the beginning of the simulation, and the channel is assumed to be invariant between two consecutive values of t. The delay domain represents the time as an offset to be added to the corresponding t value. In other words, t can be understood as a global timestamp and τ as an offset that is added to it, and the channel suffers variation only when the value of t is modified. This extension can be expressed as:

$$h(t,\tau) = \sum_{i=0}^{N} A_i(t,\tau) exp(-j(2\pi f_c \tau_i(t) + \phi_i(t,\tau)))\delta(\tau - \tau_i(t)). \tag{3.24}$$

Saleh-Valenzuela model

The S-V model was presented in [49], where the work was originally intended to characterize an indoor multipath channel and fit it to a TDL model. However, the authors noticed that the arriving rays could be grouped by their proximity in power/delay (which is referred as *cluster* in the work) and proposed their own model to represent them more accordingly. The clustering of rays is expressed as

$$h(t) = \sum_{l=0}^{L} \sum_{k=0}^{K} \beta_{kl} exp(j\theta_{kl}) \delta(t - T_l - \tau_{kl}), \tag{3.25}$$

where (l, k) indicate the cluster and ray indices, β is the amplitude of the multipath component, θ_{kl} is the phase shift of the ray and (T_l, τ_{kl}) represent the time offset of the *l*-th cluster and *k*-th component within it, respectively.

The model is intended to use with one main *Poisson arrival process* that determines the arrival time of each cluster. Then, each cluster has its own Poisson distribution that determines the additional delay of the individual rays. This can be seen as a multipath environment where the signals bounces through several irregular surfaces. In this example, a cluster would be a path that goes through the same surfaces, and the rays would represent all the points within a surface that have a reflection that points towards the receiver. Figure 3.11 shows the design and implementation of this model.

3.1.5 Deterministic propagation model: Ray Tracing

All the channel model techniques introduced until now have an element of randomness that is extrapolated from some observations. However, it is possible to make an accurate prediction of the propagation of electromagnetic signals in any environment if some properties as the geometry of the medium, the electrical properties of the materials or the antenna radiation patterns are known. This kind of simulation uses these properties along Maxwell's equations to determine the expected CIR of the scenario in a deterministic manner, and the most extended implementation of this concept in the literature is called Ray Tracing [50].

In ray tracing simulations, a Tx/Rx pair is analysed in a known scenario as an indoor office, living room, any urban environment or similar, and the expected propagation paths are calculated between both ends. This can be achieved following several criteria, but there are two main methods that can be found in the literature: the *Image method* and *Shooting and Bouncing Ray (SBR) method*.

The image method estimates the path of a ray by translating one end around the surface of the incidence. An example is provided in Figure 3.12 to show how does this technique work. This process can be repeated recursively when multiple reflections form part of the path, and in general it is more computationally demanding than SBR, which is why it is not well suited for dense environments.

On the other hand, the SBR method performs a scan that involves a partial or complete coverage around the transmitter in order to determine if a path arrives to

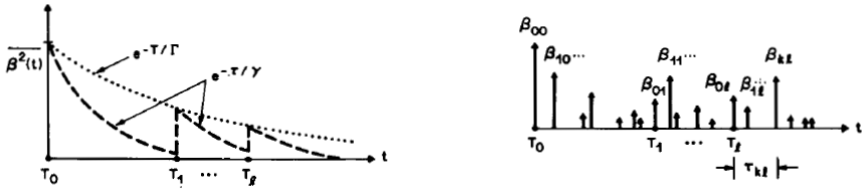

(a) Averaged cluster power in S-V model

(b) Realization of S-V model

Figure 3.11: Behaviour of S-V stochastic channel model [49]

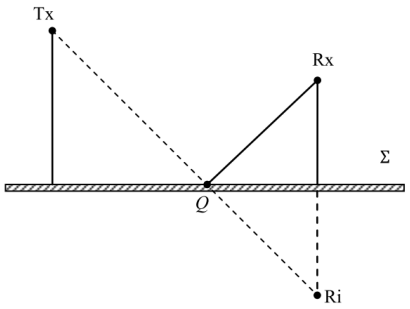

Figure 3.12: Ray tracing with image method [50]

the destination or not. This process can be divided in three main steps, which are the ray launching, tracing and reception. First, the ray launching step generates rays that propagate in directions that are distributed as uniformly as possible. Then, the propagation step calculates if the ray reaches the desired destination or not, considering reflections as well. At last, the reception determines the validity of the arrived signal, as well as its power and delay.

3.2 Wireless channel characterization

As described in the previous section, several effects take place when a signal propagates through a wireless medium. When a communication protocol that operates over this medium is designed, all these effects must be taken in consideration, as it is essential to provide mechanisms to cope with them in order to guarantee a minimum performance. To achieve this, the first step is to analyse the propagation characteristics of the medium which the communication system will be used over, and all this information is obtained through experimental measurements because the complexity of real environments cannot be fully represented with mathematical or simulation based approximations in most cases. The device used to acquire this information is known as a channel sounder.

A channel sounder is an equipment that uses a known electromagnetic signal pattern in the medium of interest in order to perform a scan of its surroundings. This equipment is composed of four different parts: the signal generator, transmitter, receiver and a signal acquisition device. These are selected based on the desired information, as a channel sounder can measure different parameters as the ones listed below:

- **Delay:** The elapsed time between the transmission and reception of a signal. If the propagation speed is known, it can be used to measure distance as well.

- **Fading:** The power lost due to the propagation of the signal, shadowing, reflection, refraction and diffraction effects.
- **Angular dispersion:** If directional antennas are employed, it is possible to know the departure and arrival angles of a path both in the azimuth and elevation planes.
- **Doppler shift:** A variation of the received signal due to a relative movement of an element, which can be part of the sounder or any surface in its surroundings.

The most suitable channel sounder design will vary depending on the information of interest, as a simple implementation will suffice for the most basic applications and more complex solutions are needed to increase the precision. All the channel sounding techniques, as well as existing implementations and measurement campaigns that have been carried out in the mmWave spectrum are discussed next.

3.2.1 Channel sounding techniques

This section introduces five channel sounder designs that are widely known in the literature. These are the single tone Continuous Wave (CW), frequency modulated CW, pulse waveform, sliding correlator and frequency domain sounders, and details regarding each can be found next.

Single tone CW sounder

The single tone CW sounder is the most simple implementation that can be found in the literature, as it only uses a single frequency tone to perform the characterization. A graphical representation can be found in Figure 3.13, and both the transmitted and received signals can be represented as

$$\begin{aligned} x(t) &= cos(2\pi f_c t) \\ y(t) &= \sum_{i=1}^{N} A_i cos(2\pi f_c (t - \tau_i)) \end{aligned}. \tag{3.26}$$

As it can be observed, each of the received paths has its own amplitude (A_i) and delay (τ_i), which means that the received tone i will be an attenuated and phase

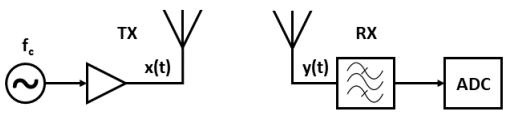

Figure 3.13: Single tone CW sounder scheme

shifted copy of the transmitted one. As the phase of a signal repeats periodically, it is impossible to know the total delay solely with the phase shift (a phase shift k and $2\pi N + k$ are the same for any integer number N), and the maximum distance that can be represented without ambiguity is the wavelength of the tone (λ).

For this reason, this kind of sounder is not well suited to retrieve the delay/distance of a multipath component. However, it can be useful to get the fading of the signal or Doppler shift while maintaining an extremely simple design, which is why it is a useful solution despite its limitations.

Frequency modulated CW sounder

The frequency modulated CW sounder can be seen as an extension of the single tone version where a signal of varying frequency is transmitted instead of a fixed tone. This manages to provide measurements of a wider area in the electromagnetic spectrum, which adds additional resolution in the time domain as well. The sounding signal is typically a sinusoidal wave that increases its frequency linearly over time between a minimum and maximum frequencies. This is known as the chirp signal in the literature, and it can be modeled as

$$x(t) = Acos\left(2\pi\left(ft + \frac{B}{2T}t^2\right)\right), \tag{3.27}$$

where the start frequency is expressed as f, the total bandwidth is B ($B = f_{max} - f$) and the total duration of the frequency sweep is T. An example of the chirp signal generated with this formula can be found in Figure 3.14, where the frequency range of 100 Hz - 1 kHz and a total duration of 100 ms have been selected.

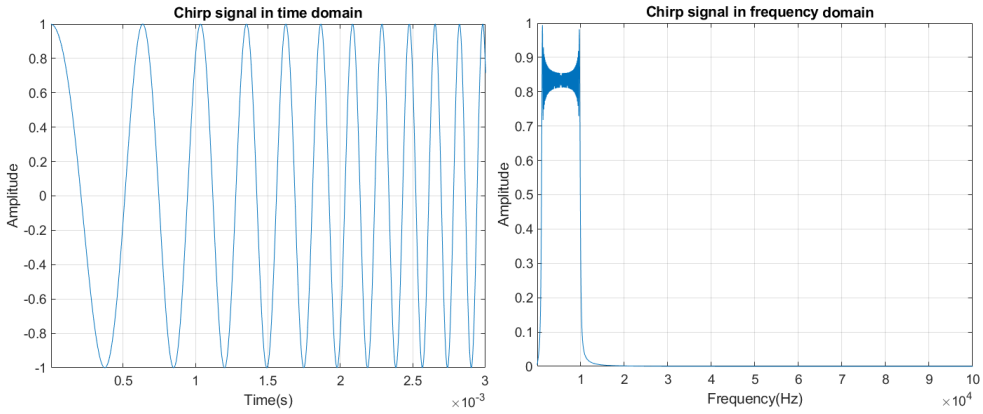

(a) Time domain (b) Frequency domain

Figure 3.14: Time and frequency domain representation of chirp signal

A sounder that transmits this kind of signal is equipped with a structure known as *matched filter* in reception that allows to recover the CIR. This filter generates the same chirp signal as the transmitted one with the opposite slope, and combining it with the input generates a compressed pulse, which is the product of delaying all the frequencies and phasing them in the same instant. This pulse has the shape of the *sinc* function, and its peak power is $10log(BT)$.

Pulse waveform sounder

An additional waveform that can be used for channel sounding is the pulse train, which consists of a periodically repeating signal that is set to the *on* state for a short interval and *off* during the rest of the period. Figure 3.15 shows the structure of this kind of signal, which is described with two parameters: the period (T) and the active interval (τ).

The active interval determines the maximum temporal resolution that can be achieved with the sounder, as two paths that contain a delay difference which is less than τ will be added in the receiver side as constructive or destructive interference. On the other hand, T defines the maximum resolvable delay of the system, which defines the maximum path distance that can be measured.

It is important to consider the environment when the parameters of the pulse signal are defined. A shorter active interval yields more precise results, but in order to achieve it the system must operate at a higher frequency. The total duration must be adjusted as well, because setting a low value can provoke an overlap between pulses from two adjacent periods and too long periods will make the system inefficient.

Sliding correlator sounder

The sliding correlator channel sounder uses a single tone signal that is spread over a large bandwidth. To achieve this, the carrier is phase modulated with a Pseudo-random Noise (PN) sequence which is typically binary (0º or 180º shift). There

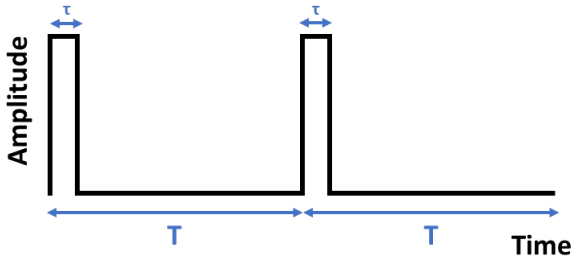

Figure 3.15: Pulse train signal

are several techniques to generate such sequences, but the most extended one is the Pseudo-Random Binary Sequence (PRBS) which is generated with a Linear Feedback Shift Register (LFSR) as the one that can be seen in Figure 3.16. This structure can be initialized with any non-zero sequence, and each iteration will output a single binary value and update all the registers, using the XOR combination of several outputs to compute the new value of the first register. The outputs that will be used to compute the new value are defined in the primitive polynomial of the LFSR, which is a mathematical formula that describers its behaviour. A LFSR that is composed of N register can have a maximum length of $2^N - 1$ (all the combinations of the registers except the all-zero case), which can only be obtained with specific primitive polynomials as the one used in the example of Figure 3.16. This case is known as Maximum Length Sequence (MLS) in the literature and is particularly interesting for use cases as channel sounding.

The structure of this kind of sounder is shown in Figure 3.17. As described above, a carrier frequency f_c is phase modulated with a PRBS in the transmitter, which is clocked at a rate r. The achievable time resolution of this setup is $1/r$, and if N is the total amount of states that the LFSR can have, the maximum resolvable delay will be of rN. In reception, the same sequence is generated and correlated with the received signal in order to retrieve the CIR, but this sequence is clocked at a slightly slower rate r'. This is a technique known as sliding correlator, and it provides a significant processing gain to the received signal.

The sliding correlator technique uses a specific clock rate in the receiver in order to make both sequences match once every γ periods of the transmitter, which is calculated as

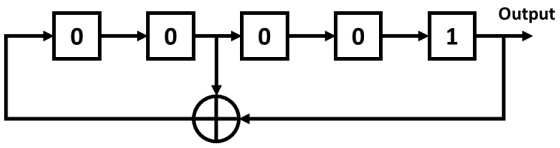

Figure 3.16: Linear Feedback Shift Register with $x^5 + x^2 + 1$ primitive polynomial

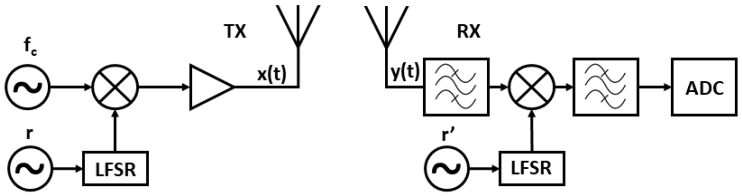

Figure 3.17: Sliding correlator sounder scheme

$$\gamma = \frac{r}{r - r'}. \tag{3.28}$$

The receiver performs the correlation with an time offset that increases by rN/γ every transmitter sequence period and stores the CIR value for that specific offset. This process is repeated for all the possible offset values between the transmitter/receiver sequences, and when it is completed, γ samples will be available in the rN interval instead of just N, effectively increasing the temporal domain resolution.

The main advantage of this technique is that the achievable resolution is much higher than the speed of the clocks employed in the system. However, both clocks need to operate at exact rates in order to implement it successfully, and the channel must remain invariant during γ transmission periods, which can be limiting factors for the implementation of this kind of sounder.

Frequency domain sounder

A VNA is a device that allows to analyse the scattering parameters (also known as S-Parameters) of a system when it is stimulated with electrical signals of various frequencies. It is possible to use this equipment to measure a CIR as well, because the time domain response of a signal can be retrieved from its frequency response via the Inverse Discrete Fourier Transform (IDFT) operation. The structure of this kind of sounder is extremely simple, as the antennas used for transmission and reception are attached directly to the VNA with coaxial cables, Figure 3.18 shows an example of this implementation.

Two main parameters determine the capability of this kind of sounder: the bandwidth and frequency spacing. The bandwidth B ($B = f_{max} - f_{min}$) determines the temporal resolution of the CIR, as the samples are spaced by $1/B$ seconds. On the other hand, the frequency spacing refers to the amount of tones that are tested within the bandwidth because, as it is known, VNAs perform the characterization with N

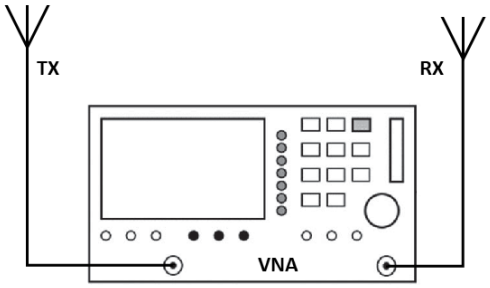

Figure 3.18: Frequency domain sounder scheme

equidistant frequency tones. In this case, N determines the length of the CIR as well as the maximum resolvable delay.

Due to its simplicity, this kind of channel sounder presents some limitations. In some cases, it is necessary to include an external power amplifier because the outputted power of a VNA can be lacking depending on the scenario. Apart from this, the acquisition time is also elevated, which means that this design is limited to static channel characterization. In addition, the cable and antenna delay and losses must be considered and compensated from the S-Parameter as well, which can be challenging depending on the available equipment.

3.2.2 Channel sounder implementations in the mmWave spectrum

As described in the previous section, sounding can be carried out using different techniques and the best approach will vary depending on the scenario and metrics of interest. Nowadays, several sounders that follow the aforementioned structures have been implemented but this work has only analyzed solutions that operate over the mmWave spectrum, as it is the main focus of this thesis. In these frequency bands, the PL is significantly larger and communication protocols use far more bandwidth, which is why channel sounder designs from lower frequencies do not suit well and additional solutions are required. The following paragraphs provide some details regarding each one of the available implementations, and all the relevant data is provided in Table 3.2. An example of a channel sounder implementation for the mmWave spectrum can also be seen in Figure 3.19.

FREQUENCY MODULATED CONTINUOUS WAVE SOUNDERS:

A sounder that uses multiple frequency tones in the 28 GHz ISM band is presented

Table 3.2: Existing channel sounding solutions in the mmWave spectrum

Ref.	Technique	Freq. (GHz)	BW (GHz)	Antenna
[51]	Freq. Mod. CW	27.85	0.4	Patch
[52]	Freq. Mod. CW	60	0.4	Horn, 2x2 MIMO
[53]	PN	73.5	1	Horn
[54]	PN	83.5	2	Horn, 16 elements
[55]	PN	28	0.5	Horn
[56]	PN	60	0.5	Biconical horn
[57]	VNA	60	2	Horn, omni
[58]	VNA	69 - 74	5	Horn, biconical
[59]	OFDM	60	0.8	Horn
[60]	802.11 ad	60	2.16	Horn

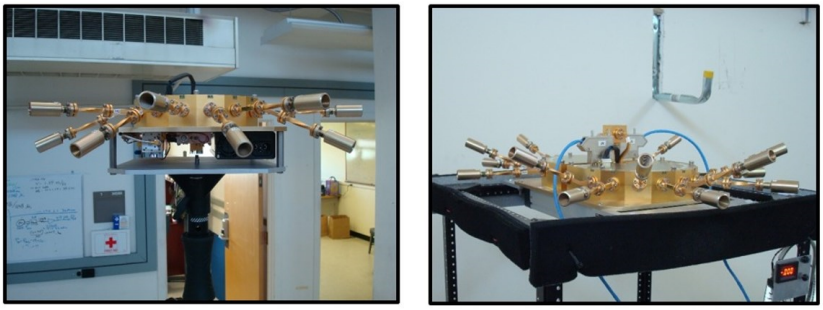

Figure 3.19: mmWave channel sounder presented in [54] (image taken from [61])

in [51]. This sounder generates a baseband signal composed of N different tones distributed over a bandwidth of 400 MHz, and uses an equipment known as band converter to carry the signal up in frequency. This conversion is done in two steps, going through an Intermediate Frequency (IF) where the signal is amplified and filtered, and ending up in the mmWave spectrum by mixing the IF signal with a 27.85 GHz carrier. Electrically steerable patch antenna arrays of 8x2 elements are used for the air interface, which allow to manipulate the boresight of the antennas in 5º steps and provide a total gain of 19.5 dBi. The reverse process is applied in the receiver side. Here, the same patch antenna array is used to capture the signal, which is down-converted to the baseband in two steps as well. The received baseband signal is the sampled at a rate of 1.25 Gsps and stored for processing.

In [52], a frequency modulated continuous wave sounder is presented. This equipment generates a sounding signal that can go up to 1 GHz in baseband and is modulated through three IF stages: 2.2-2.9 GHz, 4.4-5.9 GHz and 14.5-16.1 GHz, which can be useful for multiband sounding. The highest generated frequency is attached to an additional mixer that converts the signal to the 58/64 GHz band, and two copies of this element are used in both transmission and reception to acquire a 2x2 Multiple-Input Multiple-Output (MIMO) channel response. These mixers are attached to horn antennas that provide a gain of 20.7 dBi each. In reception, the received signal that is acquired with each antenna is down-converted and stored using a two channel Analog to Digital Converter (ADC) that operates at a rate of 400 MHz.

PN SOUNDERS:

A channel sounder that uses the sliding correlator technique is presented in [53] for the 73 GHz frequency band. This sounder uses a PN sequence of $2^{11} - 1 = 2047$ elements to generate the baseband signal, which is sampled at a rate of 500 Msps. The signal is up-converter in two steps, passing through an IF step at 5-6 GHz and ending up in the 73 GHz mmWave band. Horn antennas are used for the air interface, where

a total gain of 20 dBi per antenna is provided. In reception, the acquired signal is correlated with the original sequence sampled at a rate of 499.9375 Msps, achieving a time dilation that provides 8000 samples per sequence. A rubidium standard clock is used to synchronize all the clocks in both ends.

An additional sounder that uses a PN sequence is presented in [54]. This implementation uses a sequence of 2047 elements as well, and the generated signal is up-converted in two steps and transmitted in the 83.5 GHz frequency band. The transmitter front-end is composed of a waveguide where a horn antenna or an omnidirectional one can be attached for calibration and measurement purposes. In reception, a total of 16 horn antennas are used to access the air interface, which are selected one by one to achieve an electrically steerable beam. Two complete PN sequences are captured from each antenna, from where the CIR is retrieved. Both ends are synchronized with a rubidium reference clock.

Another sliding correlator sounder can be found in [55]. Here, a PN sequence of 4095 elements is generated at a rate of 500 Msps in the transmitter side, which is modulated with a carrier frequency of 28 GHz. Two horn antennas are used to perform the communication over the air. The one on the transmitter has a Half Power Beam Width (HPBW) of 60º and provides a gain of 9.9 dBi whereas the receiver one covers a narrower HPBW of 10º and offers 24.4 dBi of gain. Regarding the receiver side, the acquired sequence is correlated with the pattern sampled at a rate of 499.96 Msps, which equals to a time dilation where 12.5E3 samples are obtained in total for a single sequence.

At last, [56] presents another PN sequence based solution. This implementation generates two independent sequences of $2^{14}-1 = 16383$ elements sampled at a rate of 500 Msps, which are fed to the In-phase (I) and Quadrature (Q) elements of a complex baseband signal generated at a rate of 1 Gsps. This signal is then up-converted in two steps, passing through an IF stage at 7 GHz and ending up in the 60 GHz mmWave spectrum. Biconical horn antennas are used for the air interface, as they provide an omnidirectional radiation pattern in the azimuth plane. In reception, 20 complete sequences of the I and Q elements are sampled and stored after performing the down-conversion. These samples are taken at a rate of 1 Gsps, and all the sequences are averaged in order to reduce the noise power.

FREQUENCY DOMAIN SOUNDERS:

A frequency domain channel sounder can be found in [57]. This implementation differs slightly from the traditional model, as it uses an external signal generator in order to produce a sounding signal that overcomes the power limitation of the VNA. The signal is generated and split in two: one end is connected to the VNA and the

other goes to a horn antenna used for the air interface. The other port of the VNA is attached to another antenna, from where the received signal is captured. The system is configured to acquire 401 points in the 59-61 GHz frequency range, and two different techniques are employed as well to obtain the spatial information of the propagation, which are using a rotating directional antenna or a uniform virtual array.

The work presented in [58] shows another frequency domain channel sounder. Here, a VNA is used to generate a signal that covers the 3-8 GHz frequency range. This signal is later up-converted to the 69-74 GHz spectrum with an external equipment, and the resulting signal is transmitted to the air with a horn antenna that provides a gain of 20 dBi. The transmitter front-end is rotated in order to obtain directional CIRs, whereas the receiver side uses a biconical antenna that has an omnidirectional pattern in the azimuth. The receiver side captures and down-converts the signal from the air interface, and the resultant is forwarded to the other port of the VNA. An external reference clock generator ensures that the VNA and band converters are synchronized.

OTHER SOUNDERS:

A channel sounder that uses an Orthogonal Frequency-Division Multiplexing (OFDM) symbol for sounding is presented in [59]. This sounder is composed of a Field Programmable Gate Array (FPGA) that controls a high speed ADC/Digital to Analog Converter (DAC) pair capable of operating at a rate of 800 Msps. The DAC generates the sounding signal, which is a 64-point OFDM symbol that has a total duration of 160 ns. This signal is sent to an up-converter which outputs it in the 60 GHz spectrum, and a horn antenna with a gain of 20 dBi makes the connection with the air interface. The same antenna is used in reception, and both ends are mounted over rotating stands that set the directions of departure and arrival. The receptor is equipped with a down-converter as well, which brings the signal back to baseband and sends it to the ADC for the acquisition.

A COTS equipment is used as a channel sounder in [60]. Concretely, the Talon AD7200 router [62] is employed as an IEEE 802.11ad traffic source from where the propagation metrics are obtained. Two different demodulation methods are used to achieve this goal. The first alternative uses another Talon AD7200 router that has access to the Medium Access Control (MAC) layer traffic. This router operates in receiver mode, and metrics as Signal-to-Noise Ratio (SNR), Received Signal Strength Indicator (RSSI) or beamforming patterns are retrieved as packets arrive from the other end. The second method uses a down-converter and an oscilloscope to capture the baseband signal. This signal is demodulated later, from where Physical (PHY) layer metrics as the CIR, SNR and similar are obtained as well.

3.2.3 Channel measurement campaigns in the mmWave spectrum

This section provides details regarding some measurement campaigns that can be found in the literature. These measurements are carried with channel sounders or ray-tracing software and have the aim of acquiring some propagation characteristics of electromagnetic waves as PL, Power Delay Profile (PDP), DS and Azimuth Spread (AS)/Elevation Spread (ES) in Tx or Rx. A graphical representation of the PL estimation is displayed in Figure 3.20 as an example. As the main goal of this work is to analyse the mmWave band over indoor industrial networks, this analysis has been limited to works that present related scenarios. These have been divided in two categories: generic environments such as laboratory, office or living room on one hand an industrial ones on the other. Tables 3.3 and 3.4 provide detailed information of all the works that have been observed, and more information about them can be found in the next next sections.

Indoor generic scenarios

The indoor generic scenarios are detailed in Table 3.3. These can be divided in the following categories: office, university, meeting room and other.

OFFICE MEASUREMENTS:

Table 3.3: Indoor generic channel measurement campaigns in the mmWave spectrum

Ref.	Freq. (GHz)	Environment	Metrics
[57]	60	Office	DS, AS, ES
[55]	28	Hall + office	DS, AS(Rx), cluster num.
[63]	28, 73	Office	PL, DS
[64]	28	Office	PL, DS, AS
[65]	54, 70	Computer foyer, office, factory, corridor	PL, DS, AS(Rx)
[66]	26	Office	PL, DS, coherent BW
[67]	58.5	Hall	Cluster num, pow, delay, path
[68]	28	Library	PL, DS, AS
[69]	28	Classrooms 1/2, office, hall	Power decay, DS, AS
[70]	41	Corridor	DS, AS(Rx), multipath
[71]	130-140	Meeting room	Power decay, DS, AS(Rx)
[72]	60	Hall, meeting room	PL
[73]	45	Living room	PL
[74]	28, 140	Mall	PL, DS, AS(Rx)
[75]	26, 28, 38	Train intra-wagon (2 scenarios)	PL, DS

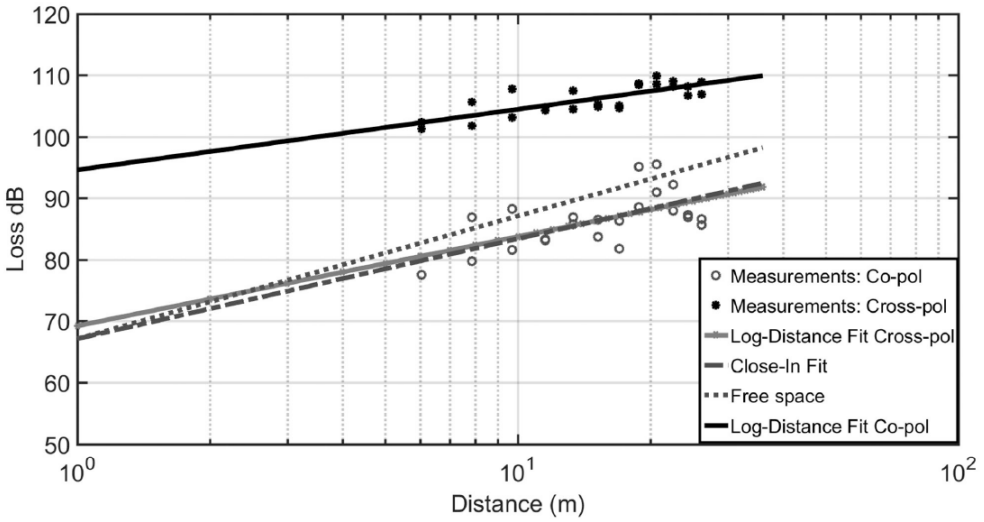

Figure 3.20: Example of PL estimation [65]

A 7.2 x 7.2 m^2 office room is measured with a frequency domain sounder in [57]. The environment has furniture as chairs, desks and a table that have computers and screens on top, and the walls contain several windows and a whiteboard. 12 Tx positions are measured in total for a single Rx location, and the sounder is configured to acquire 401 points per position, which are spanned across 2 GHz and centered at 60 GHz. PDP, DS and AS/ES in Tx are retrieved from the measurements and an analysis of their distributions is provided as well. At last, a parameter fitting is performed to the S-V model, and the results of this process are available to be used in simulated environments.

An environment composed of a corridor and office cubicles is measured in [55] using a sliding correlator channel sounder that operates in the 28 GHz mmWave spectrum and has a total bandwidth of 500 MHz. The corridor presents metallic walls whereas the office cubicles are separated by cardboard walls. The Tx end is positioned at the entrance of the corridor for all the measurements, and three Rx locations are tested in total: one LoS and two NLoS. The work estimates the Angle of Arrival (AoA) via the Space-Alternating Generalized Expectation-Maximization (SAGE) algorithm [76], and groups all the multipath components that are close in direction and time in clusters. Some metrics as their quantity, PL, DS and dispersion in AoA are extracted as well.

Measurements from an additional office environment can be found in [63] for the 27 and 73 GHz frequency bands. The selected positions are distributed along an entire floor of a building with a total dimension of 35 x 65.5 m^2. This floor includes several rooms, corridors, office cubicles and the typical furniture that can be expected

in this kind of scenario. Five Tx and 33 Rx locations are defined here, from where 48 different combinations are measured in total. The PL, as well as the DS are computed for all the measured positions and statistical inference is applied to them in order to obtain the coefficients that define the expected dispersion. The PL is fitted to the CI, FI and ABG models, which were previously introduced in Section 3.1.3.

A generic office room is measured in [64]. Here, a sliding correlator sounder that is centered at 28 GHz and uses a bandwidth of 600 MHz is employed to measure omnidirectional CIRs in 70 different positions (30 LoS and 40 NLoS). The obtained data is processed to compute metrics as the PL (which is fitted to the CI and FI models), DS and the angular dispersion, estimated with the SAGE algorithm.

Several indoor environments that include corridor and office scenarios are measured in [65] in the 54 and 70 GHz frequency bands. A frequency modulated CW sounder that uses a 2x2 MIMO configuration with horn antennas is employed to perform the measurements, which are taken from 37 different Rx locations using four fixed Tx positions. Data processing is performed to acquire some propagation metrics as the PL (fitted to the CI and FI models), DS and AS.

At last, more measurements can be found in [66] within a 9.7 x 6.7 m^2 office. This environment is composed of several materials: concrete for floor and ceiling and wood/plasterboard/glass for the walls. The interior contains typical office materials as chairs, desks, computers and similar. A frequency domain channel sounder is used for the measurements, which is centered at 26 GHz and has a span of 2 GHz, divided in 1091 points. 14 measurements are provided in total, from which 10 belong to a LoS Tx and 4 for a NLoS one. The obtained results are processed to extract the PL (fitted to CI/FI models), DS and coherent bandwidth metrics.

UNIVERSITY MEASUREMENTS:

A university entrance hall is characterized in [67]. Here, a double directional channel sounder equipped with a 2x2 MIMO antenna configuration is employed to capture signals at the 58.5 GHz mmWave spectrum with a total bandwidth of 400 MHz. The Tx is set to a fixed point and 22 Rx positions (18 LoS and 4 NLoS) are measured in total. The acquired CIRs are employed to obtain metrics related to the clustering behaviour of multipath components. These include the number of clusters, their types, arrival rates, power decay and Rician-K factors.

Electromagnetic signal propagation is characterized in [68] inside a university library. This environment has concrete ground and walls, and contains furniture as chairs, tables and whiteboards of different materials, as well as computers and screens on top of tables during the measurements. The channel sounder uses PN as the sounding signal, which is transmitted at the 28 GHz spectrum and has a total

bandwidth of 2 GHz. Five Tx positions and 19 Rx ones are used for the measurements, from where double-directional CIRs are obtained. This data is used to obtain PL (fitted to the CI and FI models) and DS metrics.

Two classrooms, an office and a hall are characterized in [69]. This work performs measurements in these scenarios considering different distances and furniture densities, which can vary from a fully equipped classroom to an empty room. A frequency domain channel sounder is employed in this work, which provides 750 points along a 2 GHz span that is centered at 28 GHz. The obtained data is used to compute the PL exponent, DS, AS and LoS/NLoS power ratio metrics.

At last, a university corridor is characterized in [70]. This corridor has a total width of 1.6 m and a corner separates it in two section, the first one has a length of 44.1 m and the second 32.4 m. The selected channel sounder uses a Golay sequence [77] correlation to obtain the CIRs and operates with a bandwidth of 1.25 GHz at the 41 GHz mmWave spectrum. Three different measurement sets are carried out to obtain PL, multipath (DS) and angular power spread metrics. The PL metrics are fitted to the CI and FI models, and ray-tracing simulations are also performed to validate the results. Statistical fitting of parameters as the DS is provided as well.

MEETING ROOM MEASUREMENTS:

Terahertz signal propagation within a meeting room is measured in [71]. In this work, a 10.1 x 7.9 m^2 room that contains some chairs, a table and two TVs in the walls is characterized with a frequency domain sounder. The sounder operates in the 130 - 143 GHz frequency range and retrieves 1301 points per acquisition. Ten Rx positions are measured in total for a single Tx location, and the obtained data is processed to compute the Rician-K, DS and AS metrics.

A hallway and a meeting room are characterized in [72]. Here, a frequency channel sounder is used to measure 401 points over a 2 GHz span at the 60 GHz spectrum. The Rx end is set in a single position during the hallway measurements, and the Tx is set at 12 different locations. On the other hand, 10 receiver locations are defined in the meeting room and two experiments are carried out: one where the transmitter is located at the center and another one on an edge of the room. The obtained data is used to characterize the PL of the environments, and a fitting to the FI model is provided as well.

OTHER SCENARIO MEASUREMENTS:

Measurements of a living room can be found in [73]. The dimensions of the room are 9 x 4.4 m^2, and a total of 12 Rx positions are defined within it. The transmitter is placed in a corner of the room during all the measurements. A channel sounder that operates at the 45 GHz frequency band obtains all the CIRs, which are later processed

to obtain PL metrics and perform a fitting to the FI model.

A four-story mall is characterized in [74]. The building has an approximate dimension of 120 x 70 m^2, from where 18 measurements are performed. A frequency domain channel sounder is used to achieve this, which has a bandwidth of 4 GHz and two frequency bands for the air interface: 28 and 140 GHz. The acquired directional CIRs are used to compute some propagation metrics as the PL (fitted to the FI model), DS and AS, as well as the number of multipath clusters in each location.

At last, some railway environment measurements are provided in [75]. This campaign uses a frequency domain channel sounder that performs the measurements over the 25-40 GHz frequency range and provides 8192 points per measurement. Two scenarios are tested in this work: one where the transmitter is located at the center of the wagon and another where it is paired to the seats. The Rx end is static during all the measurements, and 14 Tx positions are measured in total between both tests. Obtained data is processed as well in order to obtain PL (which is fitted to the FI model) and DS metrics.

Indoor industrial scenarios

The indoor industrial environments are described in Table 3.4. Details regarding each individual work are provided next.

Table 3.4: Indoor industrial channel measurement campaigns in the mmWave spectrum

Ref.	Freq. (GHz)	Environment	Metrics
[60]	60	Pipe room, hall, p.accelerator ring, tunnels	Cluster num, pow, delay, path
[78]	3.7, 28	Machining workshop	PL, DS, AS(Rx)
[79]	28	Sake factory, subway station	PL, PDP, AS(Rx)
[80]	24	Workshop, production hall, storage hall	PL
[81]	28	Machine hall	PL, DS, AS(Rx)
[82]	28	Warehouse	PL
[83]	28	Machine room	PL, DS, AS(Tx), ES(Tx)
[84]	28	Optic fiber cable laboratory	PL, DS, AS(Rx)
[85]	142	Manufacturing lab hub	PL, DS, AS(Tx,Rx)
[86]	6.75, 33.75, 60.75	Production hall	PL, DS, AS(Tx), ES(Tx)
[87]	3.5, 38.5, 39.5	Textile factory	PL, DS, RICIAN-K
[88]	28	Digital fabrication	PL, DS, AS(Rx)
[89]	28, 60	Light and heavy industries	PL, DS, AS(Tx,Rx), RICIAN-K

Several industrial scenarios as a mechanical room, experimental hall, particle accelerator ring and two maintenance tunnels are tested in [60]. Here, the Talon AD7200 router [62] is employed as a 60 GHz signal source and the channel information is obtained using two criteria: by capturing IEEE 802.11ad packets and by down-converting and storing the signal. This information is used to estimate the throughput the 802.11ad standard can offer in each scenario, and a fitting to a custom multipath propagation model is provided as well. This model groups the multipath components in clusters, and the computed metrics are the number of clusters, number of components per cluster, DS and expected power of each cluster and component.

Propagation inside a high-precision machining workshop is characterized in [78] for the 3.7 and 28 GHz frequency bands. A sliding correlator channel sounder that provides a bandwidth of 2 GHz in two frequency bands is used for the measurements. 76 positions are measured in total (38 LoS and 37 NLoS), and propagation metrics as PL (fitted to the FI and ABG models), DS and Tx/Rx AS are extracted from them as well.

A sake factory and a subway station are measured in [79]. The factory environment is composed of a 38.5 x 31.2 m^2 floor that contains a corridor and two rooms, and four Tx and five Rx positions are measured here in total. The station presents a total length of 152 meters, from where the Tx and Rx are placed at 3 different locations each. A frequency modulated continuous wave sounder that operates in the 28 GHz spectrum is used to obtain the data from both environments. Some post-processing is done to the data as well, from where metrics as the PL (fitted to the FI model), DS and receiver AS are extracted.

The PL from three different scenarios is characterized in [80] in the 24 GHz spectrum. These environments are a university workshop, a production hall and a storage room. The channel sounder employed during the measurements is composed of a signal generator, frequency band converters, omnidirectional antennas and a spectrum analyser. 26 tones that are spaced 10 MHz apart are generated for the sounding, adding up to a total bandwidth of 250 MHz, and several distances and antenna altitudes are tested in all the sites with this, considering both LoS and NLoS cases. The obtained data is used to perform a PL estimation, which is fitted to the CI and FI models, and these parameters are also compared to the results of other works.

Measurements from a circle-shaped machine hall are presented in [81]. A sliding correlator channel sounder with a bandwidth of 2 GHz and centered at 28 GHz is employed to obtain the CIRs. Four configurations are measured in total: two different heights and swapping the Tx/Rx ends, as one of them is static during all the process. 40 positions are measured per configuration, which means that 160 measurements are

provided in total. This data is processed to obtain metrics as PL (fitted to the CI and FI models), signal blockage, DS and AS, both in departure and arrival.

Signal propagation inside a smart warehouse filled with automatic guided vehicles is characterized in [82] for the 28 GHz spectrum. A frequency domain channel sounder is employed to carry out these measurements, which captures 1001 points in a span of 1 GHz. Three scenarios are measured in total: one LoS and two NLoS, the latter being provoked by placing one and two containers. The results are processed to obtain PDP and PL related metrics.

Measurements are carried in [83] inside a machine room with a size of 35 x 16 m^2. A frequency domain sounder that operates in the 28 GHz spectrum is employed for the measurements. This sounder uses monopole antennas in both ends, and takes 801 points spanned across 4 GHz in each acquisition. Three conditions are measured in total: none, partial and total obstruction of the LoS component. The data is processed as well, from where metrics as PL (fitted to the FI model), DS and AS (estimated with the SAGE algorithm) are obtained.

Propagation through an optic fiber laboratory is characterized in [84] in the 28 GHz frequency band. This measurement campaign uses a PN channel sounder that provides a bandwidth of 2.4 GHz, and two tests are carried out in total. The first one measures the PL at various distances (57 positions) and the second tests several antenna orientations (12 positions). The obtained results are employed to estimate the PL (fitted to the CI and FI models), DS and AS in reception.

In [85], sub-Terahertz measurements are carried out in a corridor that separates various machining laboratories and conference rooms. CIRs are acquired via a sliding correlator channel sounder that offers a total bandwidth of 500 MHz in baseband and is centered at 142 GHz, and horn antennas are used as well to obtain double-directional responses. Thirteen measurements are carried out in total, from where 11 are LoS and 2 NLoS. These are processed later to obtain PL (fitted to the CI model), DS and departure/arrival AS, considering the directional and omnidirectional CIRs separately, as well as co/cross polarization of antennas.

Multi-band measurements can be found in [86] for a production hall. This room has a total size of 171 x 74 m^2, and four sections can be divided: three production lines and a storage area. Measurements are performed over these sections with a 15-bit PN sounder that has a total bandwidth of 6.75 GHz and is capable of acquiring the directional CIR of the 6.75, 30 and 60 GHz frequency bands simultaneously. The data is processed to estimate the PL (fitted to the ABG model), DS and departure AS/ES inside the environment.

An additional multi-band measurement campaign can be found in [87]. Here,

propagation within a 120 x 40 m^2 textile factory is characterized using a frequency domain channel sounder. The channel sounder is configured to acquire 501 frequency points per measurement, which cover a span of 1 GHz and are centered at 3.5, 38.5 and 39.5 GHz. A total amount of 15 positions are characterized, distributed along two corridors surrounded by looms. The obtained data is used to perform PL (fitted to the ABG model), DS and Ricean-K value estimations.

A digital fabrication facility is characterized in [88] in the 28 GHz spectrum. Here, a 13 x 13 m^2 manufacturing zone is characterized by measuring 13 scenarios that combine the none, partial and total obstruction of the LoS component. The results are processed to obtain some propagation metrics as the PL (fitted to the CI model), DS and AS of arrival. The effects of co/cross polarization of antennas is also observed in these metrics.

At last, a ray-tracing based propagation characterization is carried out in [89] for simulated light/heavy industrial sites. This work uses a simulation tool known as Wireless InSite [90] to model the propagation of signals that operate in the 28 and 60 GHz mmWave spectrum using the SBR technique. The outputted results include the PL, LoS probability, Rician-K factor, DS and AS/ES, both in departure and arrival.

3.3 Network simulation

When a communication system is designed, it is necessary to complete a performance analysis to verify that its behavior is in accordance with the expected one. There are three main ways to carry out such task, which are a mathematical analysis, a simulation based approach and performing measurements of the system.

Mathematical analysis and measurements present some drawbacks on their own. The first solution can only provide a limited insight of the system, whereas the second one is very demanding as a Hardware (HW) implementation, which is difficult at early stages, and on-site measurements are required for a proper evaluation. At last, the simulations provide a good trade-off between the cost and fidelity of the analysis, which is why it is the selected method in most cases.

Nowadays there are several tools that provide a framework to test network implementations in the literature, additional information can be found in [91]. Simulations can be carried out following several methods as Monte Carlo (MC) [92], event tracing and similar, but most of these tools follow the discrete-event simulation method. This kind of simulation breaks all the interactions of a network in events that occur at specific times and jumps from one event to the following one, computing the output of each and scheduling new events when it is required. A graphical representation of

this concept can be seen in Figure 3.21.

The low complexity of the implementation and low simulation time are some of the main advantages of discrete-event simulators. As stated before, several tools that implement this concept can be found in the literature, the most extended ones being Network Simulator (NS)-2/3 and OMNeT++. Both tools are detailed in the following sections.

3.3.1 NS-2/3 simulator

Two versions of the NS simulator exist nowadays: NS-2 and NS-3. Even if the third version is based on the second one, both are incompatible, which is why they are treated as separate tools in the literature.

NS-2 gained a lot of popularity when it was active and became the standard simulation tool for most industrial and academic works. However, this tool had some issues as using a mixture of Tcl/C++ languages for programming, which was not as straightforward as using a single language, or lacking a standardized structure for the contributions. The later derived in additional challenges as an increasing complexity in the maintenance of the code or incompatibility issues between different contributions, which were the main reasons to abandon this version and develop the third one.

The NS-3 standard used some pieces from NS-2 as well as the GTNetS [93] and YANS [94] simulators for its development. The main goals of this version were to overcome the limitations found in the previous one as well as to increase the realism of the simulations. For this reason, a strict coding structure was defined to ease the maintenance, and all the programming was done in C++ with support for Python scripting. An interface based architecture was also defined, which is similar to the structure that Linux computers use.

Each NS-3 simulation is written as a different C++ program. Here, parameters as the participating devices, the network topology, propagation medium, protocol stack and applications are defined, among others. The following list shows the objects that can be defined in these programs:

- **Node:** A piece of equipment that participates in the network (laptop, router, etc.).

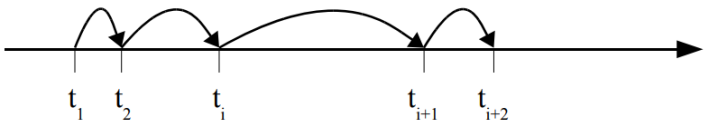

Figure 3.21: Discrete-event simulation concept [91]

- **Network device:** The equivalent of a network card, provides connection to the node (ethernet card, bluetooth, etc.).
- **Protocol stack:** Communication protocol used in the network. This may include several layers as MAC (Ethernet, 802.11), network (Internet Protocol (IP)) or trasport (Transmission Control Protocol (TCP)/User Datagram Protocol (UDP)).
- **Application:** Applications act as source and sink of payload data.
- **Channel:** The channel represents the medium information is exchanged over (point-to-point, broadcast, wireless, etc.).
- **Others:** Additional parameters that describe the network can be defined as well (mobility, energy consumption, etc.).

Predefined code blocks or custom designs can be selected to construct a network, and the configuration can be refined by defining the attributes of the blocks. Objects provide *traces* as well to retrieve the output information of interest when a simulation is launched, or traffic monitoring can be included to output standard Packet Capture (PCAP) files.

3.3.2 OMNET++ simulator

Contrary to what is believed, the OMNeT++ simulation tool is not a proper network simulator. Instead, it provides some tools that can be used to write simulations and it is always used together with a framework as INET. OMNeT++ follows a modular code structure written in C++ and its objective is to provide a simulator as generic as possible in order to implement and reuse custom modules with ease. This tool is also equipped with a custom *Eclipse*-based Integrated Development Environment (IDE) that contains a graphic interface that can be used to configure a simulation. In this regard, a domain specific language denominated NED is also presented to store the definition, parameters and connections of the different modules that participate in a network. As an example, Figure 3.22 shows the graphical/NED definitions for a simulated network.

In order to maintain a structure as generic and reusable as possible, OMNeT++ organizes the components that participate in a network in modules. There are two types of them: simple modules to represent individual blocks as applications (data source, sink), protocols (IP, TCP, UDP), data structures (routing tables) and similar and compound modules, which are formed by grouping several simple modules. An example for a compound module would be a laptop or a router, which would

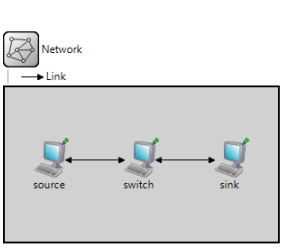


```
network Network
{
    types:
        channel Link extends ned.DatarateChannel {
            delay = 1ms;
        }
    submodules:
        source: SourceHost {
            @display("p=50,80");
        }
        switch: SwitchNode {
            @display("p=150,80");
        }
        sink: SinkHost {
            @display("p=250,80");
        }
    connections:
        source.out --> Link --> switch.in1;
        switch.out1 --> Link --> source.in;
        switch.out2 --> Link --> sink.in;
        sink.out --> Link --> switch.in2;
}
```

Figure 3.22: Graphical representation and NED code of an OMNeT++ network

include several modules to accomplish the different tasks the device needs to carry out. Modules are configured with *attributes* that are assigned in the simulation setup or during runtime. Information between modules is exchanged through *gates* that can be input, output or bidirectional type. Different modules form *connections* between them, using the gates to exchange *messages*. These can contain information as packet data, configuration or any other kind. Additionally, it is possible to configure a connection to have certain delay and error rate, simulating the behaviour of real channels.

As stated in the beginning of the section, OMNeT++ works with a framework that provides all the functions to represent protocols, communication media or other aspects as energy consumption. Nowadays several frameworks have been implemented in this environment, the following list provides some details of each:

- **INET:** Provides models for various internet protocols as TCP, UDP, IPv4/6, point-to-point, 802.11 and so on.
- **INETMANET:** Extends INET by providing mobile ad-hoc support with several routing protocols.
- **OverSim:** Another extension of the INET framework where structured and unstructured peer-to-peer communication protocols are represented.
- **MiXiM:** Includes models for wireless communications and mobility. Different protocols, mobility types and channel effects (fading, blockage, etc.) are provided, as well as a graphical interface for these environments.
- **Castalia:** Castalia defines models for wireless low-power scenarios as embedded systems, wireless sensor networks or personal area networks. Realistic node behaviour and channel access mechanisms are provided to test all kind of implementations over these scenarios.

3.4 IEEE 802.11ad standard

The IEEE 802.11ad standard is introduced in this section, as it is the communication protocol that has been used in this thesis for testing. The main motivation behind this decision is that 802.11ad is a fully developed protocol stack that operates in the mmWave spectrum and has available products as HW and simulation tools, along documentation. Other protocols as 5G NR or the newer 802.11ay version have been considered as well, but the scarce access to equipment and documentation for 5G, along the lack of implementation over real equipment for the 802.11ay standard were the reasons to discard them in the end.

This section provides details regarding the main structure of the 802.11ad standard, and some literature works that aim to characterize its achievable performance are reviewed as well.

3.4.1 Structure of IEEE 802.11ad

As for the structure of the protocol, the 802.11 working group defines a new channel access scheme oriented to Directional multi-Gigabit (DMG) communications. This covers the PHY and MAC layers of the OSI model, and the access scheme is composed of a periodically repeating structure known as a beacon. Each beacon lasts one or several Time Units (TUs), which are time blocks of 1024 μs. The duration of a beacon, which is known as the BI, is split in several fragments that control tasks as device aggregation, beamforming and channel access for data exchange. A detailed description of this mechanism and the implication of the MAC/PHY layers in it are provided next.

MAC layer

In relation to the MAC layer, 802.11ad presents a completely new architecture to cope with DMG communications [95]. The new structure can be found in Figure 3.23, and as it can be seen, several access sources are defined depending on the use case.

As described previously, all these access sources are multiplexed in time slots that form part of a periodically repeating structure known as a BI. This structure is shown in Figure 3.24, where a BI is divided into two main sections: Beacon Header Interval (BHI) and Data Transfer Interval (DTI). Details regarding both fields are provided next.

The header field covers the discovery, association, resource allocation and beamforming functions. 802.11ad uses directional communications through one of the predefined directions, which are known as *sectors*. The level of refinement of the

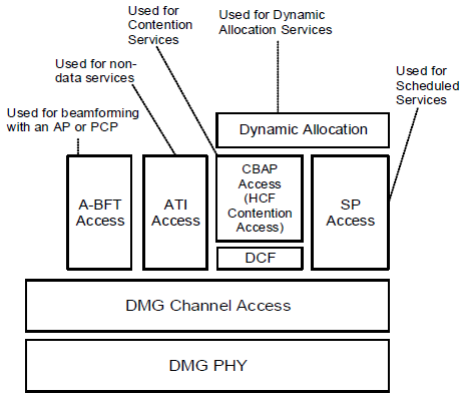

Figure 3.23: IEEE 802.11 DMG MAC layer packet structure [95]

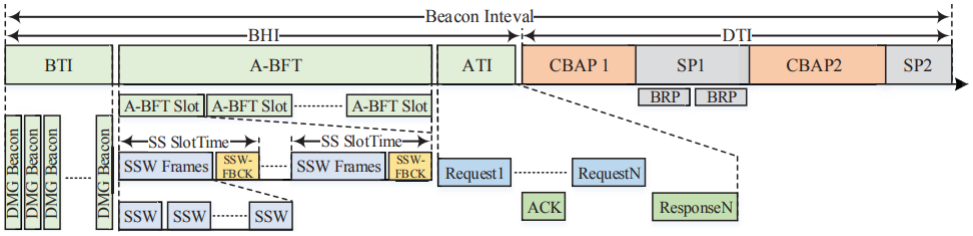

Figure 3.24: IEEE 802.11 MAC layer BI structure [96]

beams is defined by the number of available sectors, which can be of 2 (0º and 180º), 4 (0º, 90º, 180º and 270º), 8 and so on. The BHI has the responsibility of finding the best sector combination of each Tx-Rx pair among the other functions, and three sub-fields are defined to achieve these goals:

- **Beacon Transfer Interval (BTI):** The Access Point (AP) sends one beacon frame per sector during this interval. These messages serve to synchronize the network and provide the essential parameters. Both the length of A-BFT and the presence of the ATI field are defined in this frame.

- **Association Beamforming Training (A-BFT):** This period is employed to adjust the beamforming between AP and one or several Stations (STAs), depending on the assigned length. A mechanism based on sector sweep and feedback is used to achieve this.

- **Announcement Transmission Interval (ATI):** The AP and STAs can use this optional interval to exchange messages related to management, authentication, Acknowledge (ACK), polling, Request To Send (RTS)/Clear To Send (CTS) frames and similar functions.

Data messages are exchanged between the AP and STAs during the DTI. Two modes are defined by 802.11ad to perform this operation: one where the participants compete for channel access and another one where a previous allocation grants exclusive channel access to a STA. The segments of the DTI are specified in a beacon frame during the BHI using the AllocationType and Association ID (AID) parameters. The two access types are detailed below:

- **Service Period (SP):** When SP is active, a packet can only be transmitted from a previously specified STA. No other communications are allowed during this interval.
- **Contention Based Access Period (CBAP):** In the CBAP mode, nodes adopt the Distributed Coordination Function (DCF) configuration, where channel is accessed following a Carrier Sensing Multiple Access with Collision Avoidance (CSMA/CA) scheme. STAs must ensure that no communication exceeds the duration of the DTI.

As for the structure of individual messages, all versions of IEEE 802.11 share the same MAC Protocol Data Unit (MPDU) format. Four main fields are required to generate any kind of frame: Frame control, Duration/ID, Address 1 and Frame Check Sequence (FCS). The remaining parts of the frame, along the contents of the body are completely optional and may vary depending on the MPDU type. All the fields that can be detailed in a generic MAC header are shown in Figure 3.25.

The previously introduced DMG beacons form part of the extension type described in the generic MPDU. In order to select it, MAC headers must contain type and subtype fields to "11" and "0000", respectively. The MAC frame body content can be seen in Figure 3.26, where beacon related data is stored.

Each beacon is formed by four headers with a fixed length a variable body. This last part contains configuration fields that are divided in 40 different categories, being

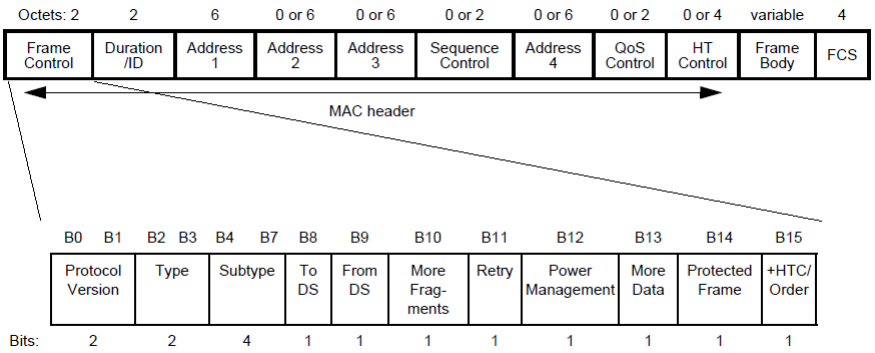

Figure 3.25: Generic IEEE 802.11 MAC frame structure [95]

	Frame Control	Duration	BSSID	Frame Body	FCS
Octets:	2	2	6	Variable	4

Figure 3.26: IEEE 802.11 DMG beacon frame structure [95]

most of them optional. Two parameters contain relevant data regarding the DTI: Order 5 (DMG parameters) and order 8 (Extended Schedule). The fifth category selects a data transmission mode while the eighth one defines the access mode and active STAs in the case of SP during the DTI segments.

The rest of message types as beamforming related ones or data follow the same MPDU scheme as the one described above. Depending on the established configuration, nodes will use different access mechanisms and data will be transmitted following any structure supported by the MAC layer.

PHY layer

Four operation modes are presented in the 802.11ad PHY layer [95, 97]. These are known as Control, Single Carrier (SC), OFDM and SC - low power. All modes are composed of the same fields, which can be seen in Figure 3.27.

All the modes share a common preamble, which is formed by the Short Training Field (STF) and Channel Estimation (CE) fields. Golay sequences (also known as complementary sequences) are employed to generate their corresponding signals. The main goal of these fields is to provide a reference to the receiver from where the channel/time and Automatic Gain Control (AGC) can be adjusted. As shown in Figure 3.27, its structure varies depending on the mode. The control mode presents a significantly larger STF compared to the rest, where 5120 symbols are used instead of

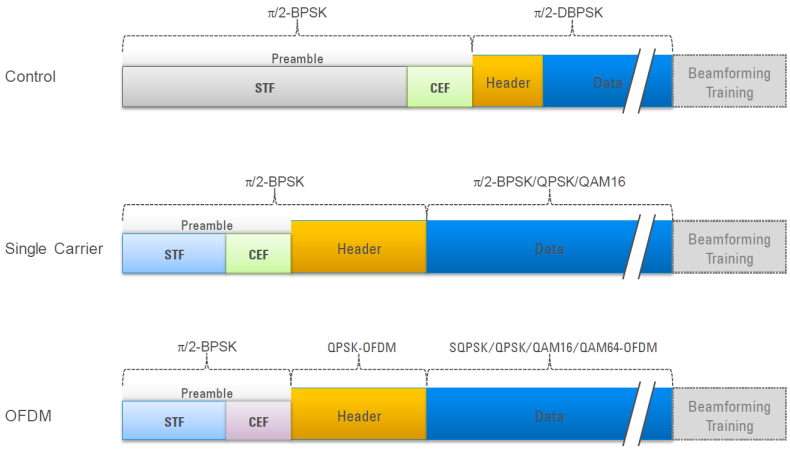

Figure 3.27: IEEE 802.11 Physical layer packet structure [97]

2176. On the other hand, the CE has a total length of 1152 symbols for all the modes. The only variant here is how the Golay sequences are concatenated, as SC and OFDM use two different combinations.

In reception, these packets are correlated with the reference Golay sequences in order to determine which modulation needs to be used in the remaining part of the message. Golay sequences have a perfect auto-correlation property, which means that the correlation outputs a non-zero value only when a perfect match is present between both sequences. An example of the correlation process is provided in Figure 3.28.

After passing through the training fields, the PHY mode is obtained and the synchronization is completed. At this point, the content of the message is decoded starting from the header, which has parameters that vary between different modes. All the headers share the Modulation and Coding Scheme (MCS) field, which specifies parameters as the constellation and code rate the data is modulated with. The standard defines a total of 32 different MCSs, but only the first five (indices 0 to 4) are mandatory. All the configurations are detailed in Table 3.5.

Some messages append the additional AGC and beamforming training segments after the data slot. The PHY modes the data is encoded with, as well as their corresponding components are detailed in the next sections.

PHY LAYER ENCODING AND MODULATION: CONTROL

The Control layer (MCS 0) defines a unique coding scheme for both header and data messages. It is oriented to robust transmissions, where a strong redundancy is applied to the transmitted information. Headers do not specify MCS, as only one configuration is allowed. The modulation process, which is identical for the data part, can be seen in Figure 3.29, and details of the individual components can be found in [95].

PHY LAYER ENCODING AND MODULATION: SC / SC - LOW POWER

Figure 3.28: Correlation of Golay Sequences in receiver [97]

Table 3.5: MCS configurations [95]

	MCS	Modulation	NCBPS	Code rate	Data rate (Mbps)
Control	0	DBPSK	-	1/2	27.5
Single Carrier	1	π/2-BPSK	1	1/2	385
	2	π/2-BPSK	1	1/2	770
	3	π/2-BPSK	1	5/8	962.5
	4	π/2-BPSK	1	3/4	1155
	5	π/2-BPSK	1	13/16	1251.25
	6	π/2-QPSK	2	1/2	1540
	7	π/2-QPSK	2	5/8	1925
	8	π/2-QPSK	2	3/4	2310
	9	π/2-QPSK	2	13/16	2502.5
	10	π/2-16QAM	4	1/2	3080
	11	π/2-16QAM	4	5/8	3850
	12	π/2-16QAM	4	3/4	4620
OFDM	13	SQPSK	336	1/2	693
	14	SQPSK	336	5/8	866.25
	15	QPSK	672	1/2	1386
	16	QPSK	672	5/8	1732.5
	17	QPSK	672	3/4	2079
	18	16-QAM	1344	1/2	2772
	19	16-QAM	1344	5/8	3465
	20	16-QAM	1344	3/4	4158
	21	16-QAM	1344	5/8	4504.5
	22	64-QAM	2016	5/8	5197.5
	23	64-QAM	2016	3/4	6237
	24	64-QAM	2016	13/16	6756.75
SC - Low Power	25	π/2-BPSK	392	13/28	626
	26	π/2-BPSK	392	13/21	834
	27	π/2-BPSK	392	52/63	1112
	28	π/2-QPSK	392	13/28	1251
	29	π/2-QPSK	392	13/21	1668
	30	π/2-QPSK	392	52/63	2224
	31	π/2-QPSK	392	13/14	2503

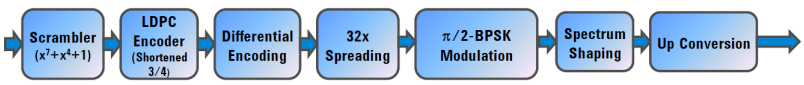

Figure 3.29: Modulation and coding process for Control frames [97]

Both variants of the SC modulation share the same preamble and header. These modes offer a trade-off between robustness and throughput, and additional mechanisms as frame aggregation are included in the header configuration. Both variants can be differentiated with the MCS value, and the modulation scheme followed by the standard SC (MCS 1 to 12) can be found in Figure 3.30.

The modulation steps are identical in the low power alternative (MCS 25 to 31). The codification part, on the other hand, is completely different. Instead of the combination between Scrambler and Low-Density Parity Check (LDPC), this alternative uses a mix of Reed-Solomon (RS), block coding and interleaving.

Two different formats are defined for the header and data. The header uses a robust RS code of RS(24,8) along a (16,8) block code. Data octets are encoded with a RS scheme of RS(224,208), and several modes of the block coding are used for the following step, depending on the selected MCS. Encoded data provided by both sources is interleaved by an uniform interleaver, and a grouping process is applied to the result. This process is used to aggregate guard intervals between data symbols via Golay sequences as it can be seen in Figure 3.31.

Once the blocks are created, the modulation of the data is performed in an identical manner to the standard SC, and the transmitted signal is finally generated. A detailed description of all the process and individual elements can be found in [95].

PHY LAYER ENCODING AND MODULATION: OFDM

OFDM messages have a fixed configuration for headers and a MCS dependant configuration for data. Headers serve several purposes as transmitting the active MCS, managing tone-pairing/beamforming processes or handling protocols as data aggregation. The modulation and coding process is the same for all the modes, the only variation is the behaviour of individual blocks as it can be seen in Figure 3.32.

Headers follow a static configuration where 64 bit blocks of a packet are initially

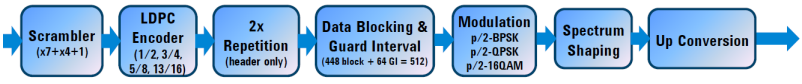

Figure 3.30: Modulation and coding process for SC frames [97]

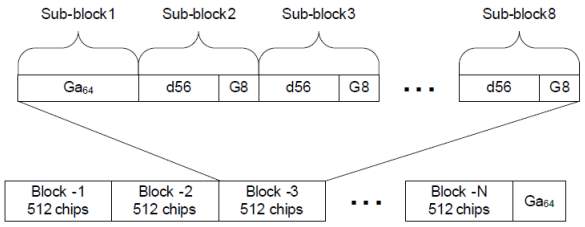

Figure 3.31: Data grouping process for SC - low power frames [95]

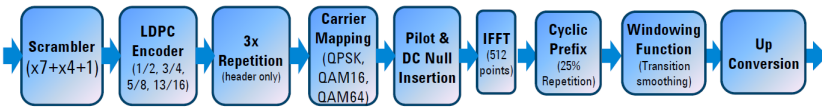

Figure 3.32: Modulation and coding process for OFDM frames [97]

passed through a scrambler. After that, zero padding is used to obtain 504 bit sequences, which are later encoded with a 3/4 LDPC code. Three repetitions of the sequence are concatenated then. This is modulated with QPSK, and the result is introduced in an OFDM symbol. Pilot and zero carriers are aggregated to the data, and the Inverse Fast Fourier Transform (IFFT) operation is performed to generate the complex baseband signal. Data is modulated in a similar manner, but in this case the LDPC has a variable configuration and the encoded sequence is not repeated. Additional information about this PHY mode can be found in [95].

AGC AND BEAMFORMING TRAINING IN PHY LAYER

AGC and beamforming training fields are aggregated to BRP packets. The structure of this kind of packet is presented in Figure 3.33.

The AGC field has the same structure regardless of the MCS. However, there is a slight difference depending on the transmission mode, as the SC and OFDM use the Golay sequence Ga_{64} to generate the signal and the Control uses the Gb_{64} one. At last, if the training length is of N, this sub-field lasts four times N.

On the other hand, the TRN sub-field is composed of N repetitions of a training unit, each one having a CE field as a preamble and four repetitions of a Golay sequence. The Golay sequence is $[Ga_{128}\ -Gb_{128}\ Ga_{128}\ Gb_{128}\ Ga_{128}]$ in all the transmission modes. There are two types of packets of this kind: Receive Training (TRN-R) and Transmit Training (TRN-T). The main difference between them is that the transmission mode uses individual training sub-sequences to have a different Antenna Weight Vector (AWV) whereas the receiver mode employs the previous configuration.

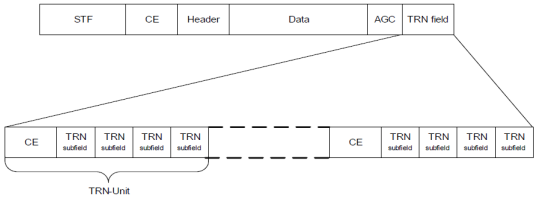

Figure 3.33: BRP packet structure [95]

3.4.2 Characterization of IEEE 802.11ad performance

In this section, the main performance characterization efforts of the 802.11ad standard that can be found in the literature are reviewed. A summary of all the relevant data from the analysed works is provided in Table 3.6, where parameters as the employed equipment (which can be real HW or a simulator), the type of generated traffic, scenario (which includes location and topology) and results can be found. Details regarding individual works are provided next.

In [98], 802.11ad radio modules that are produced by Panasonic [106] are used to test MCSs 1-9 in a typical office environment. A single link is tested in this work, where information is exchanged between the AP and a client in the form of TCP/UDP packets. Two separate conditions are evaluated: with and without interference. The provided results show that multi-Gigabit throughput is achievable for both TCP/UDP traffic if the appropriate MCS and packet size are selected. On the other hand, the paper shows that interference can cause a significant degradation in the throughput of the system and concludes that this effect should be mitigated or minimized.

Two 802.11ad compliant laptops are used in [99] to test the throughput of a link in several sites inside a university building. Both TCP/UDP traffic are generated during the testing, and the results prove that a Gigabit throughput can be achieved in all the cases if the orientation is correct and LoS is present.

Three COTS equipment models (two routers and a laptop) that work with the 802.11ad standard are evaluated in [100]. In this work, three setups are deployed in a typical office environment, each having an AP and one or several clients. The throughput and Round-Trip Time (RTT) of TCP traffic is measured with several network densities, and additional mechanisms as frame aggregation or spatial reuse are analysed as well.

A 802.11ad compliant smartphone is tested in [101]. Here, the selected MCS and achievable throughput are observed for various distances inside a lobby and a corridor, and scenarios with mobility are considered as well. The provided results show that the phone can operate effectively in this frequency band but that the beam pattern selector does not work optimally in the presence of mobility.

In [102], the TGad channel model [107] is used to evaluate the performance of a simulated 802.11ad link in a conference room. Several configurations that include the SC and OFDM modes are used in order to determine the effective throughput of the link for each case, which is given in the form of Bit Error Rate (BER) and Packet Error Rate (PER). Results show that the system is not well suited to operate with multipath fading and emphasises in the need of the LoS component and directivity.

A custom model is implemented in Matlab in [103] to test the behaviour of CBAP

Table 3.6: Comparison of existing 802.11ad characterization works

Ref.	Equipment		Traffic	Scenario	Results
[98]	HW - Panasonic IEEE 802.11ad radio		Iperf3 - TCP/UDP	Office - Link	Throughput, interference
[99]	HW	- Wilocity wil6210 802.11 - Dell Wireless Dock D5000	Iperf3 - TCP/UDP	University building - Link	Throughput
[100]	HW	- TP-Link Talon AD7200 - Netgear Nighthawk X10 - Acer Travelmate P446-M	Iperf2 - TCP/UDP	Office - Network	Throughput, delay (RTT)
[101]	HW - Asus ROG Phone		Iperf3 - TCP	Lobby, corridor - Link	Throughput, range, mobility
[102]	Simulator - TGad		4000 Byte packets	Conference room - Link	BER, PER
[103]	Simulator - Matlab Custom		7500 Byte packets	Not specified - Network	Throughput, arrival rate, service time
[104]	Simulator - OPNET		Video stream	Living, conference - Network	Throughput, delay
[105]	Simulator - Matlab 802.11ad PHY		1000 Byte packets	Conference room - Link	Throughput vs (SNR, Distance, BER)

and SP channel access methods defined in 802.11ad. A Markov chain is used to compute the backoff counter in CBAP traffic, and a stochastic model is proposed to represent SP scheduling delay as well. Simulations test various configurations where CBAP and SP occupy variable portions of the data section and the amount of stations, as well as the BER is changed. The obtained results show the effective throughput and packet arrival rate in each scenario.

The OPNET simulation environment is employed in [104] with a custom 802.11ad model. Three different scenarios are tested under this simulator, from where the throughput and delay metrics are obtained for small networks.

At last, the conference room model presented in [107] is used in [105] in order to evaluate the performance of various configurations that the 802.11ad PHY layer offers. Here, the throughput, as well as the error rate in the form of BER/PER are analysed for a single data link. The results show the error rate under several SNRs, and the achievable throughput under different MCSs, SNRs and distances.

Chapter 4

Channel characterization in the mmWave spectrum

The first step to assess the viability of mmWave frequency band communications for industrial applications is to learn about the behaviour of these signals in factory environments. As detailed in Section 3.2, this process is carried out with experimental measurements that are performed with a device known as a channel sounder. The use of mmWaves is relatively new in the communication systems sector (the first protocols were proposed in 2009) and for this reason the available HW is very limited. The mmWave channel sounders that can be found in the literature were presented in Section 3.2, but none of them are commercially available or easily replicable. For this reason, part of this thesis is dedicated to the elaboration of a channel sounder and performing measurements with it, which is the process described in this chapter.

This chapter is divided as follows: The first half details the elaboration of a custom cost-effective channel sounder that is composed of commercial elements and is designed to analyze the propagation of mmWave signals within industrial facilities. Details regarding the selected equipment, design and validation are provided in this section. The second half details a measurement campaign carried out in real industrial sites, where the sounder is employed to characterize the propagation. The selected sites, sounder configuration, extracted data and computed propagation metrics are detailed in this section. At last, the main conclusions drawn from these works are presented.

4.1 Custom channel sounder for the 60 GHz frequency band

This section describes the process behind the elaboration of the channel sounder that has been used during several development stages of this thesis. The starting

point is described first, where the possible ways to reach the mmWave spectrum are analysed and one of such options is selected. Next, the inclusion of the sounding signal generation and acquisition devices is discussed. Four major stages of the sounder are presented here, where the design limitations and proposed solutions are shown. The channel sounding signal is discussed after presenting the final HW configuration, and the calibration process carried out to suppress the undesired effects that the HW introduces to the CIRs is detailed as well. At last, the validation process of the equipment is presented.

The design and validation process of the sounder was published and presented in the IEEE International Workshop on Factory Communication Systems (WFCS) 2022 conference as the *A Cost-Effective Directional Millimeter-Wave Channel Sounder for 60 GHz Industrial Wireless Communications* article [34].

4.1.1 Reaching the mmWave spectrum

The main difficulty of mmWave signal propagation characterization is to find suitable equipment that operates in these frequencies, as there are not many solutions that cover this band. Two types of HW are used in the literature to achieve this: frequency band converters and VNAs.

When sounding is carried out in the time domain, signals are typically generated in baseband frequencies (up to few GHz), and a device known as band converter carries it up to or down from the mmWave spectrum. Generally this process is completed in two steps, passing through an IF stage where additional processing is carried out. On the other hand, VNAs make this process internally and outputs frequency tones within the range of interest.

The N5252A E-Band VNA (60 - 90 GHz) from Keysight [108] was already available in the laboratory at the start of this thesis. However, this equipment presents several challenges to operate as a channel sounder. The main application for this device is the characterization of electromagnetic signal propagation through different materials, and for this reason it has very few room to separate and rotate the front-ends. Apart from this, a strict synchronization is carried out between the front-ends, and a semi-rigid coaxial cable of six meters is employed to achieve this. The calibration of this kind of device is time consuming as well, as several configurations need to be tested in the waveguides from both front-ends and each configuration requires to screw/unscrew an equipment piece to them. Even if VNAs provide a superior resolution, it was concluded that using the available equipment as a channel sounder is not feasible and a search for another alternative began after.

Some literature works use the PEM-009 kit from Pasternack [109], which is composed of two band-converters, tripods and all the necessary power and data cables. This equipment can perform the conversion between baseband and any carrier frequency in the 57.24 - 64.8 GHz range in steps of 540 MHz, which is ideal to measure the frequencies that the IEEE 802.11ad standard operates over. A graphic interface is provided by the vendor as well, where parameters as the center frequency, bandwidth or attenuation values can be configured. At last, the system clock allows three configurations to synchronize both ends: individual internal clocks, shared clock (one is the generator and the other uses that signal) and external source for both ends. As this device is more portable and cost-effective than a VNA, it was selected as the starting point of the channel sounder.

Antenna selection was carried out next, as the band-converters have a WR-15 waveguide connector as their air interface. In this work, Lens Horn Antennas (LHAs) from Anteral [110] have been selected for both ends because they can achieve a gain of 30.3 dBi by using a total aperture that provides approximately 6° of HPBW. The lens of the antennas are of special interest for this use case as well, since they provide plane-wave (i.e. far field area) responses in proximity and FA communications are carried out in a relatively short distance. Apart from this, using antennas with high gain and directivity is crucial in the mmWave spectrum, because, as described in Section 3.1 with the Friis transmission equation (3.2), the PL increases when frequency arises. These properties are essential to measure the weakest multipath components, since the additional PL can make them arrive with very low energy.

As both antennas are highly directive, it is necessary to consider the directions of departure and arrival of the front-ends, because the CIRs will vary significantly depending on the orientation. If all the azimuth angle combinations need to be tested with a reasonable spatial resolution, for example the antenna's HPBW of 6°, a total of $(360/6)^2 = 3600$ orientations would be required, which makes the manual steering option unfeasible. For this reason, motorized positioners were installed below the front-ends, concretely the 8MR174-11 model from Standa [111], as they were already available in the laboratory. This motor can be used for both manual and automatic positioning, and the latter can be implemented in any scripting tool with a precision of 0.1°.

A limitation of this design is that positioning the antennas in all the orientations require up to several hours, which makes the channel sounder unfeasible to capture channels that have rapid variations in time. As it was described in Section 3.2.2, this is common between channel sounders in the mmWave spectrum, and the only models can measure time variant channels include special mechanisms as antenna

arrays or dipoles for the acquisition. In any case, since the main interest of this work is to analyse the received power and characteristics of multipath components, this limitation was ignored, at least for a first version.

The band converters, antennas and motors form the Stage 0 of the sounder, as they make mmWave signal propagation possible. However, it is still incomplete because both signal generation and acquisition are missing. The next section covers this topic, and the implementation carried out so far is shown in Figure 4.1.

4.1.2 Generation and acquisition of data

The addition of signal generation and acquisition devices to the initial stage of the sounder is discussed in this section. Equipment that was available at the laboratory was tested first and four designs were developed in total, overcoming the limitations that were detected in each stage. The following sub-sections provide a detailed description of each stage, as well as the main issues found after their implementation.

Stage 1

The first stage of the channel sounder is presented in Figure 4.2. Here, two pieces of equipment are incorporated to the stage 0, which are the MS2840A signal analyser and generator from Anritsu [112] and the MDO4104B oscilloscope from Tektronix [113].

This system uses the signal generation functionality of the MS2840A device, which can accept any given waveform file as input. Originally the acquisition was intended to be performed in the same device as well because both generation and acquisition can be performed simultaneously. However, both processes run independently and it is not possible to synchronize them or share a trigger signal, which is why this idea was discarded. Apart from this, two major drawbacks were present in this HW: an insufficient bandwidth (waveform files are generated at a sample rate of 160 MHz

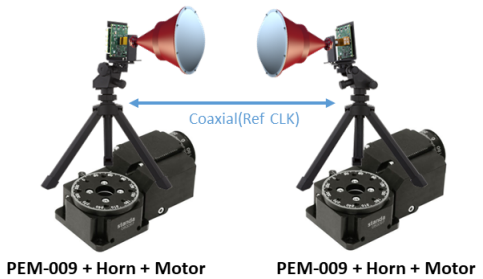

Figure 4.1: Stage 0 of the channel sounder

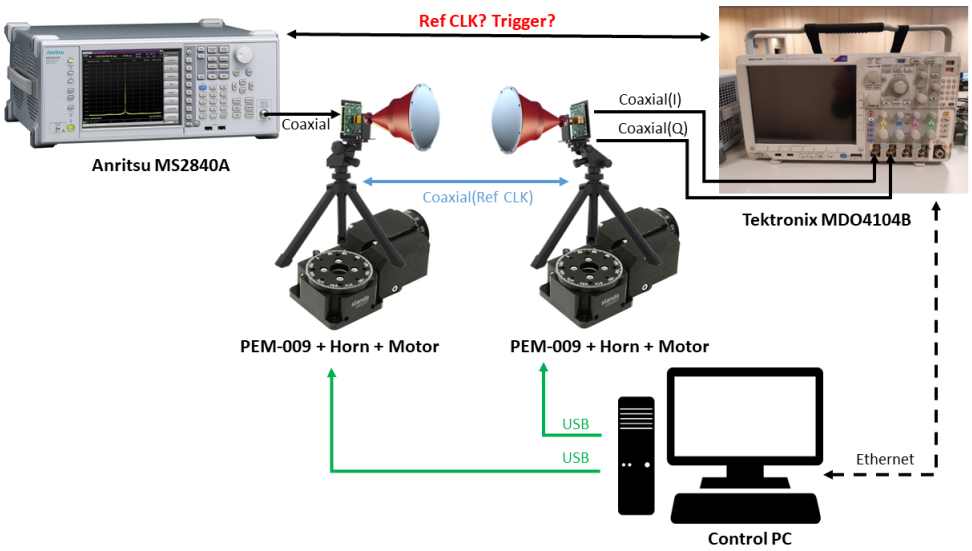

Figure 4.2: Stage 1 of the channel sounder

and modulated to an IF) and a single output, which is not enough to feed the I/Q input lanes of the band-converter. Limitations aside, it was concluded that the signal generator could be used to test at least an initial stage.

As for the reception, the MDO4104B oscilloscope was selected because it can acquire both I/Q lanes simultaneously. However, this device has only two coaxial connectors to share configuration signals: a 10 MHz reference clock input and a auxiliary connector that has a configurable output. The MS2840A signal generator has a 10 MHz reference clock input as well, which means that it is not possible to pass both trigger and reference signals between the devices since the auxiliary output of the oscilloscope needs to generate the reference signal. A possible solution could be to add a third device that generates the reference for all the systems, but as this adds additional complexity to the system and the MS2840A has limitations on its own, it was concluded that using another generator was a better approach. This is the point that separates the first and second stages.

Stage 2

As stated previously, the second stage replaces the transmitter end with a device that is capable of generating a reference clock signal for synchronization. This device is the AMIQ I/Q modulation generator from Rohde & Schwarz [114], Figure 4.3 shows the updated layout.

This stage of the sounder operates as follows. First of all, a control Personal Computer (PC) configures the transmitter device using the serial interface. A trigger

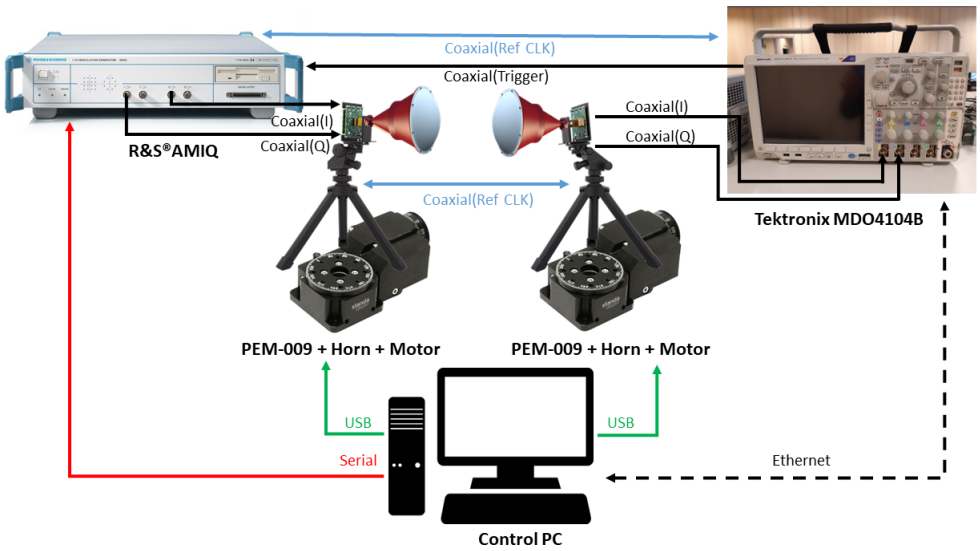

Figure 4.3: Stage 2 of the channel sounder

based transmission is enabled in this step, and the waveform of the signal is provided as well. After configuring the transmitter, the receiver is activated from the PC via Ethernet. When an acquisition is triggered, the oscilloscope forwards the trigger towards the transmitter and commences capturing the signal, achieving the synchronization between both ends.

Even if this stage overcomes most of the limitations that were present in the previous one, the available bandwidth is still an issue. This equipment has a sampling rate of 100 MHz, which is not enough to cover all the desired range (as a reference, 802.11ad uses channels with a total bandwidth of 2.16 GHz). There was no time domain signal generator in the laboratory that could cover such a wide spectrum, and for this reason the implementation of a frequency domain sounder was tested next.

Stage 3

A VNA was included in this stage of the channel sounder in order to significantly increase the bandwidth of the captures. Concretely, the ZVRE model from Rohde & Schwarz has been selected, which is capable of measuring the S-Parameters of any frequency in the 9 kHz - 4 GHz range. The scheme of this stage is displayed in Figure 4.4.

This device was configured to acquire 801 points over a 540 MHz span, and both the trigger and data acquisition processes were carried out with a control PC through a serial interface. Some tests showed that the CIRs that can be obtained with this equipment were in accordance with the environment, as the LoS power and delay

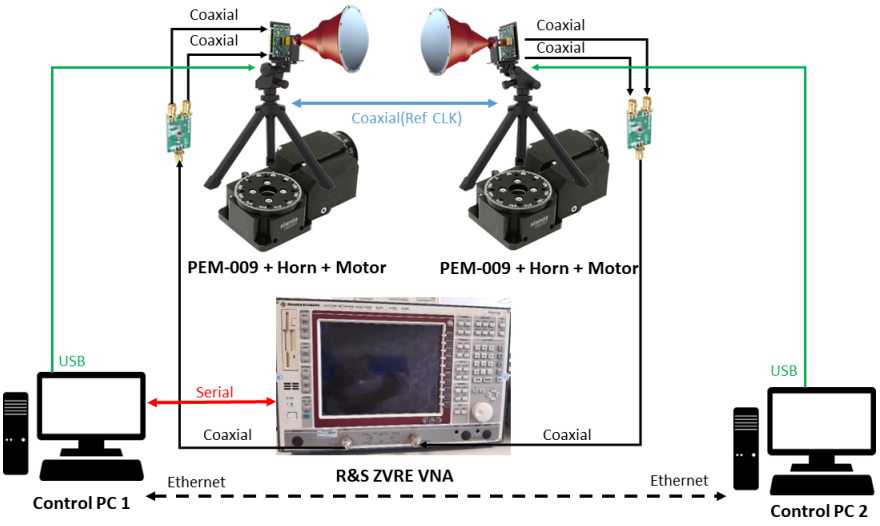

Figure 4.4: Stage 3 of the channel sounder

coincided with the expected values, which were computed with the Friis transmission equation (3.2) and the distance. However, there was still an issue related to the mirror frequencies, which is depicted in Figure 4.5.

The mirror frequency issue appears because the channel sounder operates with real signals and its spectrum is symmetric. When a frequency f is up-converted to the mmWave spectrum, two components will appear: $f_c + f$ and $f_c - f$. The problem is that if a notch attenuates one of the two components (cases 1 and 2 from Figure 4.5) the reception will not be able to know which one is it because the result will be the same after the down-conversion.

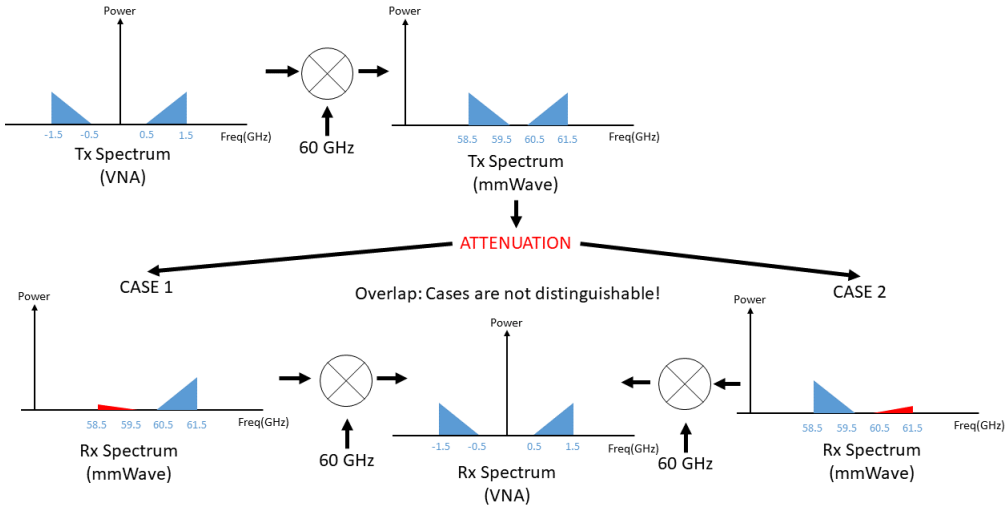

Figure 4.5: Mirror frequency issue in sounder with VNA

Two possible solutions were tested in order to overcome this issue:

- **Using different carrier frequencies:** Instead of using 60 GHz for up and down conversion, two different carriers were applied in this solution. For example, if the 59-60 GHz range needs to be characterized with a VNA that has 1 GHz of span, this signal is up-converted at 60 GHz and down-converted at 59 GHz, where the mirror frequencies would be at 1-2 GHz after the down-conversion. It can also be down-converted at 61 GHz to know the response of the 60-61 GHz range.
- **Filtering the mirror components:** The mirror frequencies are suppressed before performing the up-conversion to the mmWave spectrum. To do so, the signal is converted to an IF first and a low pass filter is applied, canceling one of the bands.

Both solutions need an IF stage for the implementation, which was reached using a mixer and a signal generator. The main issue related to this was that the signal generator needs to generate the exact tone that is used in the down-conversion for the IF stage. As the band-converters operate with an harmonic of a 308.571 MHz internal clock, the exact carrier frequency was susceptible to change (the voltage, temperature and similar parameters of the board can affect to it) and it was observed that generating an IF with an external device was not viable because it was impossible to match the exact tones. With this results in mind, frequency domain sounding was discarded and the stage 2 of the sounder was considered again since it provided more promising results.

Final stage

The final stage of the sounder uses the time-domain sounding approach, as the frequency-domain alternative was proven to be unsuitable in the previous stage. Here, a more powerful signal generator was purchased to overcome the limitations of stage 2, and some few adjustments were made to the layout as well to incorporate this piece properly. Figure 4.6 shows the complete structure of the final stage.

In this stage, the sounding signal is generated by the ADS-V2EBZ FPGA from Analog Devices [115], which includes functionalities for waveform pattern file management. This FPGA is controlled with a PC via Universal Serial Bus (USB), where parameters as the operation mode can be set and pattern files can be transmitted to the FPGA's internal memory. In order to output this data to a coaxial cable, a dual-channel, high-speed DAC board is attached to the FPGA, concretely the AD9174 evaluation board from Analog Devices [116]. This equipment allows to generate any complex baseband signal sampled at a rate of 2.94912 GHz (a multiplication of an internal

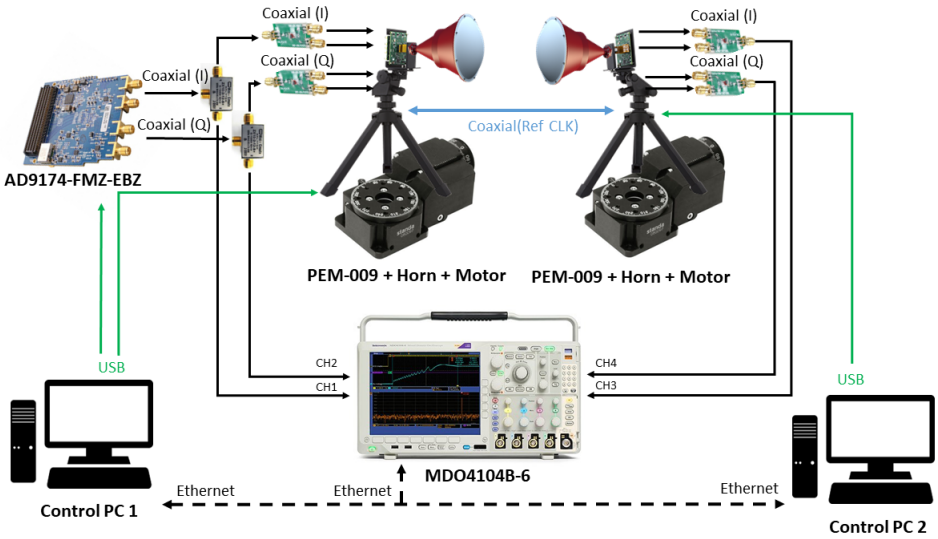

Figure 4.6: Final stage of the channel sounder

clock at 122.88 MHz), which is stored in the memory of the FPGA in the form of two independent waveform files that can have a length of up to 1E9 samples. This signal generator is more than capable to cover the 2.16 GHz bandwidth the 802.11ad standard operates over.

As for the operation, both I/Q signals are generated in this device as two separate signals, and these are forwarded to two locations using splitters: the front-end and the acquisition device. The acquisition device of this stage is the previously introduced MDO4104B-6 from Tektronix [113], but it operates in a different manner. Instead of synchronizing with the transmitter and sharing both reference clock and trigger signals, the oscilloscope is configured to simultaneously capture both transmitted and received complex baseband signals at a rate of 2.5 Gsps. As the signal from both ends is known, the CIR can be obtained by de-convolving them and thus no synchronization is required with the signal generator. The signal generator can continuously output the sounding signal and the acquisition device can make snapshots independently, simplifying the architecture design.

4.1.3 Sounding signal and calibration

The complex baseband signal generation and initial calibration of the sounder are discussed in this section. As described in the final HW setup, a high-speed, dual-channel DAC board is employed for the signal generation, which provides a great flexibility regarding the waveform signal selection.

After analysing several sounding signal alternatives as Zadoff-Chu (ZC) sequences,

OFDM symbols and similar, it was concluded that the chirp signal could be an interesting option since it provides a perfect Peak-to-Average Power Ratio (PAPR) and has an almost constant gain in all the frequency band while maintaining a simple structure for testing and implementation. A chirp signal can be generated as follows:

$$x(n) = exp\left(j2\pi\left(f_{min}n + \frac{f_{max} - f_{min}}{2N}n^2\right)\right), \tag{4.1}$$

where n is the sample index, N represents the total length of the sequence and f_{min} and f_{max} indicate the minimum and maximum frequencies, respectively.

The initial chirp signal was configured to measure the complete 2.16 GHz bandwidth that the 802.11ad standard operates over. However, the results showed that the band converter did not cope well with a spectrum as wide as the provided one because the highest frequencies suffered a considerably greater attenuation. It was concluded that it would be better to measure two contiguous 1.08 GHz frequency bands to avoid this issue, as the band converters can be configured to do this, and a chirp signal that covers the $[-540..540)$ MHz range was defined. The signal generation process showed that this signal suffers some power ripple at the highest frequencies, as shown in Figure 4.7. As it can be seen, this was solved by increasing the total frequency range, where the generator sends a $[-700..700)$ MHz chirp and the acquisition focuses only in the $[-540..540)$ MHz range.

In order to define the total duration of the chirp, a trade-off between SNR and acquisition time was done, since longer chirp signals provide better results but require more time and disk space for storage. The oscilloscope was configured to capture 10k samples at a rate of 2.5Gsps, which equals to a total time window of 4 μs. This

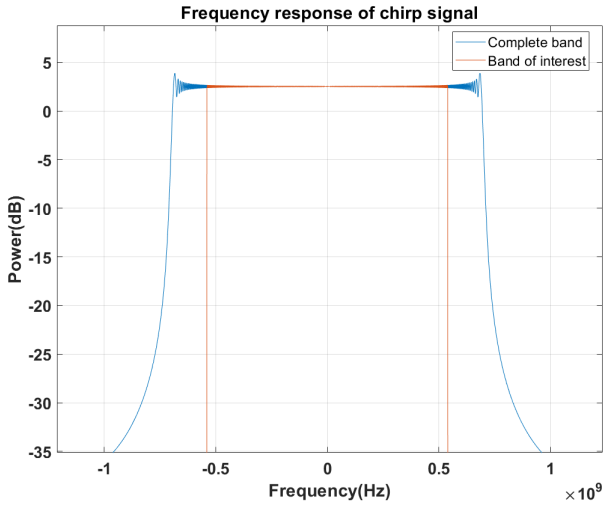

Figure 4.7: Frequency domain response of generated vs measured regions

time window was used for the chirp signal as well, which means that each acquisition contains exactly one chirp sequence.

Four signals are stored in the PC when an acquisition is completed: the real and imaginary baseband signals from the transmitter and receiver. A processing step is applied to this data in order to extract the CIR, which begins by obtaining the difference between both complex signals. This can be carried out in time domain by convolving the received signal with the complex conjugate of the transmitted one (4.2) or in the frequency domain, where the frequency response of the received sequence is divided by the transmitted one (4.3).

$$y(t) = x(t) \circledast h(t) \Leftrightarrow h(t) = x^*(t) \circledast y(t) \tag{4.2}$$

$$Y(f) = X(f)H(f) \Leftrightarrow H(f) = \frac{Y(f)}{X(f)} \tag{4.3}$$

The result of this process contains information about the propagation of the signal through the air interface mixed with the variations introduced by the HW. In order to obtain the true CIR, the effects of the HW must be removed, and to achieve this the response of the HW must be known to compensate it using the same process described in equations (4.2) and (4.3). The response of the HW is achieved by performing a measurement when a WR-15 waveguide is employed to connect both front-ends, as shown in Figure 4.8. When the CIR is measured using this setup, the obtained result contains just the HW effects, which is later used as a calibration source that cancels them from the measurements that are made with the antennas.

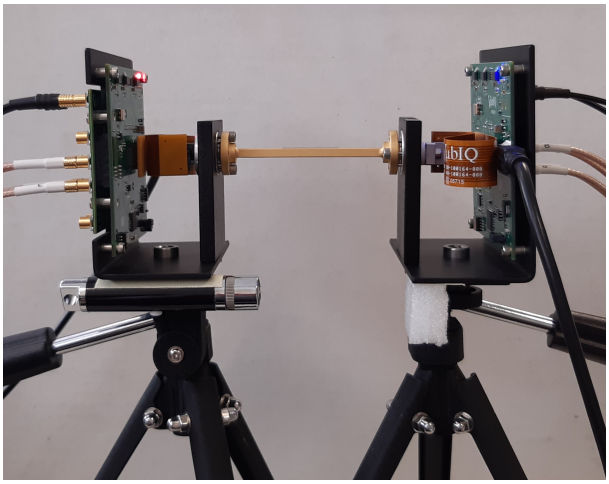

Figure 4.8: Front-ends connected with a WR-15 waveguide

A problem of this compensation technique is that the effects of the waveguide appears as a part of the calibration signal and that the response of the antennas is not considered. Since the waveguide has approximately the same length of the combination of the antennas and, due to the lack of proper instrumentation to characterize it, its response is assumed to be flat in all the band of interest, no compensation is introduced to this component. On the other hand, the antenna vendor provides some information regarding the gain over different frequencies [110], where a difference of less than 0.5 dB can be appreciated for a span of 1 GHz. Since this variations is very low, antenna response was assumed to be flat for the band of interest and this effect was not compensated.

4.1.4 Equipment validation

After ensuring that the channel sounder was assembled and operational, three different tests were carried out to verify that its performance was in accordance with the expected one. The following sections describe the objective and achieved results in each one of them.

Test 1: Comparison with a VNA

As stated at the beginning of the chapter, the N5252A E-Band VNA from Keysight [108] was already available in the laboratory at the beginning of the thesis, which operates in the 60 GHz frequency band as well. Since both devices work in the same frequency band and use identical antennas, it is possible to make measurements with them under the same conditions and compare the results. Two settings are defined in total due to the limitations of the VNA: one where the antennas are separated 0.4 meters in LoS and another NLoS scenario where a reflector is placed at a separation of 3 meters (6 meters of path length in total). The achieved CIRs in both scenarios are displayed in Figure 4.9.

The measurements are carried out using a center frequency at 62.1 GHz and a total bandwidth of 1.08 GHz, which corresponds to a resolution of 0.27 m and 0.925 ns per sample in space and time, respectively. As it can be seen in the results, the VNA offers a better dynamic range compared to the sounder, which is of approximately 65 dB in comparison to 40 dB. Nevertheless, both signals are correlated and their peaks show almost the same gain and delay. In the LoS test, both devices have estimated a delay of 1.8 ns (or a separation of 0.54 m), which is in accordance with the setup. On the other hand, a slight difference is present in the delay of the NLoS scenario. The computed delays are of 19.4 ns (or 5.82 m) and 22.2 ns (or 6.66 m) for the VNA and the sounder, respectively. This corresponds to a difference of 3 samples and it is

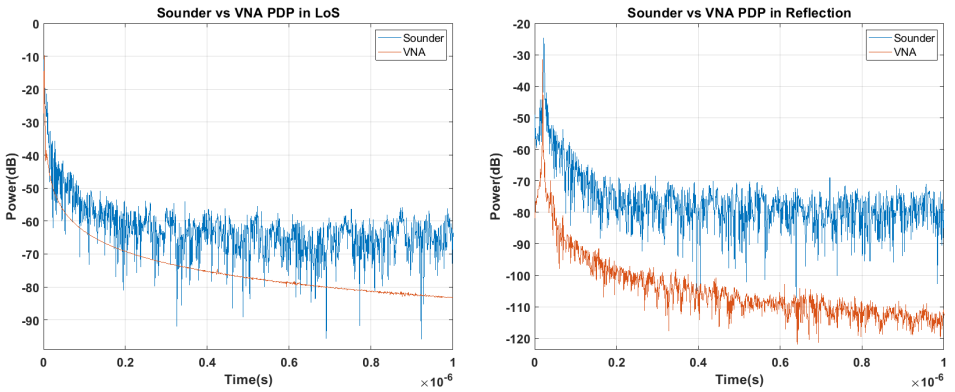

(a) LoS scenario (b) Reflection scenario

Figure 4.9: CIR of sounder and VNA in LoS and reflection scenarios

attributed to the slight differences between tests, since both equipment pieces need to be placed and oriented towards the reflector manually in the same position and the imperfections during the calibration process of the sounder can add variation as well. Even if this slight difference exists and the dynamic range of the sounder is lower in comparison to the one of the VNA, it was concluded that this test was a success because the dynamic range of the sounder is sufficient to measure several multipath components and the shapes of the CIRs are consistent.

Test 2: Power and delay vs distance

The second test aims to prove that the channel sounder is capable of measuring the power and delay properly at various distances. To achieve this, an environment where reflections are negligible has been selected in order to mimic a propagation that has FSPL. This environment is a corridor from the university of Mondragon, which is shown in Figure 4.10. The lack of reflecting surfaces along the highly directive antennas make the CIRs show just the LoS component when both ends are faced at each other. This can be modeled using the Friis transmission equation (3.2) for the power and the physical distance for the delay, where a constant propagation speed of 3E8 m/s can be assumed.

In this experiment, the sounding signal has a total bandwidth of 1.08 GHz and is centered at 59.94 GHz. Various distances are tested, starting form a separation of 1 meter and increasing the separation in 0.5 meter steps until 7.5 meters are reached. The expected values are computed as well for all these distances, and all the results are compared after, as shown in Table 4.1.

The results show a clear consistency between the expected and measured values

Figure 4.10: Power and distance test in corridor

Table 4.1: Estimated and measured powers and distances at various positions

Distance (m)		**Power (dB)**	
Real	**Measured**	**FSPL**	**Measured**
1	1.13	-74.01	-73.3
1.5	1.66	-77.53	-75.75
2	2.1	-80.03	-79.2
2.5	2.7	-81.96	-80.68
3	3.33	-83.55	-84.9
3.5	3.6	-84.89	-84.8
4	4.14	-86.05	-86.2
4.5	4.71	-87.07	-84.22
5	5.27	-87.98	-90.57
5.5	5.55	-88.81	-90.7
6	6.11	-89.57	-88.45
6.5	6.66	-90.26	-90.07
7	7.2	-90.91	-88.81
7.5	7.5	-91.51	-90.96

in all the cases. Regarding the distance, some differences can be seen between the measured and real values, which is mainly attributed to the limited resolution that the sounder can provide with this configuration (each sample equals to a step of 0.27 m). As for the power, the measured values are slightly higher than the estimated ones. Possible causes may be the presence of noise in the measurements, insufficient resolution or imperfections introduced during the calibration process, but since this difference is very slight it was concluded that the sounder provides appropriate measurements.

Test 3: Delay estimation based on orientation and layout

The double-directional aspect of the sounder is evaluated in this validation step. The main idea behind this test is to perform a complete azimuth scan with the sounder in an environment that is rich in reflecting surfaces, because this would generate several multipath components that the sounder should be able to detect. The machining workshop shown in Figure 4.11 was selected for this task, since it contains several metallic elements as the machines, pillars, tool holders and lockers.

The test is configured as follows. An arbitrary separation of 5 meters is defined for the channel sounder in this environment. As for the sounding signal, two contiguous 1.08 GHz frequency bands are measured and processed together in order to duplicate the temporal resolution. At last, the antennas are steered across all the azimuth in 3º steps, generating 14400 CIRs after the frequency band aggregation. A heatmap is generated with the strongest component detected in each path, as shown in Figure 4.12a.

As it can be seen, some directions contain a significantly greater power compared to the rest, which are the ones that contain the multipath elements. Four directions are marked for the validation process, even if there are more: LoS, NLoS1, NLoS2

Figure 4.11: Sounder in machining workshop

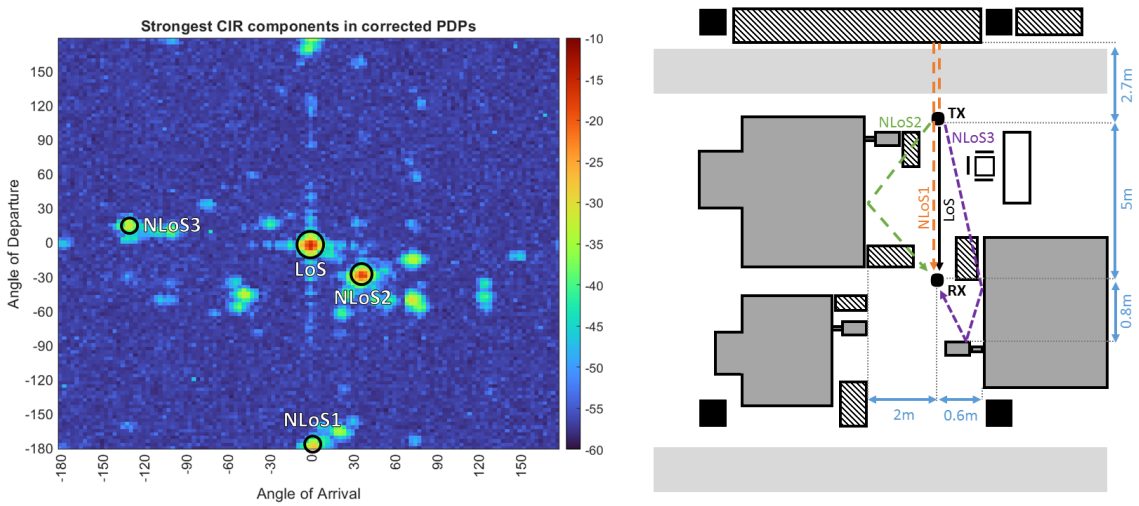

(a) Heatmap of maximum detected powers in workshop

(b) Workshop layout with multipath direction estimations

Figure 4.12: Sounder validation in workshop

and NLoS3. The layout of the workshop is provided in Figure 4.12b as well, and objective of the test is to use just the antenna orientations provided by heatmap and this layout to estimate real propagation paths. As the workshop dimensions are known, the distance of the paths can be computed along the expected delay, and this delay should be the same as the one that can be found in the individual CIRs.

The results from this experiment are summarized in Table 4.2. As it can be seen, the four estimated delays that were computed based on antenna angle combination and the layout of the site coincide almost perfectly with the real ones, which are extracted from the CIRs. This test shows that the sounder is capable of obtaining multipath components coming from multiple directions and that the spatial information is truly correlated to the environment.

Table 4.2: Estimated and measured delays of detected multipath components

Path	**AoD (º)**	**AoA (º)**	**Estimated delay (ns)**	**Measured delay (ns)**
LoS	0	0	16.67	16.66
NLoS1	-180	3	34.66	37
NLoS2	-30	36	21.33	19.44
NLoS3	15	-129	22.33	21.29

4.2 Industrial site measurements and characterization

Some industrial sites that were measured and characterized with the channel sounder developed in this thesis are discussed next. Here, the configuration of the channel sounder is detailed first for the measurement campaign. The two sites that have been characterized are introduced after, where details regarding the layouts, objects and materials that can be found in each site are provided. The post-processing step is explained then, where metrics as the amount of multipath components, power, delay and directions of departure/arrival are computed from each measured position. At last, the PL, DS and AS coefficients that are extracted from the processed data are shown and compared to other results that have been reported in similar literature works.

The measurement campaign described in this section was carried out as a collaborative work between MU and HiG, which took place between September-December, 2022. These measurements in particular were submitted to the NIST's NextG Channel Model alliance public repository [36] under the *HiG Workshop* and *Ovako steel company pit oven* names. The obtained results were presented in the WFCS 2023 conference as well, as the *60 GHz mmWave Signal Propagation Characterization in Workshop and Steel Industry* paper [35].

4.2.1 Equipment configuration

The configuration that the channel sounder employed during this measurement campaign is shown in Table 4.3.

As it can be seen, the chirp signal and antennas are identical to the ones described in the previous section. Apart from this, a trade-off between bandwidth, resolution in azimuth and acquisition time has been carried out to establish the rest of parameters.

Ideally, the channel sounder would capture a total bandwidth of 2.16 GHz in the mmWave spectrum with a resolution of 3º in azimuth. This configuration allows to measure the complete bandwidth of a channel the 802.11ad/ay standards operate over with a spatial resolution that equals to half the HPBW of the antennas, which can be helpful to cope with the losses due to antenna misalignment. However, 28800 CIRs must be acquired in each position to obtain this resolution, which correspond to two complete azimuth scans that cover the 59.94 and 61.02 GHz center frequencies in the mmWave spectrum. Even if the channel sounder can measure this, the acquisition time is of approximately 12 hours per position, which is not compatible with the limited availability of the industrial facilities.

In order to solve this issue, a more limited configuration was employed during these measurements, which consists of just one center frequency in the mmWave

Table 4.3: Sounder configuration for industrial measurements

Category	Parameter	Value
Sounding signal	Signal type	Chirp
	Freq. Range (MHz)	[-540 to 540]
	Duration (ns)	4000
Band conversion	Center freq (GHz)	59.94
Antennas	Type	LHA
	Gain (dBi)	30
	HPBW (º)	6
Azimuth orient.	Center(LoS) (º)	0
	Step (º)	6
	Range (º)	[-180 to 180]
Acquisition	Sampling rate (Gsps)	2.5
	Number of samples	10000
Results per position	Data type	CIR
	Number of captures	3600
	Total memory (MBytes)	230

spectrum (59.94 GHz) and an azimuth resolution of 6º. With this, the amount of CIRs per position is reduced to 3600 and the acquisition time is of 3 hours instead of 12, which is a more viable duration considering the limited availability of the sites.

4.2.2 Measured industrial sites

The selected sites for the measurements were a workshop from the HiG and a pit oven that belongs to the Ovako steel company [117] at Hofors. These sites are particularly interesting because, on one hand, an additional measurement campaign was already carried out in the HiG workshop for the 24 GHz mmWave spectrum, which can be a good source for a comparison. On the other hand, the pit oven scenario is surrounded by metallic elements as pipes, pillars and stairs, which is an interesting option to measure the effect that heavy multipath can have. The measurements were carried out in static environments during the maintenance period of the ovens, and very little activity was present in both sites when the data was acquired.

HiG workshop

The HiG workshop is a typical university workshop that contains some few units of a wide variety of machines. The Figure 4.13 shows a picture of the site as well as its layout and measured positions.

As it can be seen, this environment contains several industrial equipment pieces as soldering stations, an hydraulic press, a metal cutter, a drilling station and a mill. A

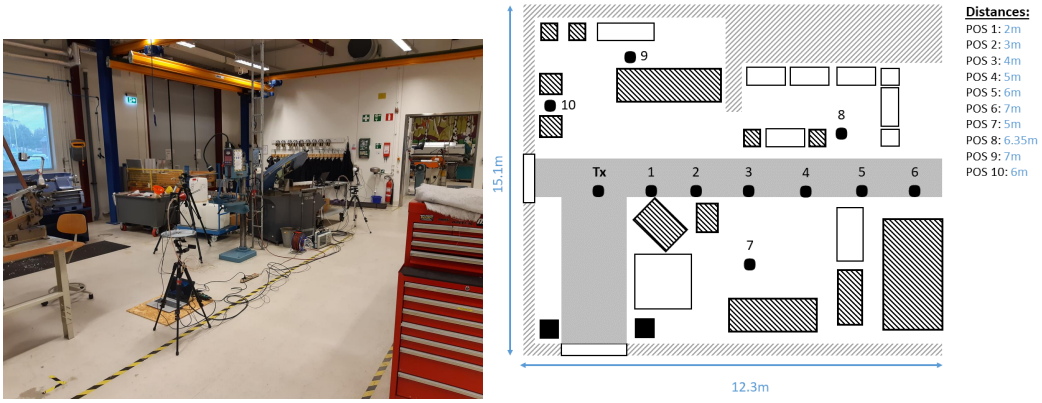

(a) HiG workshop (b) HiG workshop layout

Figure 4.13: Picture and layout of the HiG workshop

central corridor separates the room in two areas, and several meters exist between the machines, which makes the environment have a relatively low density of reflecting surfaces. During the measurements, the transmitter was fixed on one edge of the corridor and the receiver was placed in 10 positions in total: 6 LoS and 4 NLoS, with a total separation that oscillates between 2-7 meters. The LoS positions were measured at various distances in the corridor whereas the receiver was placed at locations where machines blocked the LoS component in order to evaluate the propagation in NLoS.

Pit oven from Ovako

Two different locations were measured around the pit oven from Ovako: the exhaust pipes and the fuel injection area.

EXHAUST PIPES:

The exhaust pipes are located at the lowest floor of the facility, next to the ovens. This scenario is composed of some horizontal metallic pipes that connect the ovens with a vertical chimney that is employed as a main exhaust line of the residual gases that are generated when fuel is burned to heat the ovens. A picture and the layout of this scenario can be seen in Figure 4.14.

As it can be seen in the picture, groups of 2x2 horizontal pipes that have an approximate diameter of 0.6 m each connect the ovens with the vertical chimney forming a triangular shape if seen from above. Apart from the pipes, some metallic pillars that support the higher floor structures are present in the environment as well and everything is made of metallic materials. In these measurements, the Tx was fixed in a static position and 8 Rx locations were measured in total: positions [1,2,3,6] were LoS and [4,5,7,8] were NLoS.

(a) Exhaust pipes (b) Exhaust pipes layout

Figure 4.14: Picture and layout of the exhaust pipes zone from Ovako

FUEL INJECTION AREA:

The fuel injection area is one floor above the exhaust pipes and it is composed of valves and injectors that send the fuel, which can be diesel or hydrogen, to the ovens. Figure 4.15 shows this site.

As shown in the picture, this site can be accessed using a corridor that is located on one side of the building, next to a wall that is made of bricks and has a metallic pillar. The fuel injection valves are mounted over some metallic frames located on the other side of the corridor and obstruct the vision partially. The vertical chimney that was introduced in the previous site is next to the frames as well, concretely in the center of this site. The transmitter was fixed on one side of the corridor during the measurements, and 5 LoS positions located at various distances on the corridor and 3

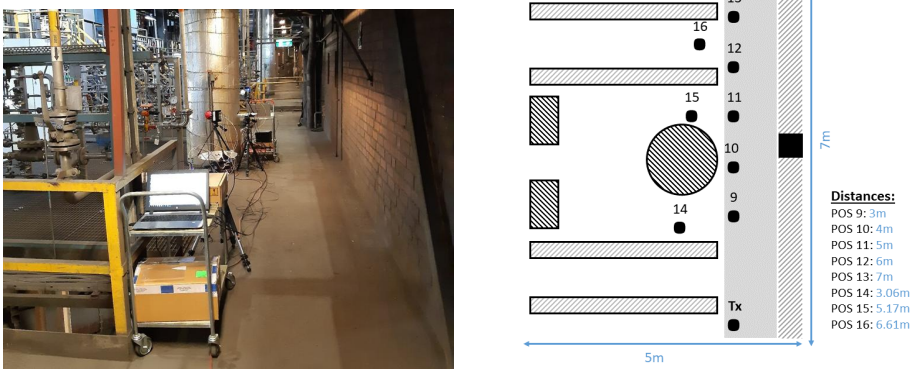

(a) Fuel injection area (b) Fuel injection area layout

Figure 4.15: Picture and layout of the fuel injection area from Ovako

NLoS one that used the metallic frames and the chimney as obstruction sources were measured in total.

4.2.3 Post-processing of data

The post-processing step has the objective of extracting the data of interest from the measurements, which include the number of multipath components and the power, delay and Tx/Rx angle combination of each individual element. This information is essential to carry out a performance assessment of the propagation, which is discussed in the next section.

The process begins by analysing all the individual CIRs that belong to a position. First of all, the directions that contain a multipath component are identified with the aid of a power mask. To do so, a matrix that contains the maximum power of each angle combination is generated first, an example can be seen in Figure 4.16 for the position 1 of the exhaust pipe scenario. A power mask that has a threshold of -110 dB of relative power between the Rx and Tx ends is passed over this matrix, which was selected following the criteria of choosing the lowest possible value that is above noise-floor peaks.

The individual CIRs that present a maximum power above the threshold are analysed in the next step. Here, it could be observed that each CIR contains just one multipath component, which is attributed to the highly directive radiation pattern of the antennas. Apart from this, the same multipath component could be appreciated in some neighbour orientations. This effect was attributed to the to the radiation pattern

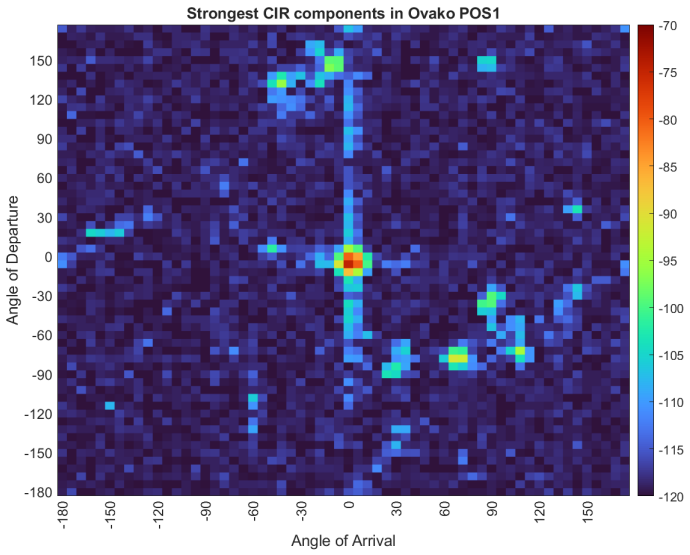

Figure 4.16: Heatmap of the strongest CIR components in Ovako POS1

of the antennas as well, because in some of these orientations the signal does not travel through the boresight. This makes some of the detected positions contain false information, since the angle combination and power of these CIRs is a byproduct of the real multipath component.

In order to avoid this issue, all the CIRs are grouped based on proximity in orientation and delay. At last, the component that contains the highest power within the group is assumed to be the real path, and the rest are discarded. The power, delay, Angle of Departure (AoD) and AoA of these components is stored at last to generate the performance metrics of the channel.

4.2.4 Results and comparison with existing works

This section details the propagation metrics that were computed based on the data acquired with the process described above. Three aspects of the propagation were considered for this process, since most works that can be found in the literature provide these metrics as well and a comparison can be performed. The metrics are the PL, DS and AS, and details regarding each are provided next.

Path loss

The different PL models that can be found in the literature were presented in Section 3.1.3. As these measurements were conducted over a single frequency band, the coefficient of just the CI and FI models were inferred from the measurements. This process was carried out using the LoS, NLoS and the strongest NLoS components of all the positions independently as in [63], and an example of the obtained results in the exhaust pipes scenario can be found in Figure 4.17.

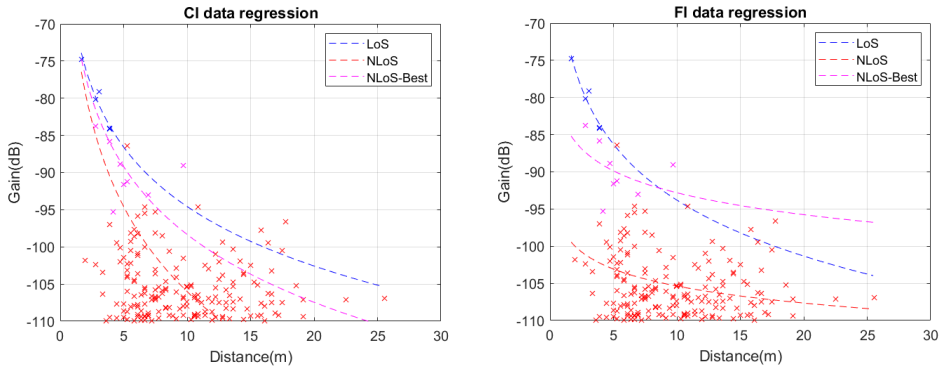

(a) CI regression (b) FI regression

Figure 4.17: PL model fitting in Ovako exhaust pipe scenario

All the inferred values for the model fitting are listed in Table 4.4. Two main conclusions were drawn after completing this process, which are detailed next.

In relation to the workshop, a work that estimates the PL in the same room is available in the literature for the 24 GHz band [80]. The article makes a parameter fitting for the CI and FI models as well, where the coefficients are $n = 1.89$, $\alpha = 62$ and $\beta = 1.67$ for the LoS case. These values show a clear consistency with the ones estimated in this measurement campaign, which indicates that the PL exponent does not vary significantly over frequency in this environment.

On the other hand, the scenarios from the steel company showed a significantly larger PL than all the works that were presented in Section 3.2.3, particularly the exhaust pipe area. The air of these sites was filled with carbon particles that are a consequence of burning the fuel and impurities of the metal in the ovens, which could be a possible cause of the additional PL of this scenario. However, due to the limited time and availability of the locations, this could not be tested further to validate this hypothesis.

Delay spread

The RMS DS of the multipath components was computed as described in Section 3.1.2. Both LoS/NLoS positions were treated separately during this process, and a RMS DS coefficient was computed per scenario and type. Figure 4.18 shows the Cumulative Distribution Function (CDF) of the DS in all the scenarios as well as a fit to the normal distribution.

As it can be seen in the figure, the DS is greater in the LoS positions and the workshop scenario. This is in accordance with the observations made in the PL estimation, since more power arrives to the reception under these conditions. This

Table 4.4: Fitted parameters for CI and FI PL models

		CI		**FI**		
Environment		***n***	σ	α	β	σ
LoS	**Workshop**	1.981	0.619	69.367	1.773	0.432
	Exhaust	2.656	0.917	68.791	2.501	0.891
	Valve	2.273	2.279	66.591	2.476	2.261
NLoS	**Workshop**	3.272	9.569	101.245	0.273	4.747
	Exhaust	3.801	7.869	97.756	0.76	4.892
	Valve	4.127	6.949	89.541	1.646	5.468
NLoS - Best	**Workshop**	2.689	7.606	94.75	0.126	4.216
	Exhaust	3.032	4.54	83.004	0.98	3.198
	Valve	3.037	5.255	79.627	1.63	4.561

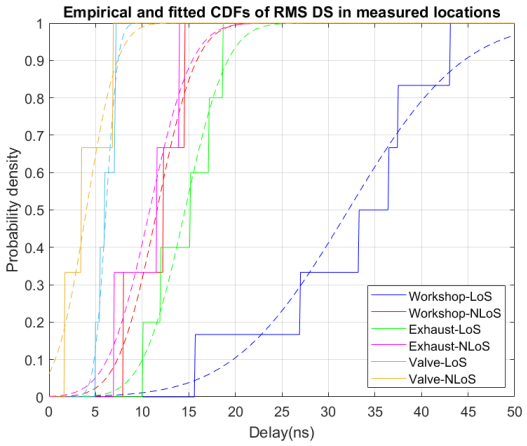

Figure 4.18: CDFs of measured and fitted RMS DS in all the environments

generates a stronger multipath and the coefficients suffer a greater dispersion in time, which is why the DS arises. Apart from this, the fuel injection valve shows the lowest dispersion in time, which is a result that can be explained with the layout of the area itself because the wall makes half of the azimuth orientations not reflect any multipath component.

In order to give some perspective to the obtained results, a comparison with existing works that characterize industrial sites over the mmWave spectrum was carried out next. Here, the measurement campaign presented in [86] and the ray-tracing based characterization done in [89] were used to perform the comparison, a detailed explanation of both works can be found in Section 3.2.3. Additionally, 3GPP has developed a channel model that works in the 0.5 - 100 GHz range [118], which is included in the comparison as well. The propagation metrics of a fictional indoor factory (InF) scenario that has a dimension of 10 x 10 x 10 m^3 and high clutter density were computed with the model presented in [118], because it is the approach that fits best to the measured scenarios. All the RMS DS metrics of these measurements and the other works can be found in Table 4.5. These metrics are presented in their logarithmic form, since this is the format that the 3GPP model uses for its estimations.

The first conclusion drawn from this comparison is that the DS metrics of the measured workshop, 3GPP-InF, [86]-Hall and [89]-Heavy scenarios do not vary significantly, which, considering the similarities between all the environments, is to be expected. Apart from this, a lower DS is measured in the pit oven and [89]-Light scenarios. This is attributed to a higher propagation loss in the first case and the scarcity of reflective surfaces in the second, which are two effects that provoke a decline in the temporal dispersion. At last, a higher RMS DS is detected in the LoS positions of the measured sites, which is contrary to the results provided by

Table 4.5: RMS DS coefficients of measured locations and other works

	DS			
	LoS		NLoS	
Environment	μ_{lg}	σ_{lg}	μ_{lg}	σ_{lg}
Workshop	-7.514	0.158	-7.948	0.134
Ovako exhaust	-7.846	0.111	-7.984	0.157
Ovako valve	-8.218	0.072	-8.464	0.303
3GPP - InF	-7.591	0.15	-7.526	0.19
[86] - Hall	-7.6	0.16	-7.4	0.12
[89] - Light	-7.872	-	-7.533	-
[89] - Heavy	-7.416	-	-7.306	-

other works. A hypothesis that could explain this behaviour is that the measured RMS DS of the NLoS positions is lower because fewer multipath components can be detected under these circumstances, which would effectively reduce the DS. Another possibility could be that the sample size is insufficient to obtain a statistically relevant metric, meaning that this result could be skewed. In any case, performing additional measurements would be necessary to have a better understanding of this behaviour.

Azimuth spread

The RMS AS of the measurements was computed as detailed in Section 3.1.2. As in the previous section, a separate set of metrics has been computed for the LoS/NLoS positions, and the Azimuth Spread of Departure (ASD)/Azimuth Spread of Arrival (ASA) metrics have been estimated independently as well. These results were also compared to the works [86, 89] and the output of the 3GPP model using a logarithmic scale, being all the metrics displayed in Table 4.6.

As it can be seen in the table, the NLoS positions have a greater dispersion in

Table 4.6: RMS AS coefficients of measured locations and other works

	ASD				ASA			
	LoS		NLoS		LoS		NLoS	
Environment	μ_{lg}	σ_{lg}	μ_{lg}	σ_{lg}	μ_{lg}	σ_{lg}	μ_{lg}	σ_{lg}
Workshop	1.57	0.214	1.84	0.158	1.55	0.289	1.94	0.08
Ovako exhaust	1.84	0.094	1.96	0.127	2.01	0.2	1.94	0.108
Ovako valve	1.83	0.153	2.15	0.039	1.95	0.287	1.98	0.053
3GPP - InF	1.56	0.25	1.57	0.2	1.46	0.414	1.72	0.3
[86] - Hall	1.53	0.03	1.55	0.06	-	-	-	-
[89] - Light	1.14	-	1.55	-	1.32	-	1.62	-
[89] - Heavy	1.62	-	1.8	-	1.77	-	1.71	-

azimuth in most cases, which is attributed to the lack of a predominant multipath component. Regarding the measurements from this campaign, the workshop scenario shows metrics that are similar to the ones of the other works, whereas the pit oven scenarios show the greatest dispersion values of the table. Since this environment is surrounded of metallic materials that reflect signals, the angle combinations that can generate multipath components are more diverse, which could explain the observed behaviour.

4.3 Summary

This chapter has described the first block of the development process of this thesis, which is composed of the elaboration of a mmWave channel sounder for industrial environments and a measurement campaign that covers different sites.

The first half of the chapter describes the elaboration and validation process of the channel sounder, which was published and presented in the WFCS 2022 conference under the *A Cost-Effective Directional Millimeter-Wave Channel Sounder for 60 GHz Industrial Wireless Communications* name [34]. The different parts that form the channel sounder were detailed at the beginning, where the front-end was described first, the four stages of the signal generation and acquisition architecture were detailed later and the sounding signal and calibration process were described at last. The validation process was explained in the end, which was composed of three different tests that aimed to ensure the correct operation of the equipment. The main conclusion drawn from this work is that the channel sounder is capable of measuring industrial scenarios in the 60 GHz frequency band with a space-time resolution that is adequate for the use case of interest.

The second half of the chapter shows a measurement campaign carried out with the channel sounder. These measurements were the product of a collaborative work between MU and HiG, and all the results were published and presented in the WFCS 2023 conference under the *60 GHz mmWave Signal Propagation Characterization in Workshop and Steel Industry* name [35]. Here, the configuration of the channel sounder was introduced first along the selected sites, which were a workshop and a pit oven from a steel factory. The post-processing that extracted the relevant data from the measurements was detailed later, and some metrics related to the PL, DS and AS were generated at last. These results were compared to other literature works, where the particularities of the measured environment were highlighted. The main conclusions drawn from this work are that the workshop is consistent with similar scenarios that were used as a comparison sources and that the steel factory is more challenging to

work with, since a higher PL, lower DS and larger dispersion in azimuth was detected for this scenario in particular.

Chapter 5

Channel model for mmWave propagation in industrial environments

This chapter explains the development process behind the elaboration of a stochastic channel model that represents mmWave electromagnetic signal propagation in industrial sites, which was the next goal of this thesis. To achieve this, an additional measurement campaign was carried out first, since the resolution and number of positions of the measurement campaign from the previous chapter (Section 4.2) were insufficient for this task. Details regarding these measurements, as well as the configuration of the channel sounder during this process, are provided first in this chapter. The next section describes the elaboration of the channel model, focusing on the design, parameterization and implementation steps. Following up, the validation process of the model is detailed, where the similarity between the model and the measurements is demonstrated. At last, a preliminary performance assessment of an IEEE 802.11ad link is done using the developed model as well as other two models that represent generic indoor scenarios with the aim of identifying the particularities of industrial sites, and a comparison of the obtained results is provided.

All this work was submitted to the IEEE Open Journal of the Industrial Electronics Society [37], and the manuscript is under review at the time of writing this document. The measurements were submitted to NIST's NextG Channel Model Alliance [36] public repository as well, which can be found as the *Measurements in a University Workshop with Industrial Equipment* dataset.

5.1 Measurement campaign in industrial workshop

The measurement campaign that generated the data for the elaboration of the model is detailed in this section. The configuration employed for the channel sounder is

presented first, and the selected workshop for the measurement campaign is described after. At last, the process that extracts the relevant information from the measurements is explained.

5.1.1 Channel sounder configuration

A complete list of the configuration parameters used by the sounder during these measurements is provided in Table 5.1.

Most of these parameters are the same as in the channel sounder design and the measurement campaign detailed in Section 4.2. The same chirp signal that was presented in the sounder design is employed to perform the measurements, and the antenna model and acquisition device configuration remain identical as well. The differences are in the band-converter configuration and the azimuth orientation, which have the goal of enhancing the resolution.

The band-converters are configured to use two different center frequencies: 59.94 and 61.02 GHz. These cover to the complete channel 2 defined by the 802.11ad standard because a bandwidth of 1.08 GHz is employed in each acquisition. On the other hand, the azimuth orientation is configured to perform 3º step rotations, which is roughly half of the HPBW area of the antennas and can be helpful to cope with antenna misalignment. As for the operation, the channel sounder performs two complete azimuth scans, one with each center frequency. The other alternative,

Table 5.1: Sounder configuration and operation parameters

Category	Parameter	Value
Sounding signal	Signal type	Chirp
	Freq. Range (MHz)	[-540 to 540]
	Duration (ns)	4000
Band conversion	Center freq. 1 (GHz)	59.94
	Center freq. 2 (GHz)	61.02
Antennas	Type	Horn
	Gain (dBi)	30
	HPBW (º)	6
Azimuth orient.	Center (LoS) (º)	0
	Step (º)	3
	Range (º)	[-180 to 180]
Acquisition	Sampling rate (Gsps)	2.5
	Number of samples	10000
Results per position	Data type	CIR
	Number of captures	28800
	Total memory (GBytes)	1.8

which is to make just one azimuth scan and re-configure the band converters in each orientation, was also considered. However, since the re-configuration process is significantly more time consuming, this idea was discarded in the end. With this configuration, 28800 CIRs (two scans of $(360/3)^2$=14400 orientation combinations) are captured in total per position, requiring 1.8 GBytes of storage. As for the duration of the acquisition, each position takes approximately 12 hours to measure with this configuration.

5.1.2 Selected scenarios and positions

The measurement campaign was carried out in a mechanical workshop that belongs to MU, which has a lot of similarities with other industrial workshops that can be found in the literature such as [78, 80, 81]. This environment contains a diverse set of machines such as vertical machining centers, drilling stations, metal cutters, milling stations, hydraulic presses and so on, and the layout can be very diverse depending on the surrounding equipment. Considering this, three different zones were selected for the measurements, and 10 locations were chosen in each site combining the LoS and NLoS cases. All the measurements were carried out at night, where all the machines were turned off and no activity was present. The three measured environments, which are named Vertical Machining Center (VMC), Milling Station (Mill) and Hydraulic Press Area (HPress), are detailed next.

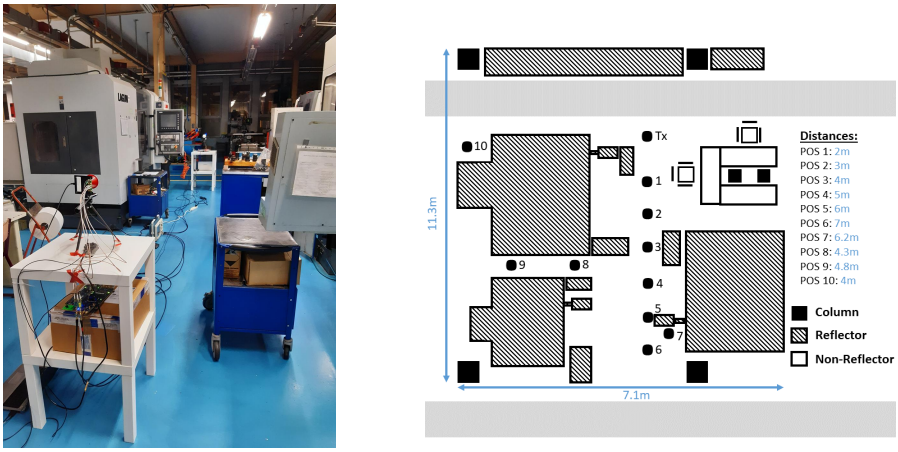

(a) VMC scenario (b) VMC scenario layout

Figure 5.1: Picture and layout of the VMC scenario

(a) Mill scenario

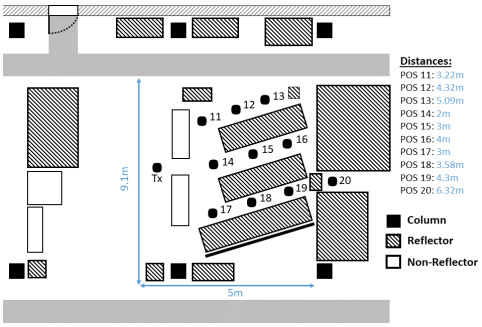

(b) Mill scenario layout

Figure 5.2: Picture and layout of the Mill scenario

(a) HPress scenario

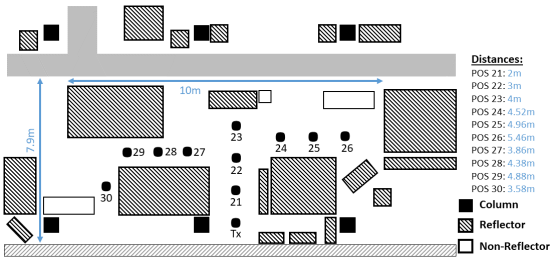

(b) HPress scenario layout

Figure 5.3: Picture and layout of the HPress scenario

Vertical machining center

The VMC area is centered at a corridor that makes three vertical machining centers accessible. These machines have the shape of big metallic box frames that are empty inside. Apart from these, this environment contains additional materials as the tool holders that are next to the machines, some metallic lockers located in front of a wall, wooden tables and chairs that have computers on top or metallic pillars that are part of the structure of the building. A picture and the layout of the site can be seen in Figure 5.1, as well as the selected positions for the measurements. Here, the Tx was fixed on one edge of the corridor and the Rx was moved around. Six LoS positions were measured first at various distances in the central corridor, and four NLoS position were acquired later, where the machines were used as blocking elements.

Milling station

The Mill zone is next to the VMC, and it is composed of three milling stations that have a height that partially blocks the vision between the antennas of the sounder in some

orientations. These machines are made of metallic materials and have irregular shapes, and one of them has a large metal plate on the back to collect metal chips. Apart from these, the environment contains additional metallic lockers that are located in front of the wall, some drilling stations, more metallic pillars and two wooden workbenches. The Tx end was placed between the workbenches during all the measurements, and the Rx was positioned around the milling stations. All the positions belong to the obstructed LoS case, since the machines and the antennas are of approximately the same height. Figure 5.2 shows a picture and the layout of this site.

Hydraulic press area

The HPress area is displayed in Figure 5.3. The main machines within this area are two hydraulic presses, an hydraulic press shear and an hydraulic press brake, which are separated by a narrow corridor. The machines are of large dimensions and present flat metallic surfaces, and the rest of the environment is composed of drilling stations, some wooden tables, a tool cabinet and additional metallic pillars. The Tx end was set to a fixed location during the measurements on an edge of a corridor, next to a wall of the building. Since direct vision is uncommon in this scenario, the Rx was placed in three LoS and seven NLoS positions.

5.1.3 Post-processing

The process that extracts the relevant information from the measurements is detailed in this section. The main goal of this step is to identify all the multipath components of each position and store their metrics, which are the power, delay, AoD and AoA.

The first step to achieve this goal is to join the CIRs from both frequency bands that belong to the same antenna orientation, because two independent measurements (centered at 59.94 and 61.02 GHz) were performed. To do so, the frequency response from both measurements is concatenated first and the result is brought back to the time domain with the IFFT operation, effectively doubling the sampling rate to 2.16 GHz.

The maximum power measured in each antenna orientation is extracted after to detect the multipath components. This processing step is the same as the one detailed in Section 4.2.3, where a power mask of -110 dB is employed to determine the presence of a multipath component in each orientation. This threshold is selected based on the noise floor.

Several neighbour directions showed to be above the threshold, and after analysing their delays, it was concluded that they contained the same multipath component with different gains. This is caused by the antenna radiation patterns, because not all the directions use the boresight and, consequently, artificial multipath components are

created. In order to solve this issue, the next processing step is to group all the detected multipath components based on proximity in orientation and delay. An example can be seen in Figure 5.4 for the position 1 of the VMC.

At last, a single element is selected from each group. The real multipath component is assumed to be over the antenna orientation combination that has the highest gain, because this can only be achieved when the antennas are aligned with the reflecting surface. In this process, the power, delay, AoD and AoA that correspond to the strongest element of each group are stored for the elaboration of the model and the rest are discarded.

5.2 Channel model elaboration

The elaboration of the stochastic channel model is described in this section. The design and structure of the model are described first. Then, the parameterization of the model, which details how to compute aspects as the PL and delay is detailed. At last, a Matlab implementation of the model is presented, and all the required parameters to elaborate it are provided as well.

5.2.1 Model design

The design of the channel model began by analysing the existing modeling approaches, some of which were described in Section 3.1.4. Here, it was observed that the basic form of the TDL model (3.23) had the potential to include all the extracted information, since this model represents the CIRs as an addition of multipath components, each

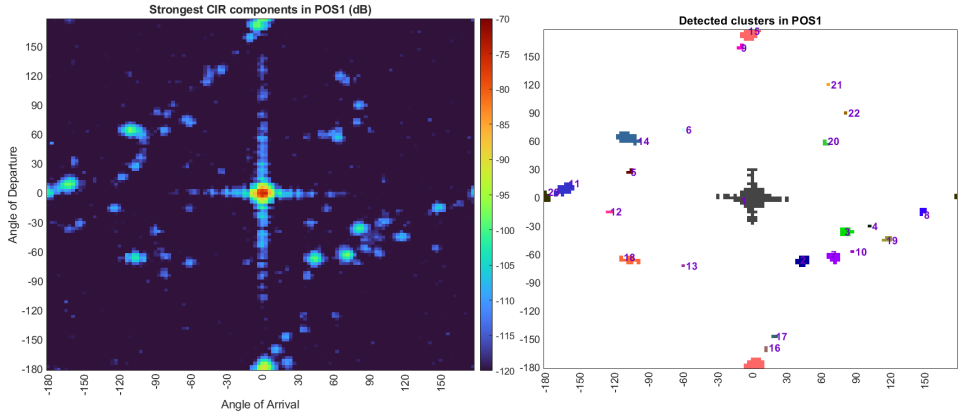

(a) Maximum power heatmap (b) Grouped multipath components

Figure 5.4: Heatmap of maximum power and detected multipath components in VMC POS1

with its own gain, delay and phase shift. As the measurements also include the directional aspect of the multipath components, it was concluded that the basic TDL was insufficient to represent all the available information. Consequently an extension that models this additional data was proposed, where the CIR can be expressed as:

$$h(\tau, \phi_{AoD}, \phi_{AoA}) = \sum_{i=0}^{N} A_i exp\left(-j\theta_i\right) \delta\left(\tau - \tau_i\right) \\ \delta\left(\phi_{AoD} - \phi_{AoD(i)}\right) \delta\left(\phi_{AoA} - \phi_{AoA(i)}\right). \quad (5.1)$$

This extension adds the parameters ϕ_{AoD} and ϕ_{AoA} to represent the azimuth angle in departure and arrival, respectively.

In order to implement this model, the amount of multipath components, as well as their gain, phase, delay and angles of departure and arrival must be previously estimated. These parameters are inferred from the measured data using both stochastic or deterministic approaches.

As for the PL, typical models separate all the measured positions in two groups to compute a set of metrics per case, which are LoS and NLoS. However, a great disparity between the received power of the multipath components was detected after performing the post-processing. It was concluded that grouping all the multipath components together would introduce a lot of variation and error, and in order to reduce this variation a categorization of the reflecting surfaces that generate the multipath components was carried out based on the received power (E_s). The FSPL, which is computed with the Friis transmission equation (3.2), was used to generate the power that would arrive at each measured delay, and the difference between this power and the measured one was used to perform the categorization. Four groups were defined in total:

- **LoS:** $FSPL \geq E_s > (FSPL - 10)$ dB, antennas close to (0,0).
- **Very Strong:** $FSPL \geq E_s > (FSPL - 10)$ dB, antennas far from (0,0).
- **Strong:** $(FSPL - 10) \geq E_s > (FSPL - 20)$ dB.
- **Weak:** $(FSPL - 20) \geq E_s > (FSPL - 30)$ dB.

As it can be seen, the first two groups are within the same power range. Some surfaces reflect almost all the power that impinges on them and in these cases the received power is almost the same as in LoS. These categories have the aim of separating both cases and use the antenna orientation to do so. The directions that are

close to (0,0) represent the scenario where both boresights of the antennas are aligned, which is only possible in LoS. Thus, these directions are assumed to belong to the direct path unlike the rest, which have at least one reflection. The remaining categories, which are labeled as strong and weak reflectors, are for multipath components that arrive with lower amplitude. Each category is set with a range of 10 dB, which is an arbitrary delimiter that suits well with the data. These categories cover all the detected multipath components above the -110 dB threshold, which is why no additional groups are required.

The categorization of multipath concludes with the main design of the channel model. As stated before, the number of multipath components, power, delay and angles must be estimated to apply the model, which are values that are inferred from the measurements. The parameterization of these aspects is discussed in the next section, considering the LoS/NLoS positions as well as the defined groups separately.

5.2.2 Model parameterization

This section explains the process followed to generate the formulas that represent the different parameters used in the extended TDL model, which are the number of multipath components, PL, excess delay and orientation in azimuth. As for the phase shift, this is represented with a random uniform distribution in all the scenarios. Even if the rest of the formulas are the same for all the cases, a different set of values is computed per scenario (VMC, Mill or HPress), position type (LoS or NLoS) and reflector type (LoS, very strong, strong or weak).

NUMBER OF MULTIPATH COMPONENTS:

A correlation between the separation between the antennas and the amount of received multipath components was detected in the post-processing of the measurements, as the closest positions yielded more multipath. This motivated to represent the number of multipath components as a variable that depends on the separation between antennas using a linear regression. The formula to implement this is

$$N_{refl.} = \alpha + 10\beta log_{10}(d) + X_{\sigma}, \tag{5.2}$$

where α is the intercept, β is the distance (d in meters) dependant slope and X_{σ} is a random variable that represents the error measured during the inference process. The main idea behind this last variable is to include the MSE of the measurements relative to the regression as a random fluctuation of the channel, and this is implemented with a Gaussian random variable with the $N(0, MSE)$ distribution.

PATH LOSS:

In Section 3.1.3, the different techniques to model PL were reviewed. Two of these

models are widely accepted in the literature to represent single frequency band measurements: CI and FI. Since these solutions can be appropriate to represent the PL of the model, this parameterization step has conducted an analysis of the suitability of both models in order to determine the alternative that fits best.

Two metrics were employed to carry out the analysis: the Root Mean Square Error (RMSE) and the R-Squared. The RMSE represents the error between the estimated data and the measured one, and it is computed as

$$RMSE = \sqrt{\frac{\sum_{i=1}^{N}(x_i - \hat{x}_i)^2}{N}}, \tag{5.3}$$

where x_i and $\hat{x}_i$ contain the measured and estimated sample i and N represents the total amount of samples. On the other hand, the R-Squared metric represents the percentage of the variance that a regression can explain for a dependent variable. This value can be achieved with

$$R^2 = 1 - \frac{\sum_{i=1}^{N}(x_i - \hat{x}_i)^2}{\sum_{i=1}^{N}(x_i - \bar{x})^2}, \tag{5.4}$$

where x_i and $\hat{x}_i$ are the measured and estimated values at index i and $\bar{x}$ represents the sampled mean.

These metrics were computed considering all the scenarios and reflector types independently, and a result set was elaborated for each case. All the obtained metrics can be found in Tables 5.2 and 5.3. The first conclusion drawn from the results was that both models offer a similar performance in the LoS path. However, the FI approach clearly outperformed the CI model in the rest of the reflectors. This result was expected, since the CI uses the FSPL as its intercept and this same metric was previously employed for the categorization of multipath components. As the CI model was not well suited to represent most of the reflectors and no clear advantage could be seen in the LoS case, it was concluded that the FI model was the best approach to represent the PL in the model.

Table 5.2: R-Squared value comparison of path loss models

R2		**LoS**				**NLoS**		
		LoS	**V.S. Refl.**	**S. Refl.**	**W.Refl.**	**V.S. Refl.**	**S. Refl.**	**W.Refl.**
VMC	**CI**	0.67	0.03	0	0	0.09	0	0
	FI	0.67	0.42	0.5	0.47	0.21	0.36	0.55
Mill	**CI**	0.7	0.5	0	0	-	-	-
	FI	0.82	0.54	0.52	0.4	-	-	-
HPress	**CI**	0.85	0.7	0	0	0.7	0	0
	FI	0.86	0.73	0.4	0.21	0.72	0.59	0.05

Table 5.3: RMSE value comparison of path loss models

RMSE		LoS				NLoS		
		LoS	**V.S. Refl.**	**S. Refl.**	**W.Refl.**	**V.S. Refl.**	**S. Refl.**	**W.Refl.**
VMC	**CI**	2.15	5.17	5.46	5.62	4.55	5.86	4.05
	FI	2.15	4	2.18	1.21	4.22	2.6	1.31
Mill	**CI**	3.1	4.16	5.11	6.47	-	-	-
	FI	2.35	3.98	2.39	1.16	-	-	-
HPress	**CI**	0.99	4.38	4.44	11.5	2.73	5.95	6.1
	FI	0.92	4.14	2.44	2.07	2.67	1.55	0.9

EXCESS DELAY ESTIMATION:

The process to estimate the delay that the multipath components have is detailed in this section. In order to perform a fair comparison between all the positions, the excess delay relative to the LoS path was analysed instead of the absolute value, as this estimation is independent of the distance.

A stochastic approach was selected to model the excess delay, and the best probabilistic distribution was searched using the Kolmogorov-Smirnov (K-S) method [119]. This method compares the CDFs of the measured data and the distribution under test, whose parameters are inferred from the measurements. The difference between both curves is then analysed in order to determine how accurate the fit is. The maximum distance d between both CDF curves is calculated with

$$d = \max_x \left(|F_0(x) - S_N(x)| \right), \tag{5.5}$$

where the estimated CDF is represented as $F_0(x)$ and the CDF of the empirical dataset, which is of size N, is $S_N(x)$.

A total amount of 24 distributions were tested with this technique. The obtained results were varied, as the datasets were relatively small for each case. Even if the best approach was not always the same, the Generalized Extreme Value (GEV) showed promising results, as it got the best or almost the best score in all the cases (its d value was less than 0.2 below the best approach in the worst case scenario). Since using different distribution for each case would add an unnecessary complexity to the channel model, all the measured data was fitted to the GEV distribution.

The PDF of the GEV distribution is computed as

$$\begin{aligned} PDF_{GEV} &= \frac{1}{\sigma} t(x)^{k+1} e^{-t(x)} \\ t(x) &= \begin{cases} \left(1 + k\left(\frac{x-\mu}{\sigma}\right)\right)^{-1/k}, k \neq 0 \\ e^{-(x-\mu)/\sigma}, k = 0 \end{cases} . \end{aligned} \tag{5.6}$$

As it can be seen, three parameters are required to characterize this distribution: the location (μ), scale (σ) and shape (k). A set of these values was computed for each scenario and reflector type, as the NLoS positions showed a significantly lower dispersion in time because less multipath arrives under this condition. At last, a minor inconvenience was detected with this distribution, which is that it can generate negative values even if they are unlikely. Since the delay must be always positive, the model is programmed to generate random numbers until a value that is greater than zero is obtained, effectively avoiding the mentioned issue.

ORIENTATION IN AZIMUTH:

The azimuth orientation modeling began by estimating the paths followed by all the multipath components, which was achieved using the antenna angle combinations, the delays of the multipath components and the layouts of the sites. Here, most paths showed to be 1^{st} order reflections (i.e. paths that reflect on just one surface before reaching the destination) and their distribution showed a clear pattern if these were displayed in the heatmap from Figure 5.4. This pattern is shown in Figure 5.5 for the frame of the previously employed heatmap with a blue dashed line, where the relation between the AoD and AoA is computed as

$$AoD[^\circ] = \begin{cases} +180 - \sqrt{180^2 - (AoA + 180)^2}, AoA < 0 \\ -180 + \sqrt{180^2 - (AoA - 180)^2}, AoA \geq 0 \end{cases} . \tag{5.7}$$

As shown in the figure, three different regions were defined in order to categorize the orientation of multipath in the azimuth plane: LoS, 1^{st} order and 2^{nd} order.

The first region includes all the directions that are close to (0,0), which is the case where both antennas are aligned. Since this direction range only makes sense for the LoS path, this region of the azimuth plane is reserved for it.

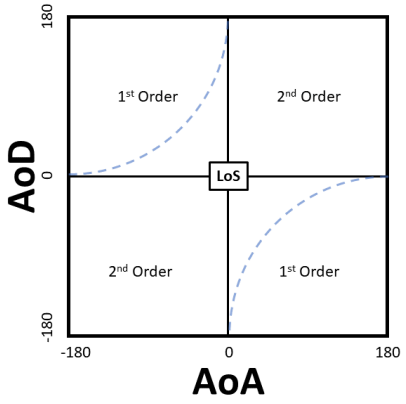

Figure 5.5: Azimuth angle regions seen from the heatmap frame

Then, two sections of the azimuth plane are assigned to the 1^{st} order region. This corresponds to all the antenna angle combinations where a 1^{st} order reflection path is possible, and the pattern shown in Figure 5.5 falls within this category. The majority of multipath components fall within this region, as the obtained data showed that approximately 8 out of 10 components are located here. These multipath components showed to have the shortest delays as well, since they correspond to paths that have a smaller distance compared to the ones from the 2^{nd} order region. Considering these points, the 80% of the multipath components (the ones with the shortest delays) generated by the model are assumed to be first order reflections. As for the location, the blue dashed line described in (5.7) is used as the starting point. A random location is selected first using a uniform distribution, and the MSE between this line and the measured orientations is used to add some randomness. To do so, two Gaussian random variables with the $N(0, MSE)$ distribution are employed, one for the departure axis and the other one for the arrival.

At last, the remaining 20% of the multipath components generated by the model are assigned to the 2^{nd} order region. As stated before, these correspond to paths that contain at least two reflection before reaching the destination, and, since more diverse angle combinations yield valid paths, there is no clear pattern that models the angular distribution of this kind of multipath components. Considering this, a random uniform distribution was employed to model the locations of the 2^{nd} order region.

5.2.3 Model implementation

The proposed model was implement in Matlab using all the concepts described in the design and parameterization steps. This model was named millimeter Industrial Channel Model (mmICM), and it was submitted to NIST's NextG Channel Model Alliance public repository along the data within the *Measurements in a University Workshop with Industrial Equipment* dataset. All the required parameters to implement this model can be seen in Table 5.4, where the key values to estimate the amount of multipath components from each category (*NReflectors*), the PL of each case (*GReflectors*), excess delay (*TReflectors*) and azimuth angle combination (*AReflectors*) are provided. This data, along the formulas and indications from the previous sections, are all the necessary information to implement this model.

The mmICM model can be configured to operate under different conditions by specifying the values of 10 parameters:

- **Scenario:** 'VMC', 'Mill' or 'HPress' (default: 'VMC').
- **Distance:** Tx/Rx separation (m) (default: 5).

Table 5.4: Parameter list for model realization

			NReflectors			GReflectors			TReflectors			AReflectors	
Scenario		**Type**	α	β	$X_\sigma(MSE)$	α	β	$X_\sigma(MSE)$	**k**	σ	μ	MSE_{AoD}	MSE_{AoA}
VMC	**LoS**	**LoS**	-	-	-	-67.229	-2.050	4.646	-	-	-	-	-
		V.S. Refl.	9.87	-0.975	2.152	-82.398	-1.474	16.121	0.465	10.620	11.790	174.482	135.807
		S. Refl.	9.812	-0.341	4.429	-93.964	-1.191	4.804	0.522	8.388	8.425	306.780	776.625
		W. Refl.	9.027	-1.024	0.516	-101.337	-0.839	1.454	-0.160	6.932	7.048	475.275	369.812
	NLoS	**V.S. Refl.**	9.651	-1.004	1.398	-80.153	-1.541	18.135	0.210	8.522	10.374	292.136	307.641
		S. Refl.	12.651	-1.004	1.594	-95.808	-1.038	6.821	0.281	9.916	9.966	266.050	200.611
		W. Refl.	12.355	-1.614	1.336	-96.806	-1.449	1.826	-0.239	4.292	5.284	692.398	593.386
Mill	**LoS**	**LoS**	-	-	-	-61.284	-3.422	6.042	-	-	-	-	-
		V.S. Refl.	9.166	-0.895	5.35	-74.273	-2.248	15.880	0.225	10.345	16.538	267.523	313.587
		S. Refl.	15.7	-1.487	2.414	-92.065	-1.371	5.669	-0.004	10.116	15.540	311.442	428.072
		W. Refl.	9.646	-1.025	3.858	-102.804	-0.660	1.343	0.380	4.679	6.128	180.131	432.904
HPress	**LoS**	**LoS**	-	-	-	-66.190	-2.017	0.886	-	-	-	-	-
		V.S. Refl.	19.321	-2.084	0	-72.452	-2.606	17.203	0.629	7.248	7.379	1282.296	533.146
		S. Refl.	20.66	-1.042	2.18	-91.541	-1.423	5.965	0.074	6.843	12.793	2776.315	1355.769
		W. Refl.	14.347	-1.549	1.013	-104.204	-0.492	4.311	-0.002	5.376	5.831	1332.435	1005.028
	NLoS	**V.S. Refl.**	5.501	-0.697	0.953	-71.272	-2.751	7.201	-0.401	9.246	11.822	85.398	118.098
		S. Refl.	29.757	-3.902	2.025	-96.835	-0.932	2.354	0.616	8.970	10.280	326.516	240.519
		W. Refl.	9.774	-1.27	0.472	-107.362	-0.166	0.808	-0.354	5.453	5.516	940.708	764.533

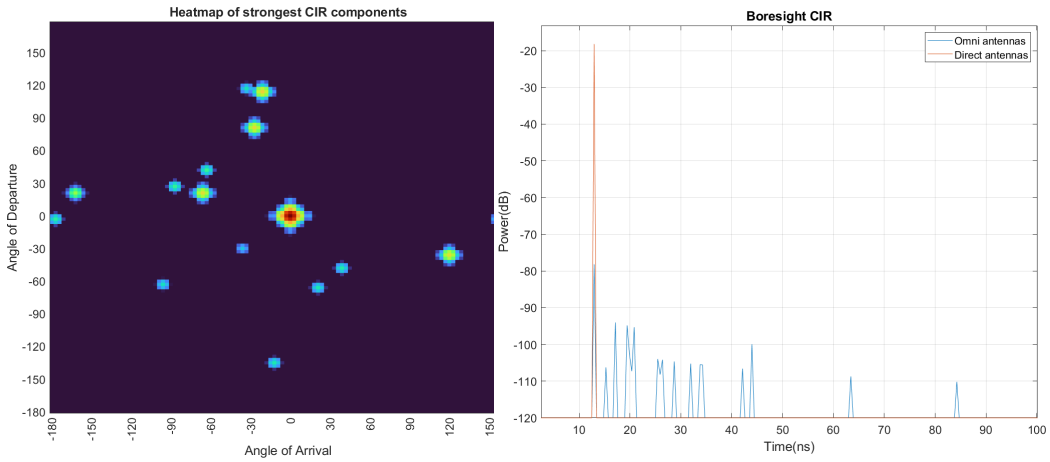

(a) Heatmap of maximum gain per direction (b) Boresight CIR of directional/omni antennas

Figure 5.6: Example CIR generated with the model

- **LoSPresent:** 'True' or 'False' (default: 'True').
- **SamplingRate:** Baseband sampling rate (SPS) (default: 2.16E9).
- **SpatialRes:** Spatial resolution (º) (default: 1).
- **NSamples:** Number of samples in time (default: 1E3).
- **RandNumGen:** 'default' or any integer (default: 'default').
- **MinDetPow:** Minimum detectable power (dB) (default: -120).
- **TxAntennaRP:** Radiation pattern in Tx (dBi) Coefficients must follow the spatial separation defined in SpatialRes. An empty array equals to the omnidirectional antenna (default: []).
- **RxAntennaRP:** Radiation pattern in Rx (dBi) Coefficients must follow the spatial separation defined in SpatialRes. An empty array equals to the omnidirectional antenna (default: []).

These parameters can be specified when the channel model object is created or when a realization of a channel is performed. There are four functions that allow to interact with the channel model object:

- **generateChannel(params)** Performs a realization of the channel with the configuration specified in 'params'. The realization is divided in two main steps. The information that describes the reflectors is generated first (NReflectors, GReflectors,

TReflectors, AoD and AoA). The second step performs a convolution between each reflector and the antenna radiation pattern in order to determine the reflector gain in the spatial domain.

- **cir = generateCIR(aod,aoa,plot)** Generates the complex baseband CIR of a given antenna orientation specified by the AoD and AoA parameters. The parameter plot is a boolean that generates a plot of the CIR in dB when set to 'True'.
- **displayHeatmap()** Displays a heatmap where the maximum amplitude of each antenna orientation combination can be seen in dB.
- **displayConfig()** Displays a list with the values of the configuration parameters the model is working with.

Additional information related to the channel model can be found by introducing the 'help mmICM' command in Matlab. This command provides an example model run as well, where the same channel realization is generated with both directional/omni antennas. Figure 5.6 shows both the heatmap and the CIRs that are achieved with this test.

5.3 Channel model validation

This section is aimed to prove that the CIRs generated with the model are truly correlated with the measured values. To achieve this, the technique shown in [120] is employed. This work compares the measured data to realizations of the model, focusing on the DS and AS aspects. The comparison is carried out with the CDFs of both approaches, because they should be correlated if the model truly represents the measured data. In this work, the validation process is carried out in both the delay and azimuth domains.

5.3.1 Delay validation

The validation of the dispersion in delay is carried out using the excess delay relative to the LoS path, since this is the parameter that the model generates to estimate the multipath component delays. The empirical CDF of the measurements is compared to the averaged value of 100 realizations of the model for the same scenarios, and the obtained results are separated in LoS/NLoS positions and each reflector type. An example of the comparison between the CDFs of the delays is provided in Figure 5.7 for the LoS positions in the VMC scenario, and the mean delay of all the scenarios can be found in Table 5.5.

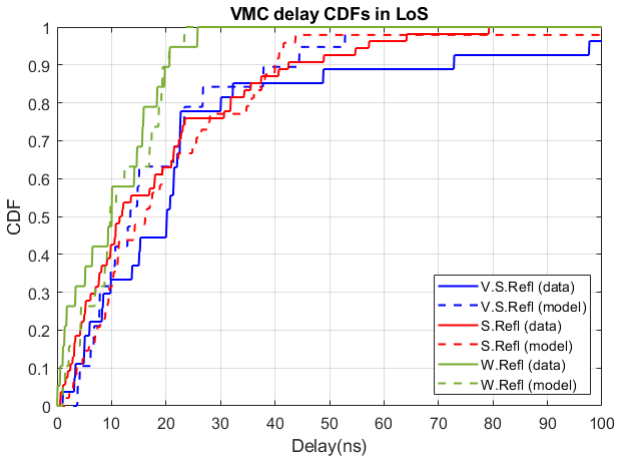

Figure 5.7: Measured and modeled CDFs of excess delay in VMC LoS

Table 5.5: Mean delay spread comparison between measurements and model

		LoS Excess Delay (ns)			**NLoS Excess Delay (ns)**		
		Measure	**Model**		**Measure**	**Model**	
		Mean	**Avg.**	**std**	**Mean**	**Avg.**	**std**
VMC	**V.S.Refl**	24.905	27.781	10.614	17.130	18.281	5.164
	S.Refl	18.665	22.425	9.862	18.919	20.403	4.149
	W.Refl	10.202	11.282	1.752	6.972	7.564	1.676
Mill	**V.S.Ref**	25.304	25.304	2.898	-	-	-
	S.Refl	21.363	21.518	1.497	-	-	-
	W.Refl	10.680	11.593	2.181	-	-	-
HPress	**V.S.Ref**	17.927	23.699	14.203	14.469	15.130	2.722
	S.Refl	17.2801	17.288	1.450	22.265	29.455	14.191
	W.Refl	8.9774	9.581	1.376	7.244	8.198	1.252

As for the results of this test, very similar mean delays are obtained in both approaches. The difference between the measurements and the model does not exceed the 10% in most cases, with the exception of the VMC LoS and HPress NLoS scenarios, where a difference of approximately 30 % can be appreciated. These particular positions are the ones that have the highest Standard Deviation (STD) as well, which means that the multipath components arrive in a wider time window in these cases and predicting them can be more challenging. In any case, the excess delay of the model resembles the one of the measurements with an accuracy that is believed to be sufficient to represent this aspect properly, since the observed variation is even lower than the one reported in [120].

5.3.2 Azimuth validation

As described in the realization of the model, the azimuth plane is divided in three different regions. To begin with, the LoS region is always located at the center. Next, the model computes the azimuth angle combination of the 1^{st} order region based on the curves that were shown in Figure 5.5, using the equation provided in (5.7). At last, the 2^{nd} order region, which represents the multipath components that require at leas two reflections in the model, is assumed to be randomly distributed with a uniform distribution. Since only first order reflections are correlated to the data, this is the only part that has been selected for the validation.

In order to validate this aspect of the model, the distance between the CDF curves of the measured angular dispersion and the averaged value of 100 realizations of the model is computed. This comparison is performed for each scenario, considering LoS/NLoS position and departure/arrival angles separately since the model estimates them independently in each case. An example of the comparsion between the CDFs can be seen in Figure 5.8 for the LoS case of the VMC scenario, and all the results are provided in Table 5.6.

As it can be seen, a slightly lower angular spread is present in the model in all the cases, where the difference between both approaches is of 8º in the worst case scenario. This can be explained with the measurements, because not all of the 1^{st} region multipath components are first order reflections. This means that their corresponding angle combinations are arbitrary and do not necessarily need to be correlated with the drawn curve, which increases the average distance. Even if this difference is present between both approaches, their metrics are considered to be close enough to validate this aspect of the model.

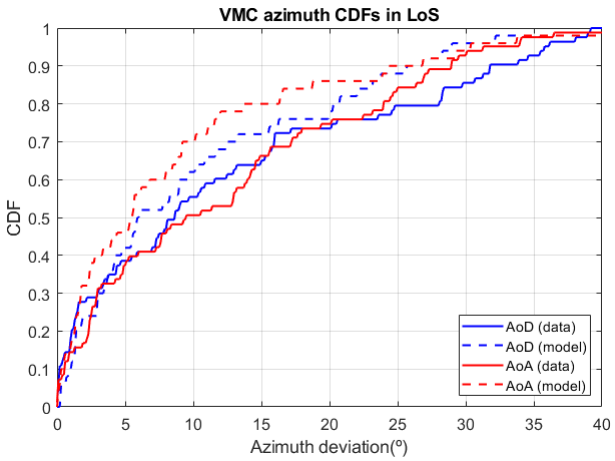

Figure 5.8: Measured and modeled CDFs of azimuth offset in VMC LoS

Table 5.6: Mean azimuth offset comparison between measurements and model

		LoS Azimuth Dispersion (º)			NLoS Azimuth Dispersion (º)		
		Measure	Model		Measure	Model	
		Mean	Avg.	std	Mean	Avg.	std
VMC	AoD	12.5075	10.4306	1.3697	12.795	9.9917	1.9995
	AoA	13.6881	7.6022	1.0439	12.503	6.9698	1.4267
Mill	AoD	10.5645	9.8746	0.8608	-	-	-
	AoA	12.3268	7.3785	0.7744	-	-	-
HPress	AoD	25.1962	19.8683	2.8343	16.962	10.241	1.9929
	AoA	18.602	14.6555	1.9807	15.482	7.2527	1.2884

5.4 Performance assessment of the channel model

This section aims to provide a preliminary assessment of the performance that a mmWave communication protocol can achieve in industrial sites using the elaborated model. The main goal is to compare it with existing models that represent generic indoor environments in order to identify the differences of their corresponding sites and find the opportunities and challenges that industrial scenarios may pose.

In order to achieve this task, the transmission of an 802.11ad Physical Service Data Unit (PSDU) is evaluated. The newer 802.11ay version of the standard was considered for the simulations as well, but due to its novelty it presents several challenges as the lack of literature works to compare it, not being implemented in real HW yet or the scarce amount of tools to operate with it in simulated environments. Consequently, the 802.11ad was selected since it does not have these issues while being a valid standard to perform the comparison.

The comparison is performed with MC simulations [92]. In these simulations, a realization of a channel model is used in each iteration, and different levels of Additive White Gaussian Noise (AWGN) are added in order to evaluate various SNRs. The BER from each case is computed and averaged later, from where the SNR/BER curves are obtained. As for the employed tool, the WLAN toolbox from Matlab [121] is selected, as it offers all the required functionalities to work with the PHY layer of the 802.11ad standard. The MC simulation is configured to perform 1E6 iterations in order to obtain statistically significant results at error rates of approximately 1E-5 (the estimation would be in the [0.5E-5, 1.8E-5] interval with a 95% confidence level), and all the SNR values in the (-10:2:10) dB range are evaluated in each iteration.

The structure of the PSDU is defined in accordance with the requirements listed in [8]. Several industrial communication types are categorized in this article based on the network size, range, reliability and similar parameters. Class 1 communications,

which are oriented to Closed Loop Regulatory Control applications, are taken as the reference for this comparison, where an update rate of 0.25 ms, a total network size of 30 nodes and a payload of 64 bytes per packet are defined. In order to satisfy these requirements, a total throughput of 30.72 Mbps is required, which can be covered with any MCS defined in 802.11ad as it was shown in Section 3.4 (Table 3.5). The MCS 1 is selected for this test, since the aspect under test is reliability and this mode is the most robust option.

At last, the performance of the standard over the mmICM developed in this work is compared to two models that represent propagation over the same frequency band. These are the 802.11ay [122] and NYUSIM [123] models, and two LoS scenarios are used for the testing, where separations of 5 and 10 meters are defined between the stations. Details regarding these models are provided next.

The 802.11ay channel model [122] follows a Quasi-Deterministic (Q-D) approach with ray tracing. Three types of scenarios can be selected for the realizations, which are an open area hotspot, street canyon and a large hotel lobby. The 3-D environment is created first with the given dimensions, and a Tx/Rx pair is placed at a specific location. Other configuration parameters are also used to specify antenna dimensions, beamforming and similar settings. With this, the model would be ready to work with any input signal, and a realization is done by generating both deterministic (depending on the layout) and stochastic (random events) rays that are later combined to elaborate the CIR. In this comparison, the hotel lobby scenario is selected with a physical separation of 5 and 10 meters between Tx/Rx. A single patch antenna is set in each end in order to get a radiation pattern as isotropic as possible, and both ends are faced towards each other.

The NYUSIM model [123] follows a stochastic approach that groups the multipath components in time clusters that contain different spatial lobe sizes along the CI model for path loss estimation. It offers five different scenarios: urban microcell, urban macrocell, rural macrocell, indoor hotspot and indoor factory. There are a total of 28 configuration parameters in the model, where aspects as Tx/Rx separation, LoS presence or blockage can be defined. The model estimates the channel parameters by performing N different simulations, where the receiver is placed at random locations between a predefined set of ranges. Some of the generated outputs are files that contain data related to AoD/AoA power spectrum or the PDP. The MC simulations carried out in this comparison are done with the configuration that approaches best to the other models, which is the indoor factory scenario with a fixed physical separation of 10 meters and a single patch antenna in both ends. Unfortunately, the minimum distance this model operates over is of 10 meters, which is why it is not possible to include its

results in 5 meters.

Results from both tests are discussed next. The SNR/BER curves found in Figure 5.9 show two different graphs that correspond to the 5 and 10 meter tests, respectively. As it can be seen, the achievable performance of the standard is very similar over both the mmICM and 802.11ay models, at least in the 5 meters case. This is in accordance with the measurements from both models, since a predominant LoS component is always present in the CIRs and first order reflections are at least 10 dB lower. On the other hand, the difference that both approaches present at 10 meters could be explained with the techniques that the models use to generate multipath. In mmICM, the amount of multipath components decreases as distance arises, whereas the ray-tracing approach used in 802.11ay does not consider the separation between stations and has a fixed amount of multipath. The 802.11ay model could be suffering a greater multipath at 10 meters, which is why its BER is slightly higher.

At last, a significantly worse performance can be appreciated with the NYUSIM channel. In this case, the measured power difference between the LoS path and reflected rays in [85] is similar to the one of the other works, but the model uses another approach to estimate the channel. The NYUSIM models the arrival of a multipath component as a group of rays that have very similar amplitudes and delays. This applies to the LoS path as well, which means that the multipath suffered in this model is significantly worse than the other ones. If this is added to the fact that the modem lacks to ability to cope with heavy multipath, the observed error floor could be explained. At last, the error rate seen with the mmICM is similar to the one of the more generic indoor scenarios, which could indicate that mmWave communications can have the potential to operate in industrial settings.

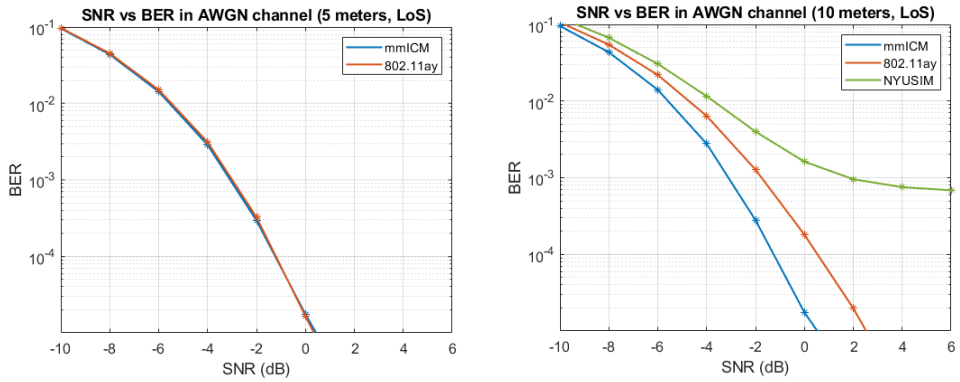

(a) Performance at 5 meters

(b) Performance at 10 meters

Figure 5.9: Performance of an 802.11ad link evaluated with the mmICM, 802.11ay and NYUSIM models

5.5 Summary

This chapter describes the process behind the elaboration of a mmWave propagation channel model that represents industrial scenarios. All the work presented during this chapter was submitted to the IEEE Open Journal of the Industrial Electronics Society as the *Measurement based stochastic channel model for 60 GHz mmWave industrial communications* article [37], and the manuscript is under review at the time of writing this document. The measurements were submitted to NIST's NextG Channel Model Alliance [36] public repository as well, which can be found as the *Measurements in a University Workshop with Industrial Equipment* dataset.

As for the contents of the chapter, the measurement campaign was detailed first, where all the necessary data to elaborate the model was obtained. Information regarding the channel sounder configuration, the measured location and the post-processing was provided here. The location was a workshop from MU, which was divided in three areas named VMC, Mill and HPress. Thirty positions (19 LoS and 11 NLoS) were acquired in total over these areas, covering all the channel 2 used in the 802.11ad standard, and all the acquired data was submitted to NIST's NextG Channel Model Alliance public repository [36] under the *Measurements in a University Workshop with Industrial Equipment* dataset.

In the next section, the elaboration of the channel model was discussed, which was named mmICM. The elaboration process was divided in three steps. The main design was introduced first, where an extension of the TDL model was proposed and the different multipath components were divided in categories depending on their relative strength. The parameterization of the model came next, where the formulas and techniques to compute the number of multipath components, PL, excess delay and orientation in azimuth were provided. At last, a Matlab implementation of the model was shown, where the configuration parameters and functions were described and an example run was displayed. A table containing all the parameterization coefficients of the model was provided here as well, which can be used to implement the model in any simulation environment. The Matlab implementation of the mmICM model was also submitted to the previously introduced dataset and is publicly available.

Next, the validation of the channel model was presented. The similarity between the measurements and the model was analyzed in this section, since the model must generate channels that are in accordance with the observations. The excess delay and azimuth angle orientation aspects were considered for this validation, where a clear correlation was shown between the mean values of the measured and modeled data, demonstrating the similarity between both approaches.

At last, a preliminary analysis was carried out where a 802.11ad frame was transmitted over the mmICM and two indoor generic models, which were the 802.11ay and NYUSIM. This analysis was done with the aim of searching differences between industrial and more generic indoor scenarios in order to detect the opportunities and challenges of this kind of site. The obtained results showed that the standard operates with a similar performance over all the channels, which indicated that mmWave communications could be a potential candidate for industrial use cases.

Chapter 6

Simulation based performance analysis of a mmWave communication system in industrial settings

This chapter is focused on the analysis of the achievable performance of an IEEE 802.11ad industrial networks. As it has been said in Section 1.1, industrial communications have strict requirements in terms of reliability and timing, because any error can put the process under control in danger and derive into an undesirable outcome that can vary between the interruption of the process and the cost of human lives. The main goal of this test is to determine the suitability of a protocol that operates over the mmWave spectrum for this task, and the IEEE 802.11ad standard has been selected because it is widely discussed in literature, easy to simulate and equipment that implement it is already commercially available. Existing 802.11ad characterization works, which were extensively discussed in Section 3.4.2, are mainly oriented to the achievable throughput, since this is the most appealing feature of this technology thanks to the huge available bandwidth of 2.16 GHz per channel. As the concept of using communication systems over the mmWave spectrum for reliable data exchange has not been extensively analysed in the literature, very few works explore the performance of the standard in terms of reliability and time-critical aspects, which is the main motivation behind this chapter.

Since simulating complex channels for a whole network is an extremely resource intensive task, the simulation has been split in two steps. In the first simulation, an individual link is analyzed with a realistic channel model under several conditions, where reliability related metrics are extracted. On the other hand, the second simulation explores the behaviour of a complete network using the previous reliability metrics to

represent the medium, which simplifies the channel implementation and significantly decreases the amount of required operations.

This chapter begins by checking the requirements that the network must fulfill in an hypothetical industrial use case, as well as the available simulation tools and equipment that can be simulated. The next section details the individual link simulation, where its objective, procedure and results are described. The network level simulation is presented after, where two topologies that fulfill different roles are analyzed in total. Again, the objective, procedure and results from each test are detailed in the section. At last, the main results and conclusions are summarized.

A conference paper named *Simulation based IEEE 802.11ad performance assessment in factory workshop* has been written with all the results obtained in this chapter [38]. This has been accepted in the IEEE Conference on Standards for Communications and Networking (CSCN), which will be held on November 2023.

6.1 Simulated network requirements and tools

This section begins by revisiting the different factory oriented network types, from where a use case is selected and its requirements are analyzed. Apart from this, the properties of an existing 802.11ad COTS router are extracted to include them in the simulations and make them as realistic as possible. At last, the tools that perform the simulations are selected.

6.1.1 Requirements of the network

The different use cases that fulfill industrial communications were briefly detailed in Chapter 1, where the main motivations behind this thesis were provided. Here, Table 1.1 showed that these use cases can be divided in classes depending on how demanding the requirements are in terms of maximum latency, number of devices, range and similar metrics [8]. Since this study aims to test the most stringent operational use case, class 1 requirements have been selected, which correspond to closed loop regulatory control applications. The performance metrics that this kind of network must provide are listed below:

- **Latency:** 0.25 to 4 ms.
- **Reliability:** Maximum PER of 10^{-7}.
- **Scale:** 10 to 30 links.
- **Range:** 10 to 30 meters.

- **Payload:** 8 to 64 data Bytes.
- **Update rate:** 125 to 2000 Hz.

6.1.2 Simulated equipment

Some properties of a COTS 802.11ad router are included in the simulations in order to generate realistic results. Concretely, the Talon AD7200 [62] router is selected because the work presented in [124] performs a characterization of this device and information as its available antenna radiation patterns is provided. Here, two different patterns are selected for the simulations named sectors 27 and 63 in [124]. These can be found in Figure 6.1.

The idea behind the selection of those two specific radiation patterns is to be able to analyze both sides: a highly directional radiation pattern that has a relatively narrow main lobe and a radiation pattern that is closer to the omnidirectional case. At last, the Tx power is extracted from the datasheet provided by the vendor in [62], which is of 10 dBm.

6.1.3 Simulation tools

As for the simulation of the network, the available tools were analysed first in Section 3.3, where a summary of the main features of each tool was done. An extension of the NS-3 is provided in [125], which includes all the functionalities to operate with the 802.11ad standard as well as its newer version, the 802.11ay. Since there are no more alternatives to represent 802.11ad operated networks, this extension of the tool is selected to perform the simulations. However, NS-3 is a discrete event simulator, which means that some channel effects as multipath cannot be properly simulated. For this reason, the individual links of the network are simulated apart with a tool that is capable of representing more realistic channels as the mmICM developed in Chapter 5, which is the WLAN toolbox from Matlab [121]. The main idea is to

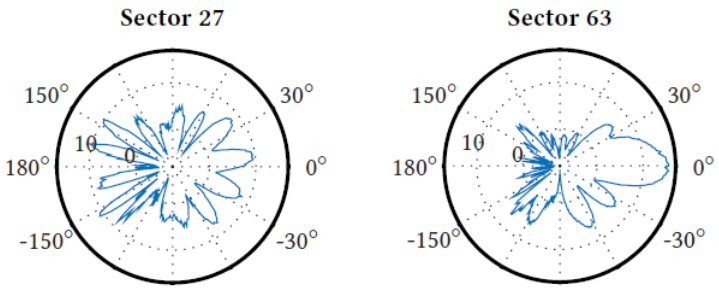

Figure 6.1: Sectors 27 and 63 of Talon AD7200 [124]

compute the PER of the links with this tool and include this metric later in NS-3, where a communication error will randomly occur based on the PER assigned to that link. The design, parameters and results of both simulations are discussed next.

6.2 Link level simulation

As mentioned earlier, the link level simulation is carried out in Matlab and has the goal of obtaining the PER of an 802.11ad link under several conditions. To achieve this, MC simulations [92] are carried at the link, using a system that modulates, transmits, receives and de-modulates 802.11ad Physical Protocol Data Units (PPDUs). The complete list of configuration parameters is detailed in Table 6.1 for the link level simulations.

As it can be seen, the propagation medium of the simulations is represented with the mmICM elaborated in Chapter 5. Here, the VMC scenario is selected, and several distances and SNRs are tested for the LoS and NLoS cases. As for the 802.11ad standard, the MCS 1 has been selected because it offers a sufficient throughput while being the most robust mode. The MCSs that belong to OFDM were considered as well, but as their inclusion is optional and not all the COTS equipment supports them, they were discarded in the end. The payload of individual packets is set to 156 Bytes, which is the required length to encapsulate 64 data Bytes (which is the maximum payload defined in the requirements) using the smallest overhead (UDP and IPv4). At last, the equipment is configured to transmit using the power and antenna radiation patterns that were previously selected.

The amount of required MC iterations is computed with the reliability requirement of a PER of 10^{-7} as the reference. Here, it was observed that over 10^9 iterations are required in order to achieve the confidence interval of $[0.8 * 10^{-7}, 1.2 * 10^{-7}]$ with a confidence level of 95%, which is not a viable goal considering the available

Table 6.1: Link level simulation configuration

	Parameter	Value
Environment	Scenario	VMC (LoS, NLoS)
	Distance (m)	2:1:10
	SNR (dB)	0:2:40
DMG Frame	MCS	1
	Payload (Byte)	156
Talon	Tx Power (dBm)	10
	Sector	27, 63
Monte Carlo	Iterations	1E6

computational capabilities. It was observed that a simulation of 10^6 iterations can guarantee a confidence interval of [$0.5*10^{-5}$, $1.8*10^{-5}$] for an error rate of 10^{-5} with a confidence level of 95%, which is an approach that can be simulated in approximately one day. Considering that 36 simulations are required in total (9 separate distances, tested over LoS/NLoS and antenna sectors 27/63), it was concluded that this resolution was acceptable, at least for a first approach.

All the simulations were carried out with the configuration showed above, the results can be found in Tables 6.2 to 6.5 for all the scenarios. The first conclusion drawn from these tables is that the LoS scenarios are significantly more reliable than the NLoS ones, since an error-free communication can be obtained if a sufficient SNR is achieved. This is not the case for the NLoS scenarios, where an error floor is present in all the cases. Apart from this, it can also be observed that communications over sector 63, which uses the directional antenna radiation pattern, perform better than the ones over sector 27. This difference is more noticeable in the NLoS case, where the error is an order of magnitude lower. A possible cause of this behaviour can be that the directional radiation patter finds the strongest multipath component and amplifies it as much as possible whereas the other alternative amplifies directions that contain just noise.

Table 6.2: MC results for PER in Sector 27 LoS

		SNR(dB)										
		2	**4**	**6**	**8**	**10**	**12**	**14**	**16**	**18**	**20**	**22**
Distance(m)	**2**	0.9987	0.6610	0.0638	0.0011	1.2E-5	3.0E-6	0	0	0	0	0
	3	0.9989	0.6752	0.0697	0.0015	3.9E-5	1.0E-6	0	0	1.0E-6	0	1.0E-6
	4	0.9990	0.6828	0.0729	0.0018	6.1E-5	4.0E-6	0	0	1.0E-6	0	1.0E-6
	5	0.9991	0.6868	0.0749	0.0021	8.5E-5	1.1E-5	1.0E-6	2.0E-6	1.0E-6	1.0E-6	3.0E-6
	6	0.9991	0.6875	0.0755	0.0022	1.0E-4	1.0E-5	6.0E-6	4.0E-6	3.0E-6	3.0E-6	3.0E-6
	7	0.9991	0.6876	0.0755	0.0022	1.1E-4	1.9E-5	8.0E-6	5.0E-6	5.0E-6	3.0E-6	6.0E-6
	8	0.9992	0.6867	0.0742	0.0022	1.1E-4	2.6E-5	1.2E-5	5.0E-6	7.0E-6	4.0E-6	5.0E-6
	9	0.9992	0.6849	0.0735	0.0020	1.2E-4	2.1E-5	1.2E-5	8.0E-6	6.0E-6	4.0E-6	8.0E-6
	10	0.9991	0.6836	0.0723	0.0019	1.2E-4	3.1E-5	1.1E-5	8.0E-6	7.0E-6	9.0E-6	1.0E-5

Table 6.3: MC results for PER in Sector 27 NLoS

		SNR(dB)										
		2	**4**	**6**	**8**	**10**	**12**	**14**	**16**	**18**	**20**	**22**
Distance(m)	**2**	1.0000	0.9744	0.6063	0.1528	0.0177	0.0016	0.0004	0.0003	0.0003	0.0003	0.0003
	3	1.0000	0.9632	0.5598	0.1368	0.0172	0.0024	0.0010	0.0009	0.0008	0.0009	0.0010
	4	1.0000	0.9437	0.4949	0.1169	0.0169	0.0038	0.0023	0.0020	0.0019	0.0020	0.0021
	5	0.9999	0.9192	0.4321	0.1006	0.0174	0.0055	0.0038	0.0033	0.0031	0.0032	0.0034
	6	0.9999	0.8991	0.3906	0.0922	0.0183	0.0070	0.0049	0.0042	0.0041	0.0041	0.0042
	7	0.9999	0.8869	0.3749	0.0915	0.0199	0.0081	0.0055	0.0047	0.0045	0.0045	0.0047
	8	0.9999	0.8790	0.3659	0.0917	0.0210	0.0087	0.0061	0.0052	0.0048	0.0048	0.0049
	9	0.9998	0.8693	0.3512	0.0895	0.0211	0.0088	0.0062	0.0053	0.0049	0.0049	0.0049
	10	0.9998	0.8549	0.3269	0.0830	0.0204	0.0087	0.0060	0.0050	0.0047	0.0045	0.0045

Table 6.4: MC results for PER in Sector 63 LoS

		SNR(dB)										
		2	**4**	**6**	**8**	**10**	**12**	**14**	**16**	**18**	**20**	**22**
Distance(m)	**2**	0.9986	0.6358	0.0548	0.0007	1.0E-6	0	0	0	0	0	0
	3	0.9987	0.6415	0.0559	0.0007	1.0E-6	1.0E-6	0	0	0	0	0
	4	0.9988	0.6454	0.0565	0.0007	2.0E-6	0	0	0	0	0	0
	5	0.9989	0.6485	0.0573	0.0008	0	0	0	0	0	0	0
	6	0.9990	0.6493	0.0580	0.0008	1.0E-6	0	0	0	0	0	0
	7	0.9989	0.6521	0.0585	0.0008	1.0E-6	0	0	0	0	0	0
	8	0.9990	0.6525	0.0582	0.0007	2.0E-6	0	0	0	0	0	0
	9	0.9990	0.6541	0.0587	0.0007	3.0E-6	1.0E-6	1.0E-6	1.0E-6	1.0E-6	1.0E-6	1.0E-6
	10	0.9990	0.6551	0.0591	0.0008	2.0E-6	0	0	0	0	0	0

Table 6.5: MC results for PER in Sector 63 NLoS

		SNR(dB)										
		2	**4**	**6**	**8**	**10**	**12**	**14**	**16**	**18**	**20**	**22**
Distance(m)	**2**	0.9998	0.8395	0.2590	0.0427	0.0048	0.0005	0.0002	0.0002	0.0001	0.0001	0.0001
	3	0.9998	0.8194	0.2278	0.0358	0.0044	0.0006	0.0003	0.0003	0.0002	0.0002	0.0002
	4	0.9998	0.8010	0.2002	0.0300	0.0040	0.0008	0.0004	0.0003	0.0003	0.0003	0.0003
	5	0.9997	0.7816	0.1778	0.0255	0.0036	0.0009	0.0005	0.0004	0.0004	0.0004	0.0004
	6	0.9997	0.7682	0.1620	0.0225	0.0034	0.0010	0.0006	0.0005	0.0004	0.0004	0.0004
	7	0.9997	0.7602	0.1522	0.0207	0.0035	0.0010	0.0006	0.0005	0.0004	0.0004	0.0004
	8	0.9997	0.7532	0.1444	0.0190	0.0033	0.0010	0.0006	0.0005	0.0004	0.0004	0.0004
	9	0.9996	0.7451	0.1358	0.0174	0.0032	0.0010	0.0007	0.0005	0.0004	0.0004	0.0004
	10	0.9996	0.7379	0.1266	0.0156	0.0030	0.0010	0.0007	0.0005	0.0004	0.0003	0.0003

6.3 Network level simulation

As describer earlier, the network level simulation is carried out in NS-3 and has the aim of evaluating the performance of the 802.11ad standard at a larger scale. Here, two topologies are tested in total: one where a sensors and actuators network is considered and another that represents the backhaul network of a workshop. Details regarding each are discussed next.

6.3.1 Topology 1: Sensors and actuators

The first tested network is shown in Figure 6.2, where the control of a sensors and actuators network is done with the 802.11ad standard.

Here, a centralized AP is attached to a controller that operates with four sensors and actuators pairs (8 separate devices). Each pair uses a different link for data exchange, alternating between LoS/NLoS and sectors 27/63. The distances of the nodes have been arbitrarily assigned, where a separation of 3 meters exists in NLoS and 6 meters in LoS. At last, the network is expected to operate with a periodically repeating structure that lasts 1 ms at most, where the sensors must send a payload of 100 bits to the AP and the AP must send one 100 bit packet to each actuator.

The complete list of configuration parameters employed in this simulation can be found in Table 6.6.

As for the IEEE 802.11ad standard, a BI of one TU (or 1024 μs) is selected in order to provide the fastest update rate possible. During the DTI of the beacon,

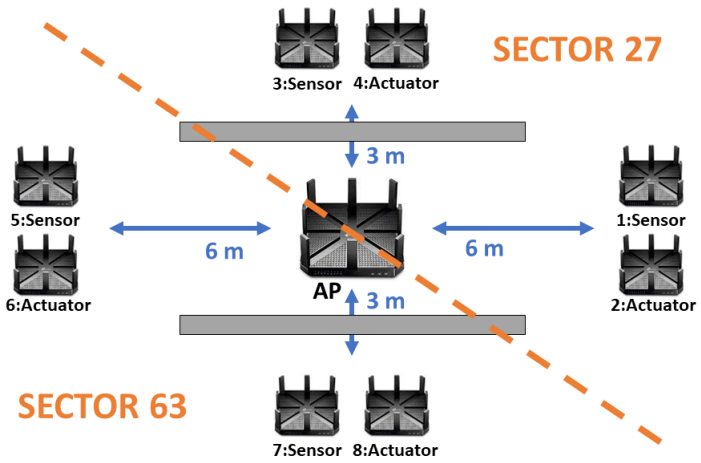

Figure 6.2: Topology of simulated 802.11ad sensors and actuators network

Table 6.6: Sensors and actuators network simulation configuration

	Parameter	Value
Timing	BI (μs)	1024
	SP (μs)	15
	Simulation (BI)	1.00E+06
Beamforming	Sectors	8
	SSSlots	1
Data	Payload (Byte)	13
	Protocol	IPv4 + UDP
SNR	Nodes 1, 2 (dB)	20
	Nodes 3, 4 (dB)	12
	Nodes 5, 6 (dB)	22
	Nodes 7, 8 (dB)	12

a SP based access is defined for all the nodes, since this grants exclusive channel access to them. Eight SPs are assigned in total, half of which cover the sensors to AP transmissions and the other half are for packets from the AP to the actuators. The duration of individual SPs is set to 15 μs, which is the shortest timeslot that allows to exchange a packet. At last, the A-BFT section of the BHI is configured with the objective of shortening its duration as much as possible. This is achieved by setting just one sweep of 8 sectors, which limits the system to the aggregation of one device per BI. Since the network is very small and all the nodes are previously known, this can be an assumable configuration.

The duration of the simulation is set to 1024 seconds, which corresponds to 10^6 BIs. This length is selected using the link level MC simulations as a reference, where the same amount of iterations was considered. Each node sends or receives one packet

with a payload of 13 bytes in each BI and is encapsulates it using UDP and IPv4, which is the combination that introduces the least overhead.

At last, the PER of individual links is defined using the tables that were generated in the link level simulation. The specific table and distance within it are selected based on the position of the nodes in Figure 6.2. On the other hand, the SNR is computed as the difference between the noise floor, which is extracted from the measurements the mmICM was elaborated with, and the power that would arrive at each distance. This last part is computed considering both the power used by the COTS device and the antenna gain.

Results from this simulation are discussed next. A PCAP file that contains all the messages exchanged by the AP was generated during the simulation, from where the amount of successfully exchanged packets and their corresponding timestamps were extracted. Under ideal conditions, each node would send/receive an UDP frame per BI, which corresponds to an elapsed time of 1024 μs between packets. However, some frames were lost due to the errors of the channel and two or three BIs were required to restore the communications in these cases. The amount of elapsed BIs between consecutive messages is broken down in Table 6.7, and the percentage of erroneous BIs, which correspond to the ones where no packet is present, is provided as well.

As it can be seen, the measured errors are consistent with the probabilities of their corresponding links, which shows that the implementation of the NS-3 model is correct. The link level simulation showed an almost non-existent error probability for the LoS cases, which is true for the simulated results as well. In the NLoS nodes, most errors involve the loss of just one BI since these occur at arbitrary intervals, and some rare cases show the loss of two consecutive BIs as well. The error probabilities are almost identical for the uplink are downlink cases of each link type, which is attributed to the fact that both the AP and stations transmit using the same power and antenna

Table 6.7: Amount of elapsed BIs between received frames for all the nodes

	Number of elapsed BIs			**Lost frames (%)**
	One BI	**Two BIs**	**Three BIs**	
Node 1	999993	3	0	**3E-4**
Node 2	999987	6	0	**6E-4**
Node 3	995096	2447	3	**0.245**
Node 4	995084	2450	5	**0.246**
Node 5	999999	0	0	**0**
Node 6	999999	0	0	**0**
Node 7	998635	682	0	**0.068**
Node 8	998835	582	0	**0.058**

radiation pattern.

The reliability of the network as a whole is analysed after. Here, the amount of erroneous BIs is measured, where an error is assumed to occur when at least one of the nodes cannot perform a successful communication. A total amount of 6174 failed BIs were counted, which represents a reliability of 0.99386. Since the network requirements defined in [8] define a maximum error probability of 10^{-7}, this result indicates that the 802.11ad standard is not capable of providing the required reliability on its own, even if it shows potential to accomplish this.

At last, the elapsed time between received packets is analysed to assess the expected update rate of the network. Since the system is designed to operate with a periodic interval of 1024 μs, this is the fastest rate that can be achieved. As mentioned earlier, 6174 BIs failed to deliver all the information, which means that in these cases the required time to update the receiver will be higher. Out of the 6174 periods, 6125 recovered in the next period and the remaining 49 regained the connection after two periods. This implies that two contiguous BIs are lost in the worst case scenario and that a periodic update of 3072 μs can be guaranteed in all the cases. This value is between the most demanding and relaxed cases, where their corresponding periods are of 0.5 and 8 ms. At last, it must be considered that these results were simulation based and errors occurred at arbitrary times. In reality, these errors could be correlated, which is why contrasting these findings with real measurements is strongly recommended.

6.3.2 Topology 2: Backhaul

This section details the second network simulated in NS-3, which is a backhaul network that manages different tasks within a workshop. Its structure can be found in Figure 6.3.

The behaviour of this network is as follows. A centralized controller (CONTROL) manages several processes that take place in the workshop, and two repeaters (REP1, REP2) are installed to increase the coverage of the network. As for the devices, three different types are connected to the backhaul network.

First, four nodes that control a Wireless Sensors and Actuators Network (WSAN) each (WSAN1-4) are connected to the backhaul network. Each node is located at one corner of the workshop, and they are assumed to perform the communication with their corresponding sensors and actuators successfully. These nodes use the backhaul to send the information collected by the sensors to the controller node, which processes it and sends back commands for the actuators.

The remaining nodes of the network are two robotic arms (ROBOT1, ROBOT2) and a crane (CRANE1), which are located at different locations of the backhaul

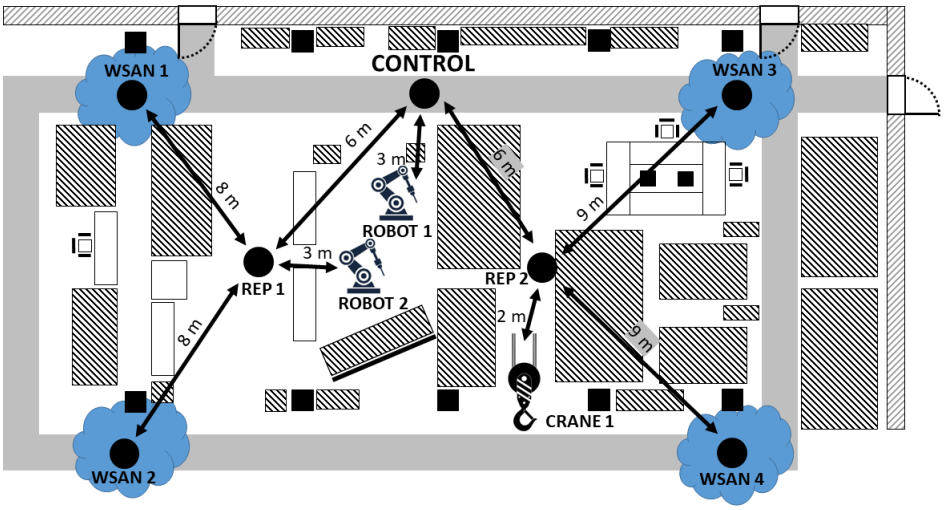

Figure 6.3: Topology of simulated 802.11ad backhaul network

network. Their operation is similar to the one of the WSAN nodes, where information is sent to the control node and commands are received.

The configuration for the simulation of this topology is discussed next, and all the relevant parameters are listed in Table 6.8.

Most parameters are identical to the ones set for the sensors and actuators network simulation, and the motivation for their selection is the same in this case as well, which is why no further detail is provided in these cases. The only exceptions are the data payload and SNR values, which are discussed next.

On one hand, the payload of the data has been increased to 64 Bytes, which

Table 6.8: Backhaul network simulation configuration

		Parameter	Value
Timing		Duration (s)	1024
		BI (μs)	1024
		SP (μs)	15
Beamforming		Sectors	8
		SSSlots	1
Data		Payload (Byte)	64
		Protocol	IPv4 + UDP
SNR	CONTROL -	REP1, REP2 (dB)	10
		ROBOT1 (dB)	16
	REP1 -	WSAN1, WSAN2 (dB)	8
		ROBOT2 (dB)	16
	REP2 -	WSAN3, WSAN4 (dB)	6
		CRANE1 (dB)	20

corresponds to the maximum size defined in [8] for the use case under test. Since the nodes that participate in the backhaul may aggregate several parameters within a single packet (e.g. the information collected by various sensors), using the maximum length can be more appropriate to represent this kind of network.

On the other hand, the SNR values have been computed again for these links. Here, the procedure is the same as in the previous network, where the difference between the noise floor and the power that would arrive at each distance is computed to obtain this parameter.

The previously generated simple NS-3 channel model has been used here as well to assign error probabilities to the different links. As for the type of link, the LoS case with the directional antenna radiation pattern (whose error probabilities are listed in Table 6.4) has been selected, since the link level simulation showed that this is the most reliable option.

A reference performance metric set has been generated in order to determine if there is any improvement by using the 802.11ad standard. To achieve this, the same network has been simulated using 802.11ax [126] compliant nodes, which gives an insight of the behaviour of the 802.11 standard in other frequency bands. The 802.11ax nodes have been configured to operate with the MCS 4 and a bandwidth of 160 MHz, providing a throughput of 408 Mbps similar to the 385 Mbps rate of 802.11ad. Apart from this, the simple channel model cannot be used in this test, since all the MC simulations have been carried out with signals in the 60 GHz spectrum. Instead, the *LogDistancePropagationModel* provided by NS-3 has been used, extracting the path loss exponent from the measurements of the VMC scenario introduced in Section 5.1.2, which is the same scenario that has been evaluated in the link level simulation with the mmICM. At last, the MAC layer frame aggregation mechanism has been disabled in the 802.11ax nodes, since this mechanism does not cope well with low latency oriented applications.

The results obtained in these simulations are discussed next. Here, two aspects have been considered in order to evaluate the performance: the amount of received packets and the elapsed time between them.

The amount of received packets can be used to determine the expected reliability of the network. In order to evaluate this aspect, the traffic exchanged by the CONTROL node has been captured in a PCAP file, and all the packets originated in the rest of devices have been analysed. Since the amount of transmitted ones is known, the percentage of successfully received packets can be computed. This metric is shown in Table 6.9 for the 802.11ad and 802.11ax managed networks. Note that the simulation stopped just after transmitting the last frame, which means that all the transmitted or

Table 6.9: Percentage of received packets in CONTROL

	Received packets (%)	
	802.11ad	**802.11ax**
WSAN 1	99.92	34.03
WSAN 2	99.91	34.02
WSAN 3	94.16	14.32
WSAN 4	94.11	14.34
ROBOT 1	99.99	81.50
ROBOT 2	99.99	34.18
CRANE 1	99.99	14.19

buffered packets are assumed to be erroneous after this instant. The results show that 802.11ad clearly outperforms 802.11ax, and two reasons can explain this behaviour. The first one is the use of the mmWave spectrum, where a higher SNR can be achieved thanks to the lower levels of multipath and interference, effectively reducing the amount of erroneous transmissions. The second reason is that 802.11ad uses a radio access scheme that suits the evaluated use case better. In 802.11ad, each node has a unique time window within the BI, where an exclusive channel access is granted. On the other hand, 802.11ax nodes need to request channel access before transmitting a packet, which is a time consuming process and not well suited for large amounts of very short packets. This difference in the performance highlights the importance of selecting an appropriate radio access scheme. At last, even if the 802.11ad nodes show a better performance, the reliability requirement of a maximum PER of 10^{-7} cannot be met unless links that have a very short distance are employed, which can be a challenge for the most demanding use cases.

The elapsed time between received packets gives an insight of the update rate that the network can achieve. Following the reliability analysis case, the elapsed time between the packets received in the CONTROL node has been analysed to determine the achievable update rate in each standard. Concretely, the CDF of the required time to receive an update has been computed to better analyse this aspect. Figure 6.4 shows the obtained CDF curves, where the packets received from the WSAN nodes and the rest have been differentiated in two graphs to improve the readability. As it can be seen, the periodical structure of 802.11ad makes the received packets arrive at multiples of 1024 μs, which is the duration of a BI. As it can be seen, most nodes can provide an update rate of 1024 μs with a reliability of 0.99, unless WSAN3 and WSAN4 nodes where the reliability is of 0.94 for this update rate. The larger distance of the communication link that these nodes have can be a possible cause for this drop in reliability, since packets are more susceptible to error in these links. In any case, their

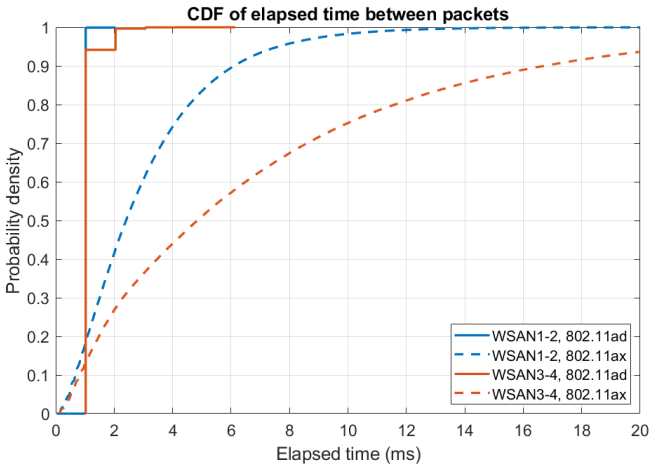

(a) WSAN generated packets

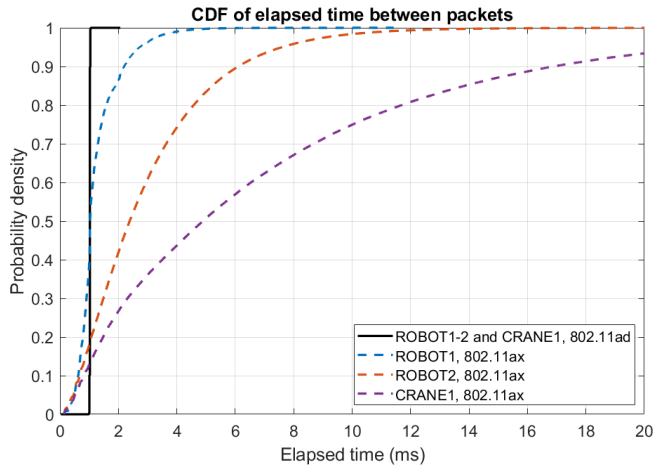

(b) ROBOT and CRANE generated packets

Figure 6.4: CDF of elapsed time between arrived packets in CONTROL node

reliability can be raised to 0.99 as well if an update period of 2048 μs is considered, and the worst case measured with this standard is of 6144 μs in WSAN3, which is still below the most relaxed update rate requirement of a periodic interval of 8 ms defined in [8]. On the other hand, 802.11ax nodes present a much less predictable behaviour since the channel access needs to be negotiated before each transmission. Some cases show a shorter update period than the 802.11ad case, but in general the elapsed time is considerably larger. The required time to achieve an update with a reliability of 0.99 is of 4, 12 and 34 ms for the ROBOT1, ROBOT2 and CRANE1 nodes, which again shows that this standard is not well suited for use cases where large amounts of short messages are exchanged. The overall conclusion extracted from these results is that none of the standards is capable to provide an update rate that copes with the

most stringent requirement, where the period should be of 0.5 ms. However, 802.11ad shows some promising results in this regard, and if the more relaxed update period of 8 ms is considered, the standard itself could be enough to provide the necessary update rate.

6.4 Summary

This chapter has presented a simulation based analysis of the performance that an IEEE 802.11ad standard operated industrial network can provide for use cases focused on the reliability and time-critical aspects. A conference paper named *Simulation based IEEE 802.11ad performance assessment in factory workshop* [38] was elaborated with all the work described in this chapter, which will be presented in the CSCN on November 2023.

The requirements that this kind of network must fulfill were reviewed first along the available tools that could be used for this task. As for the application of interest, the close loop regulatory control use case defined in [8] was selected, since this presents the most stringent demands. Apart from this, a COTS router that operates with the 802.11ad standard was analysed as well, and its properties were included in the simulations to make them as realistic as possible. At last, NS-3 was selected as the simulation tool because it was the only alternative that supports 802.11ad networks. Since this simulation tool was not designed to represent complex channels, the simulation process was split in two steps: an initial one where individual links were tested with a realistic channel in Matlab and a second one in NS-3 that used the previously generated metrics to represent the links of an entire network.

The link level simulations were described next. Here, the PER metric was computed for the transmission of an individual 802.11ad frame. The channel was represented with the mmICM described in Chapter 5, and 36 types of links were tested in total using MC simulations. Each link was a combination between a distance, ranged between 2 and 10 meters in 1 meter steps, the presence of direct vision between stations (LoS or NLoS) and the employed antenna radiation pattern, which could be directional or omnidirectional. The results obtained in these simulations showed a clear advantage of the LoS links, where an error-free connection can be achieved with a sufficient SNR unlike the NLoS cases where an error floor was present regardless of the SNR value. Apart from this, directive antennas showed a visible improvement as well, where the error floor was an order of magnitude lower compared to its omnidirectional counter-part in some scenarios.

At last, the network level simulations were performed. Two topologies were tested

here: one where information was exchanged within a sensors and actuators network and another one where the backhaul network of a workshop was represented. The sensors and actuators network included some of the scenarios considered in the link level simulation, and both reliability and update rate metrics were computed from the packages acquired by the AP. The results showed that the reliability metric could not be met, whereas the provided update rate could be enough to cover the just more relaxed use cases within the context of interest. On the other hand, the backhaul network was tested on a larger scale using the best case scenario, which was LoS links with directive antennas. Its performance was compared to the one of the same network simulated with the 802.11ax standard, and the obtained results showed that 802.11ad was clearly better suited for the evaluated scenario. Two main reasons were attributed to these results: the use of the mmWave spectrum, which improved the overall quality of the received signal and the radio access scheme employed in 802.11ad, which grants exclusive channel access to the nodes in periodic intervals. Even if the 802.11ad showed a great potential for this particular use case, the ultimate conclusion was that the performance provided by the standard on its own was not sufficient to cope with the most demanding reliability and time-critical requirements. However, since the performance was close to the required values, it was concluded that it could be used in more relaxed use cases or improved to the point where these requirements could be met as well.

Chapter 7

Conclusions

This thesis has focused on assessing the viability of mmWave band communications for industrial applications, where the reliability and determinism aspects are critical for a correct operation of the processes. The main conclusions drawn from the work are discussed in this chapter, which is organised as follows.

The main contributions of the thesis are summarized first, where all the findings are discussed. Next, the hypotheses presented in Section 2.2 are contrasted with the obtained results and validated or rejected. At last, the future lines are discussed, where possible ways to expand the carried out research are provided.

7.1 Contributions of the thesis

This thesis has brought four major contributions, which are listed next:

- A channel sounder that measures electromagnetic signal propagation in the mmWave spectrum has been elaborated. This equipment was created with COTS devices, and it was designed with indoor industrial environments in mind. In order to properly characterize the multipath-rich sites of interest, highly directional antennas were selected along automatic rotating stands, which can achieve double-directional CIRs. At last, the channel sounder was validated with three empirical tests, where its measurements were proved to be in accordance with the real environment. Details regarding this topic can be found in Chapter 4.

- A measurement campaign has been carried out in real industrial sites. This campaign includes the characterization of a workshop and a pit oven from a steel industry, and all the measured data was submitted to a public repository. Some propagation characteristics as the PL or spread in delay and azimuth were extracted from the acquired data as well. This information was compared to other metrics that were reported in similar works found in the literature, from where it was concluded that the pit oven scenario is a particularly harsh environment to perform

communications over the mmWave frequency band. A detailed explanation of this contribution is provided in Chapter 4.

- A stochastic channel model that represents the propagation of mmWave frequency band signals in industrial sites has been elaborated. This model is based on measurements performed over a mechanical university workshop, which were acquired with a higher resolution than the previous measurement campaign. The model can estimate the CIR in three different sites within the workshop, considering parameters as the distance, antenna configuration or the presence of direct vision between both ends. This is achieved by combining stochastic and deterministic processes that estimate the number of multipath components, their arrival power, delay, azimuth angle and other parameters. The channel model was validated later by checking the similarity between the measurements and samples elaborated with the model under the same conditions, where both approaches showed results that were correlated. At last, transmissions of IEEE 802.11ad packets were simulated over the developed model, as well as two additional models found in the literature in order to perform a preliminary evaluation of the expected performance of the standard in an industrial site. More information regarding this contribution can be found in Chapter 5.

- A simulation based performance assessment of the IEEE 802.11ad standard has been carried out for industrial use cases, focusing on the reliability and time-critical aspects. This test was carried out with the aim of evaluating the capabilities of the standard for reliable and deterministic communications. The simulation process was divided in two sections, where individual links were tested first under several conditions and a complete network was simulated later using the metrics extracted from the links. The obtained results showed that, in order to achieve reliable communications with this standard, direct vision between stations must be guaranteed. Additionally, directional antenna radiation patterns showed to be a significant aid. Apart from this, the network level simulation concluded that the standard cannot provide a performance that copes with the most demanding requirements on its own. However, the standard showed potential for this kind of applications since its capabilities are almost on par with the demands, which indicates that modifications could achieve a performance that copes with the most stringent requirements. This contribution is detailed in Chapter 6.

The adoption of mmWave frequency bands for communication systems is an actively discussed topic at the time in which this thesis has been developed. Some efforts have already been carried out in order to use this technology for industrial

use cases, but the development is still in its early stage. This is partly because, due to the novelty of the use of the mmWave spectrum for communication systems, the behaviour of these signals has not been extensively analyzed yet in factory sites, which is essential to assess the achievable performance of the communications. This thesis has contributed to overcome this limitation by providing the following: a tool for measuring the propagation, two measurement campaigns, a model to represent the observed propagation in a simulated environment and finally an analysis of the performance that a commercial standard can achieve in an industrial network, effectively increasing the state of the art knowledge that can be found in this topic.

7.2 Validation of hypotheses

Validity of the hypotheses presented in Section 2.2 is analysed in this section. All the hypotheses are discussed next:

HYPOTHESIS 1: IT IS POSSIBLE TO MAKE ACCURATE MMWAVE SIGNAL PROPAGATION MEASUREMENTS USING LOW COST COTS EQUIPMENT.

The elaboration of a custom, cost-effective channel sounder for mmWave signal propagation measurements is discussed in Chapter 4. The proposed design has two main drawbacks, which are the limited range due to the cable based synchronization of both ends and the long acquisition periods, allowing to measure only static environments. Even if the channel sounder has these limitations, it is perfectly viable to make measurements of factory scenarios with it, which validates the first hypothesis.

HYPOTHESIS 2: INDUSTRIAL SITES PRESENT DIFFICULTIES FOR MMWAVE SIGNAL PROPAGATION DUE TO THE ABUNDANCE OF REFLECTIVE SURFACES.

Two real industrial sites are characterized in Chapter 4, which are a university workshop and the surroundings of a pit oven that belongs to a steel company. Considering the results from the contributions of this thesis, it is concluded that the transmission of mmWave electromagnetic signals can be challenging in some industrial sites. The pit oven scenario showed a significantly greater attenuation compared to other indoor scenarios, which is the reason to believe that some industrial sites can be seen as harsh environments for communications, even in the mmWave spectrum. However, since industrial sites can be very diverse depending on their type (workshop, mining, logistics, food production and so on), the evidence provided in this work may be insufficient to fully validate the second hypothesis.

HYPOTHESIS 3: THE PROPAGATION OF MMWAVE BAND SIGNALS IN INDUS-

TRIAL SITES CAN BE APPROXIMATED WITH MATHEMATICAL FORMULAS AND STOCHASTIC PROCESSES.

Chapter 5 describes the work related to the elaboration of a custom channel model based on samples of the propagation of mmWave signals within a university workshop. The main limitation of the model is the scarcity of the measurements, as very few samples are available per scenario due to the long acquisition time of the channel sounder. In any case, the model showed to be able to properly represent the observed data in the validation process, which is why it is concluded that a model that combines stochastic and deterministic approaches is a suitable candidate to represent the propagation of mmWave electromagnetic signals within industrial sites. Thus, the third hypothesis is considered to be valid even if performing additional measurements would be recommended to refine the model and add an additional source of validation.

HYPOTHESIS 4: EXISTING STANDARD THAT OPERATE OVER MMWAVE FREQUENCIES CANNOT MEET THE MOST STRINGENT RELIABILITY DEMANDS OF INDUSTRIAL COMMUNICATIONS, BUT MODIFICATIONS CAN BE DONE TO IMPROVE THEIR PERFORMANCE.

A simulation based analysis of the IEEE 802.11ad standard has been carried out in Chapter 6 for networks in the context of FA, where the reliability and latency aspects have been observed. These simulations have been done in two steps due to the limitations of the tools, starting by testing the reliability of individual 802.11ad links and ending by simulating two complete networks. As for the results, the link level simulation showed that it is possible to achieve an error free communication if the right conditions are met. On the other hand, the network level results showed that, under ideal circumstances, the reliability requirements can only be met in very short links and that the standard is not designed to cope with the most stringent update rate. However, the obtained metrics indicate that there is potential to achieve this since the measured performance is close to the required one. Thus, it is concluded that it is indeed possible to achieve a sufficient performance with the right modifications of the standard.

7.3 Future lines

After analysing all the contributions and the current state of the thesis, three tasks that improve the existing work have been identified. The following paragraphs introduce the tasks that could be followed to expand and increase the quality of the existing

work.

7.3.1 Reduction of the acquisition time of the channel sounder

As mentioned in Section 7.1, one of the contributions of this thesis has been the development of a channel sounder capable of measuring mmWave signal propagation in factory sites. However, two limitations were detected during the measurement campaigns carried out with this equipment, which can be critical for other kind of measurements. The limitations derive from the long acquisition time required by the sounder, which makes it impossible to measure large amounts of positions or time varying channels. A possible way to overcome this limitation could be to improve the existing design and provide a more powerful solution, which can be an interesting research line as well.

As mentioned, the issue is that the acquisition time is prohibitively high and two possible solutions are discussed next.

Each sample requires several hours to complete mostly because all the antenna azimuth orientation combinations need to be tested. This means that if, for example, the azimuth scan is going to be completed in 3º steps, each end has 360/3 = 120 possible orientations. All the possible combinations would be 120^2 = 14400, which, if each positioning equals to approximately 1 second, equals to 4 hours of time just positioning the antennas. An alternative could be to change the type of antenna to an omnidirectional or electrically steerable one. The omnidirectional antenna is the most simple solution, since the antenna is the only component that needs to be modified. However this also supposes the loss of spatial information in one end and a higher noise level. On the other hand, electrically steerable antennas could be used to accelerate the steering process. In this case, the main challenges would be to program their behaviour and to verify that they are capable of generating an almost identical beam in all the directions.

Another possible improvement could be to apply HW acceleration to the acquisition of data since a high volume of information is processed in each capture. Here, the oscilloscope could be replaced by an FPGA that is capable of processing high volumes of data and extracting and storing the CIR instead of relying on a computer that uses MATLAB to retrieve data from a remote device and process it.

Additional possibilities can also be explored, but after analysing the operation of the sounder it is certain that new aspects of the propagation could be evaluated if any of the pointed improvements is implemented.

7.3.2 Channel model improvements

In its current state, the channel model is capable of representing just static channels with reflecting surfaces that are set at predefined locations and have constant gains. If any movement is present within the facility, the channel cannot predict how would the CIR evolve with time. This could be an interesting addition for scenarios where mobility is unavoidable.

Another aspect that has not been considered during the development of the model is the presence of interference caused by neighbour networks. Including an interference source that represents this effect can also be a valuable addition to test more diverse scenarios.

At last, all the scenarios of the model were extracted from measurements carried out in a university workshop. Performing measurements in additional industrial sites and extracting their corresponding model parameters can also be another way to increase the value of the model.

7.3.3 Modifications to increase the reliability of 802.11ad

The IEEE 802.11ad standard has been used during several development stages of this thesis with the aim of testing communication systems in industrial sites. This standard is oriented to obtain the maximum throughput of the communications with the given resources, which does not cope well with industrial use cases where reliability and determinism are the main scope.

Another research line could be to investigate how to modify the standard for reliability driven use cases. Here, the main limitations could be identified first, and replacements of the architecture, components or behaviour could be proposed after in order to overcome them. Simulation based or HW assisted tests could be employed to verify and validate the proposed solutions, and once a prototype is ready additional tests could be done in real industrial plants. However, this is just an idea and further analysis would be required in order to determine if IEEE 802.11ad based solutions are not just possible but viable alternatives for wireless industrial communications.

Bibliographic References

[1] Andreja Rojko. “Industry 4.0 concept: Background and overview.” In: *International journal of interactive mobile technologies* 11.5 (2017).

[2] Ozlem Senvar and Erkut Akkartal. “An overview to industry 4.0”. In: *International Journal of Information, Business and Management* 10.4 (2018), pp. 50–57.

[3] Rainer Drath and Alexander Horch. “Industrie 4.0: Hit or hype?[industry forum]”. In: *IEEE industrial electronics magazine* 8.2 (2014), pp. 56–58.

[4] Baotong Chen et al. “Smart factory of industry 4.0: Key technologies, application case, and challenges”. In: *Ieee Access* 6 (2017), pp. 6505–6519.

[5] Nasser Jazdi. “Cyber physical systems in the context of Industry 4.0”. In: *2014 IEEE international conference on automation, quality and testing, robotics*. IEEE. 2014, pp. 1–4.

[6] László Monostori et al. “Cyber-physical systems in manufacturing”. In: *Cirp Annals* 65.2 (2016), pp. 621–641.

[7] Hugh Boyes et al. “The industrial internet of things (IIoT): An analysis framework”. In: *Computers in industry* 101 (2018), pp. 1–12.

[8] Karl Montgomery et al. *Wireless user requirements for the factory workcell*. Department of Commerce, National Institute of Standards and Technology, 2020.

[9] Michele Luvisotto, Zhibo Pang, and Dacfey Dzung. “Ultra high performance wireless control for critical applications: Challenges and directions”. In: *IEEE Transactions on Industrial Informatics* 13.3 (2016), pp. 1448–1459.

[10] Giuseppe Aceto, Valerio Persico, and Antonio Pescapé. “A survey on information and communication technologies for industry 4.0: State-of-the-art, taxonomies, perspectives, and challenges”. In: *IEEE Communications Surveys & Tutorials* 21.4 (2019), pp. 3467–3501.

[11] Brendan Galloway and Gerhard P Hancke. “Introduction to industrial control networks”. In: *IEEE Communications surveys & tutorials* 15.2 (2012), pp. 860–880.

[12] Thilo Sauter. “The three generations of field-level networks—Evolution and compatibility issues”. In: *IEEE Transactions on Industrial Electronics* 57.11 (2010), pp. 3585–3595.

[13] Max Felser. “The fieldbus standards: History and structures”. In: *Technology Leadership Day* (2002).

[14] Augusto Pereira Ian Verhappen. *Foundation Fieldbus*. 4th ed. ISA—The International Society of Automation, 2012. ISBN: 1937560201; 9781937560201.

[15] *Industrial communication networks - Profiles Part 1: Fieldbus profiles*. International Standard. International Electrotechnical Commission, Apr. 2019.

[16] Wolfhard Lawrenz. “CAN system engineering”. In: *From theory to practical applications, New York* (1997).

[17] Ming Yang and Guang Li. “Analysis of PROFINET IO communication protocol”. In: *2014 Fourth International Conference on Instrumentation and Measurement, Computer, Communication and Control*. IEEE. 2014, pp. 945–949.

[18] *Industrial communication networks - Profiles - Part 2: Additional fieldbus profiles for real-time networks based on ISO/IEC/IEEE 8802-3*. International Standard. International Electrotechnical Commission, Apr. 2019.

[19] Richard Zurawski. *Industrial communication technology handbook*. CRC Press, 2014.

[20] Jacopo Tosi et al. “Performance evaluation of bluetooth low energy: A systematic review”. In: *Sensors* 17.12 (2017), p. 2898.

[21] Sinem Coleri Ergen. “ZigBee/IEEE 802.15. 4 Summary”. In: *UC Berkeley, September* 10.17 (2004), p. 11.

[22] Jan Endresen. “Introduction to WISA”. In: *ABB STOTZ-KONTAKT GmbH, Berlin, Germany, Tech. Rep* (2006).

[23] Heitor Florencio, Adrião Dória Neto, and Daniel Martins. “ISA 100.11 a networked control system based on link stability”. In: *Sensors* 20.18 (2020), p. 5417.

[24] Jianping Song et al. “WirelessHART: Applying wireless technology in real-time industrial process control”. In: *2008 IEEE Real-Time and Embedded Technology and Applications Symposium*. IEEE. 2008, pp. 377–386.

[25] Wei Liang et al. “Survey and experiments of WIA-PA specification of industrial wireless network”. In: *Wireless Communications and Mobile Computing* 11.8 (2011), pp. 1197–1212.

[26] Wei Liang et al. “WIA-FA and its applications to digital factory: A wireless network solution for factory automation”. In: *Proceedings of the IEEE* 107.6 (2019), pp. 1053–1073.

[27] Michele Luvisotto et al. “Physical layer design of high-performance wireless transmission for critical control applications”. In: *IEEE Transactions on Industrial Informatics* 13.6 (2017), pp. 2844–2854.

[28] Óscar Seijo et al. “SHARP: A novel hybrid architecture for industrial wireless sensor and actuator networks”. In: *2018 14th IEEE International Workshop on Factory Communication Systems (WFCS)*. IEEE. 2018, pp. 1–10.

[29] Ralf Heynicke et al. “IO-Link Wireless enhanced factory automation communication for Industry 4.0 applications”. In: *Journal of Sensors and Sensor Systems* 7.1 (2018), pp. 131–142.

[30] Zhouyue Pi and Farooq Khan. “An introduction to millimeter-wave mobile broadband systems”. In: *IEEE communications magazine* 49.6 (2011), pp. 101–107.

[31] Sundeep Rangan, Theodore S Rappaport, and Elza Erkip. “Millimeter-wave cellular wireless networks: Potentials and challenges”. In: *Proceedings of the IEEE* 102.3 (2014), pp. 366–385.

[32] L Ericsson. “More than 50 billion connected devices”. In: *White Paper* 14.1 (2011), p. 124.

[33] Olaonipekun Oluwafemi Erunkulu et al. “5G mobile communication applications: A survey and comparison of use cases”. In: *IEEE Access* 9 (2021), pp. 97251–97295.

[34] Joseba Osa et al. “A Cost-Effective Directional Millimeter-Wave Channel Sounder for 60 GHz Industrial Wireless Communications”. In: *2022 IEEE 18th International Conference on Factory Communication Systems (WFCS)*. IEEE. 2022, pp. 1–8.

[35] Joseba Osa et al. “60 GHz mmWave Signal Propagation Characterization in Workshop and Steel Industry”. In: *2023 IEEE 19th International Conference on Factory Communication Systems (WFCS)*. IEEE. 2023, pp. 1–8.

[36] *NextG CMA | Home*. https://nextg.nist.gov/. (Accessed on 22/05/2023).

[37] Joseba Osa et al. *Measurement based stochastic channel model for 60 GHz mmWave industrial communications*. [Manuscript submitted to the IEEE Open Journal of the Industrial Electronics Society].

[38] Joseba Osa, Inaki Val, and Mikel Mendicute. *Simulation based IEEE 802.11ad performance assessment in factory workshop*. [Manuscript accepted in the CSCN’23 conference].

[39] Ranjit Kumar. *Research methodology: A step-by-step guide for beginners*. Sage, 2018.

[40] DK Ghodgaonkar, VV Varadan, and Vijay K Varadan. “Free-space measurement of complex permittivity and complex permeability of magnetic materials at microwave frequencies”. In: *IEEE Transactions on instrumentation and measurement* 39.2 (1990), pp. 387–394.

[41] S Rappaport Theodore et al. *Wireless communications: principles and practice*. 2002.

[42] Harald T Friis. “A note on a simple transmission formula”. In: *Proceedings of the IRE* 34.5 (1946), pp. 254–256.

[43] Constantine A Balanis. *Antenna theory: analysis and design*. John wiley & sons, 2015.

[44] Nanfang Yu et al. “Light propagation with phase discontinuities: generalized laws of reflection and refraction”. In: *science* 334.6054 (2011), pp. 333–337.

[45] C Lee Giles and Walter J Wild. “Fresnel reflection and transmission at a planar boundary from media of equal refractive indices”. In: *Applied Physics Letters* 40.3 (1982), pp. 210–212.

[46] Sana Salous. *Radio propagation measurement and channel modelling*. John Wiley & Sons, 2013.

[47] Ayşe Kızılersü, Markus Kreer, and Anthony W Thomas. *The weibull distribution*. 2018.

[48] CW Hoffman. “The m-Distribution, a general formula of intensity of rapid fading”. In: *Statistical Methods in Radio Wave Propagation: Proceedings of a Symposium held June*. 1958, pp. 18–20.

[49] Adel AM Saleh and Reinaldo Valenzuela. “A statistical model for indoor multipath propagation”. In: *IEEE Journal on selected areas in communications* 5.2 (1987), pp. 128–137.

[50] Zhengqing Yun and Magdy F Iskander. “Ray tracing for radio propagation modeling: Principles and applications”. In: *IEEE access* 3 (2015), pp. 1089–1100.

[51] Celalettin Umit Bas et al. “Real-time millimeter-wave MIMO channel sounder for dynamic directional measurements”. In: *IEEE Transactions on Vehicular Technology* 68.9 (2019), pp. 8775–8789.

[52] Sana Salous et al. “Wideband MIMO channel sounder for radio measurements in the 60 GHz band”. In: *IEEE transactions on wireless communications* 15.4 (2015), pp. 2825–2832.

[53] George R MacCartney and Theodore S Rappaport. “A flexible millimeter-wave channel sounder with absolute timing”. In: *IEEE Journal on Selected Areas in Communications* 35.6 (2017), pp. 1402–1418.

[54] Peter B Papazian et al. “A radio channel sounder for mobile millimeter-wave communications: System implementation and measurement assessment”. In: *IEEE Transactions on Microwave Theory and Techniques* 64.9 (2016), pp. 2924–2932.

[55] Xuefeng Yin, Cen Ling, and Myung-Don Kim. “Experimental multipath-cluster characteristics of 28-GHz propagation channel”. In: *IEEE access* 3 (2015), pp. 3138–3150.

[56] Thomas Zwick, Troy J Beukema, and Haewoon Nam. “Wideband channel sounder with measurements and model for the 60 GHz indoor radio channel”. In: *IEEE transactions on Vehicular technology* 54.4 (2005), pp. 1266–1277.

[57] Xianyue Wu et al. “60-GHz millimeter-wave channel measurements and modeling for indoor office environments”. In: *IEEE Transactions on Antennas and Propagation* 65.4 (2017), pp. 1912–1924.

[58] Katsuyuki Haneda et al. “A statistical spatio-temporal radio channel model for large indoor environments at 60 and 70 GHz”. In: *IEEE Transactions on Antennas and Propagation* 63.6 (2015), pp. 2694–2704.

[59] Alexander Maltsev et al. “Experimental investigations of 60 GHz WLAN systems in office environment”. In: *IEEE journal on selected areas in communications* 27.8 (2009), pp. 1488–1499.

[60] Cristina Cano et al. “A channel measurement campaign for mmWave communication in industrial settings”. In: *IEEE Transactions on Wireless Communications* 20.1 (2020), pp. 299–315.

[61] *60-GHz Switched-Array Channel Sounder*. URL: https://www.nist.gov/image/60-ghzswitched-arraychannelsounderjpg.

[62] *Talon AD7200 multi-band Wi-Fi Router*. URL: https://www.tp-link.com/us/home-networking/wifi-router/ad7200/.

[63] George R Maccartney et al. “Indoor office wideband millimeter-wave propagation measurements and channel models at 28 and 73 GHz for ultra-dense 5G wireless networks”. In: *IEEE access* 3 (2015), pp. 2388–2424.

[64] Pan Tang et al. “Millimeter wave channel measurements and modelling in an indoor hotspot scenario at 28 GHz”. In: *2018 IEEE 88th Vehicular Technology Conference (VTC-Fall)*. IEEE. 2018, pp. 1–5.

[65] Xavier Raimundo, Sana Salous, and Adnan Cheema. “Indoor dual polarised radio channel characterisation in the 54 and 70 GHz bands”. In: *IET microwaves, antennas & propagation* 12.8 (2018), pp. 1287–1292.

[66] Lorenzo Rubio et al. “Contribution to the channel path loss and time-dispersion characterization in an office environment at 26 GHz”. In: *Electronics* 8.11 (2019), p. 1261.

[67] Satoshi Yamakawa, Satoru Kishimoto, and Minseok Kim. “Quasi-deterministic channel model for millimeter-wave indoor entrance hall access links”. In: *IEICE Communications Express* 9.7 (2020), pp. 336–341.

[68] Fatih Erden, Ozgur Ozdemir, and Ismail Guvenc. “28 GHz mmWave channel measurements and modeling in a library environment”. In: *2020 IEEE Radio and Wireless Symposium (RWS)*. IEEE. 2020, pp. 52–55.

[69] Guojin Zhang et al. “Experimental characterization of millimeter-wave indoor propagation channels at 28 GHz”. In: *IEEE Access* 6 (2018), pp. 76516–76526.

[70] Guangrong Yue et al. “Measurements and ray tracing simulations for non-line-of-sight millimeter-wave channels in a confined corridor environment”. In: *IEEE Access* 7 (2019), pp. 85066–85081.

[71] Ziming Yu et al. “Wideband channel measurements and temporal-spatial analysis for terahertz indoor communications”. In: *2020 IEEE International Conference on Communications Workshops (ICC Workshops)*. IEEE. 2020, pp. 1–6.

[72] Marwan El Hajj et al. “Millimeter-wave propagation measurements at 60 GHz in indoor environments”. In: *2019 International Symposium on Signals, Circuits and Systems (ISSCS)*. IEEE. 2019, pp. 1–4.

[73] Jin Zhu, Haiming Wang, and Wei Hong. “Characterization of large-scale fading for 45 GHz indoor channels”. In: *Proceedings of 2014 3rd Asia-Pacific Conference on Antennas and Propagation*. IEEE. 2014, pp. 728–730.

[74] Sinh LH Nguyen et al. “Comparing radio propagation channels between 28 and 140 GHz bands in a shopping mall”. In: (2018).

[75] Lorenzo Rubio et al. “Millimeter wave channel measurements in an intra-wagon environment”. In: *IEEE transactions on vehicular technology* 68.12 (2019), pp. 12427–12431.

[76] Jeffrey A Fessler and Alfred O Hero. “Space-alternating generalized expectation-maximization algorithm”. In: *IEEE Transactions on signal processing* 42.10 (1994), pp. 2664–2677.

[77] Robert Craigen, Wolf Holzmann, and Hadi Kharaghani. “Complex Golay sequences: structure and applications”. In: *Discrete mathematics* 252.1-3 (2002), pp. 73–89.

[78] Mathis Schmieder et al. “Measurement and characterization of an indoor industrial environment at 3.7 and 28 GHz”. In: *2020 14th European Conference on Antennas and Propagation (EuCAP)*. IEEE. 2020, pp. 1–5.

[79] Satoshi Ito et al. “Measurement and Modeling of Propagation Characteristics for an Indoor Environment in the 28 GHz-band”. In: *2019 IEEE 30th Annual International Symposium on Personal, Indoor and Mobile Radio Communications (PIMRC)*. IEEE. 2019, pp. 1–6.

[80] Smruti Ranjan Panigrahi, Niclas Björsell, and Mats Bengtsson. “Radio Channel Measurement in Industrial Indoor Environments at the 24 GHz ISM band: Path loss and Channel Fading”. In: (2021).

[81] Mathis Schmieder et al. “Directional wideband channel measurements at 28 GHz in an industrial environment”. In: *2019 IEEE Global Communications Conference (GLOBECOM)*. IEEE. 2019, pp. 1–6.

[82] Hang Mi et al. “Millimeter Wave Channel Measurement and Analysis in Smart Warehouse Scenario”. In: *2022 IEEE International Symposium on Antennas and Propagation and USNC-URSI Radio Science Meeting (AP-S/URSI)*. IEEE. 2022, pp. 211–212.

[83] Alfred Mudonhi et al. “Mm-Wave Massive MIMO Channel Sounding in Industrial IoT Scenarios”. In: *2022 Joint European Conference on Networks and Communications & 6G Summit (EuCNC/6G Summit)*. IEEE. 2022, pp. 53–58.

[84] Yujie Wang et al. “Measurement-based Analysis and Modeling of Channel Characteristics in an Industrial Scenario at 28 GHz”. In: *2021 IEEE 94th Vehicular Technology Conference (VTC2021-Fall)*. IEEE. 2021, pp. 1–5.

[85] Shihao Ju et al. “Sub-Terahertz Channel Measurements and Characterization in a Factory Building”. In: *arXiv preprint arXiv:2203.03799* (2022).

[86] Diego Dupleich et al. “From Sub-6 GHz to mm-Wave: Simultaneous Multi-band Characterization of Propagation from Measurements in Industry Scenarios”. In: *2022 16th European Conference on Antennas and Propagation (EuCAP)*. IEEE. 2022, pp. 1–5.

[87] Yu Wang et al. “Measurement-based experimental statistical modeling of propagation channel in industrial IoT scenario”. In: *Radio Science* 55.9 (2020), pp. 1–14.

[88] Dmitrii Solomitckii et al. “Millimeter-wave channel measurements at 28 GHz in digital fabrication facilities”. In: *2019 16th International Symposium on Wireless Communication Systems (ISWCS)*. IEEE. 2019, pp. 548–552.

[89] Dmitrii Solomitckii et al. “Characterization of mmWave channel properties at 28 and 60 GHz in factory automation deployments”. In: *2018 IEEE Wireless Communications and Networking Conference (WCNC)*. IEEE. 2018, pp. 1–6.

[90] *Wireless InSite 3D Wireless Prediction Software*. URL: https://www.remcom.com/wireless-insite-em-propagation-software/.

[91] Klaus Wehrle, Mesut Günes, and James Gross. *Modeling and tools for network simulation*. Springer Science & Business Media, 2010.

[92] William Oberle. *Monte Carlo simulations: number of iterations and accuracy*. Tech. rep. Army Research Lab Aberdeen Proving Ground MD Weapons and Materials Research . . ., 2015.

[93] George F Riley. “The georgia tech network simulator”. In: *Proceedings of the ACM SIGCOMM workshop on Models, methods and tools for reproducible network research*. 2003, pp. 5–12.

[94] Mathieu Lacage and Thomas R Henderson. “Yet another network simulator”. In: *Proceedings of the 2006 Workshop on ns-3*. 2006, 12–es.

[95] "IEEE Standard for Information Technology–Telecommunications and Information Exchange between Systems - Local and Metropolitan Area Networks–Specific Requirements - Part 11: Wireless LAN Medium Access Control (MAC) and Physical Layer (PHY) Specifications". In: *IEEE Std 802.11-2020 (Revision of IEEE Std 802.11-2016)* (2021), pp. 1–4379. DOI: 10.1109/IEEESTD.2021.9363693.

[96] Hany Assasa and Joerg Widmer. "Implementation and Evaluation of a WLAN IEEE 802.11 ad Model in ns-3". In: *Proceedings of the 2016 Workshop on ns-3*. 2016, pp. 57–64.

[97] John Harmon. *Understanding IEEE 802.11ad Physical Layer and Measurement Challenges*. https://www.keysight.com/upload/cmc_upload/All/22May2014Webcast.pdf. 2014.

[98] Kien Nguyen et al. "Empirical investigation of IEEE 802.11 ad network". In: *2017 IEEE International Conference on Communications Workshops (ICC Workshops)*. IEEE. 2017, pp. 192–197.

[99] Swetank Kumar Saha et al. "On the feasibility of indoor IEEE 802.11 ad WLANs". In: *2015 IEEE Conference on Computer Communications Workshops (INFOCOM WKSHPS)*. IEEE. 2015, pp. 107–108.

[100] Hany Assasa et al. "Medium access and transport protocol aspects in practical 802.11 ad networks". In: *2018 IEEE 19th International Symposium on" A World of Wireless, Mobile and Multimedia Networks"(WoWMoM)*. IEEE. 2018, pp. 1–11.

[101] Shivang Aggarwal, Arvind Thirumurugan, and Dimitrios Koutsonikolas. "A first look at 802.11 ad performance on a smartphone". In: *Proceedings of the 3rd ACM Workshop on Millimeter-wave Networks and Sensing Systems*. 2019, pp. 13–18.

[102] MZ Zaaimia et al. "Design and performance evaluation of 802.11 ad phys in 60 GHz multipath fading channel". In: *2013 8th international workshop on systems, signal processing and their applications (WoSSPA)*. IEEE. 2013, pp. 521–525.

[103] C Hemanth and TG Venkatesh. "Performance analysis of contention-based access periods and service periods of 802.11 ad hybrid medium access control". In: *IET Networks* 3.3 (2014), pp. 193–203.

[104] Carlos Cordeiro, Dmitry Akhmetov, and Minyoung Park. "IEEE 802.11 ad: Introduction and performance evaluation of the first multi-Gbps WiFi technology". In: *Proceedings of the 2010 ACM international workshop on mmWave communications: from circuits to networks*. 2010, pp. 3–8.

[105] Xiaoyi Zhu, Angela Doufexi, and Taskin Kocak. "Throughput and coverage performance for IEEE 802.11 ad millimeter-wave WPANs". In: *2011 IEEE 73rd vehicular technology conference (VTC Spring)*. IEEE. 2011, pp. 1–5.

[106] Noriaki Saito et al. "A fully integrated 60-GHz CMOS transceiver chipset based on WiGig/IEEE 802.11 ad with built-in self calibration for mobile usage". In: *IEEE Journal of Solid-State Circuits* 48.12 (2013), pp. 3146–3159.

[107] Alexander Maltsev et al. "Statistical channel model for 60 GHz WLAN systems in conference room environment". In: *Proceedings of the Fourth European Conference on Antennas and Propagation*. IEEE. 2010, pp. 1–5.

[108] *N5252A E-Band Network Analyzer System*. URL: https://www.keysight.com/us/en/product/N5252A/e-band-network-analyzer-system.html.

[109] *60 GHz Transmitter/ Receiver Development System*. URL: https://www.pasternack.com/pages/Featured_Products/60-GHz-Transmitter-Receiver-Development-System.html.

[110] *V-Band Lens Horn Antenna*. URL: https://anteral.com/datasheets/lens-horn-antenna-wr15-30-dbi-gain.pdf.

[111] *8MR174-11 - Motorized Rotation Stage*. URL: https://www.standa.lt/products/catalog/motorised_positioners?item=68&prod=motorized_rotation_stage.

[112] *Spectrum Analyzer/Signal Analyzer MS2840A*. URL: https://www.anritsu.com/en-us/test-measurement/products/ms2840a.

[113] *MDO4000B Mixed Domain Oscilloscopes - Datasheet*. URL: https://www.tek.com/en/datasheet/mdo4000b-mixed-domain-oscilloscopes-datasheet.

[114] *R&S AMIQ I/Q Modulation Generator Operating Manual*. URL: https://www.rohde-schwarz.com/nl/manual/r-s-amiq-i-q-modulation-generator-operating-manual-manuals_78701-28872.html.

[115] *ADS7-V2EBZ*. URL: https://www.analog.com/en/design-center/evaluation-hardware-and-software/evaluation-boards-kits/eval-ads7-v2.html.

[116] *AD9174*. URL: https://www.analog.com/en/products/ad9174.html#product-overview.

[117] *Ovako*. URL: https://www.ovako.com/.

[118] 3GPP. *Study on channel model for frequencies from 0.5 to 100 GHz (Release 16)*. Technical Report (TR) 38.901. Version 17.0.0. 3rd Generation Partnership Project (3GPP), Mar. 2022. URL: https://portal.3gpp.org/desktopmodules/Specifications/SpecificationDetails.aspx?specificationId=3173.

[119] Frank J Massey Jr. "The Kolmogorov-Smirnov test for goodness of fit". In: *Journal of the American statistical Association* 46.253 (1951), pp. 68–78.

[120] Katsuyuki Haneda et al. "Comparison of delay and angular spreads between channel measurements and the COST2100 channel model". In: *2010 Loughborough Antennas & Propagation Conference*. IEEE. 2010, pp. 477–480.

[121] *WLAN Toolbox Documentation*. https://www.mathworks.com/help/wlan/index.html?s_tid=CRUX_lftnav.

[122] Alexander Maltsev et al. "Channel modeling in the next generation mmWave Wi-Fi: IEEE 802.11 ay standard". In: *European Wireless 2016; 22th European Wireless Conference*. VDE. 2016, pp. 1–8.

[123] Shu Sun, George R MacCartney, and Theodore S Rappaport. "A novel millimeter-wave channel simulator and applications for 5G wireless communications". In: *2017 IEEE International Conference on Communications (ICC)*. IEEE. 2017, pp. 1–7.

[124] Daniel Steinmetzer et al. "Compressive millimeter-wave sector selection in off-the-shelf IEEE 802.11 ad devices". In: *Proceedings of the 13th International Conference on emerging Networking EXperiments and Technologies*. 2017, pp. 414–425.

[125] Hany Assasa et al. "Implementation and Evaluation of a WLAN IEEE 802.11 ay Model in Network Simulator ns-3". In: *Proceedings of the 2021 Workshop on ns-3*. 2021, pp. 9–16.

[126] "IEEE Standard for Information Technology–Telecommunications and Information Exchange between Systems Local and Metropolitan Area Networks–Specific Requirements Part 11: Wireless LAN Medium Access Control (MAC) and Physical Layer (PHY) Specifications Amendment 1: Enhancements for High-Efficiency WLAN". In: *IEEE Std 802.11ax-2021 (Amendment to IEEE Std 802.11-2020)* (2021), pp. 1–767. DOI: 10.1109/IEEESTD.2021.9442429.